ISSN: 2376-2136 (Print)
ISSN: 2376-2144 (Online)

Trends in Renewable Energy

Volume 9, Issue 1, March 2023

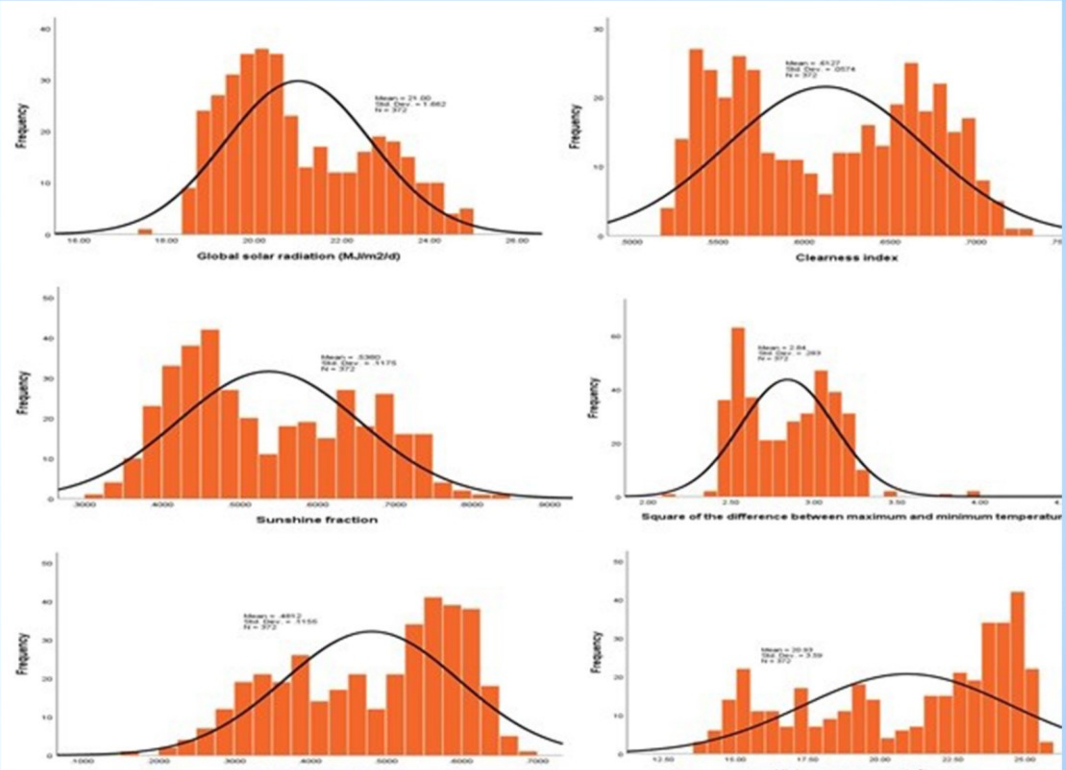

ISSN 2376-2136
22
9 772376 213001

futureenergysp.com
thefutureenergy.org

Trends in Renewable Energy

ISSN: 2376-2136 (Print)   ISSN: 2376-2144 (Online)

http://futureenergysp.com/

Trends in Renewable Energy is an open accessed, peer-reviewed semi-annual journal publishing reviews and research papers in the field of renewable energy technology and science.

The aim of this journal is to provide a communication platform that is run exclusively by scientists working in the renewable energy field. Scope of the journal covers: Bioenergy, Biofuel, Biomass, Bioprocessing, Biorefinery, Biological waste treatment, Catalysis for energy generation, Energy conservation, Energy delivery, Energy resources, Energy storage, Energy transformation, Environmental impact, Feedstock utilization, Future energy development, Green chemistry, Green energy, Microbial products, Physico-chemical process for Biomass, Policy, Pollution, Renewable energy, Smart grid, Thermo-chemical processes for biomass, etc.

The Trends in Renewable Energy publishes the following article types: peer-reviewed reviews, mini-reviews, technical notes, short-form research papers, and original research papers.

The article processing charge (APC), also known as a publication fee, is fully waived for the Trends in Renewable Energy.

Editorial Team of Trends in Renewable Energy

EDITOR-IN-CHIEF

Dr. Bo Zhang	Prof., School of Chemical Engineering & Pharmacy, Wuhan Institute of Technology, China
Dr. Changyan Yang	Prof., School of Chemical Engineering & Pharmacy, Wuhan Institute of Technology, China

HONORARY CHAIRMEN

Dr. Yong Wang	Voiland Distinguished Professor, The Gene and Linda Voiland School of Chemical Engineering and Bioengineering, Washington State University, United States
Dr. Mahendra Singh Sodha	Professor, Lucknow University; Former Vice Chancellor of Devi Ahilya University, Lucknow University, and Barkatulla University; Professor/Dean/HOD/Deputy Director at IIT Delhi; Padma Shri Award; India
Dr. Elio Santacesaria	Professor of Industrial Chemistry, CEO of Eurochem Engineering srl, Italy

VICE CHAIRMEN

Dr. Mo Xian	Prof., Assistant Director, Qingdao Institute of BioEnergy and Bioprocess Technology, Chinese Academy of Sciences, China

EDITORS

Dr. Yiu Fai Tsang,	Associate Prof., Department of Science and Environmental Studies, The Education University of Hong Kong
Dr. Melanie Sattler	Dr. Syed Qasim Endowed Professor, Dept. of Civil Engineering, University of Texas at Arlington, United States
Dr. Attila Bai	Associate Prof., University of Debrecen, Hungary
Prof. Christophe Pierre Ménézo	University of Savoy Mont-Blanc, France
Dr. Moinuddin Sarker	MCIC, FICER, MInstP, MRSC, FARSS., VP of R & D, Head of Science/Technology Team, Natural State Research, Inc., United States
Dr. Suzana Yusup	Associate Prof., Biomass Processing Laboratory, Centre for Biofuel and Biochemical Research, Green Technology Mission Oriented Research, Universiti Teknologi PETRONAS, Malaysia
Dr. Zewei Miao	Global Technology Development, Monsanto Company, United States
Dr. Hui Wang	Pfizer Inc., United States
Dr. Shuangning Xiu	North Carolina Agricultural and Technical State University, United States
Dr. Junming XU	Associate Prof., Institute of Chemical Industry of Forest Products, China Academy of Forest, China
Dr. Hui Yang	Prof., College of Materials Science and Engineering, Nanjing Tech University, China
Dr. Ying Zhang	Associate Prof., School of Chemistry and Materials Science, University of Science and Technology of China, China
Dr. Ming-Jun Zhu	Prof., Assistant Dean, School of Bioscience & Bioengineering, South China University of Technology, China

EDITORIAL BOARD

Dr. Risahbh Dev Shukla	Dean and Associate Prof., Department of Electrical Engineering, Budge Budge Institute of Technology Kolkata, India
Dr. Neeraj Gupta	Indian Institute of Technology Roorkee, India

Dr. Elena Lucchi	Politecnico di Milano, Italy
Dr. Muhammad Mujtaba Asad	Faculty of Technical and Vocational Education, Universiti Tun Hussein Onn Malaysia, Malaysia
Dr. Afzal Sikander	Department of Instrumentation and Control Engineering, Dr. B. R. Ambedkar National Institute of Technology, India
Dr. Padmanabh Thakur	Professor and Head, Department of Electrical Engineering, Graphic Era University, India
Dr. K. DHAYALINI	Professor, Department of Electrical and Electronics Engineering, K. Ramakrishnan College of Engineering, Tamilnadu, India
Shangxian Xie	Texas A&M University, United States
Dr. Tanmoy Dutta	Sandia National Laboratories, United States
Dr. Efstathios Stefos	Pontifical Catholic University of Ecuador, Faculty of Exact and Natural Sciences, School of Physical Sciences and Mathematics, Ecuador
Dr. Xin Wang	Miami University, United States
Dr. Rami El-Emam	Assist. Prof., Faculty of Engineering, Mansoura University, Egypt
Dr. Rameshprabu Ramaraj	School of Renewable Energy, Maejo University, Thailand
Dr. ZAFER ÖMER ÖZDEMİR	Kirklareli University, Technology Faculty, Turkey
Dr. Vijay Yeul	Chandrapur Super Thermal Power Station, India
Dr. Mohanakrishna Gunda	VITO - Flemish Institute for Technological Research, Belgium
Dr. Shuai Tan	Georgia Institute of Technology, United States
Shahabaldin Rezania	Universiti Teknologi Malaysia (UTM), Malaysia
Dr. Madhu Sabnis	Contek Solutions LLC, Texas, United States
Dr. Qiangu Yan	Mississippi State University, United States
Dr. Mustafa Tolga BALTA	Associate Prof., Department of Mechanical Engineering, Faculty of Engineering, Aksaray University, Turkey
Dr. María González Alriols	Associate Prof., Chemical and Environmental Engineering Department, University of the Basque Country, Spain
Dr. Nattaporn Chaiyat	Assist. Prof., School of Renewable Energy, Maejo University, Thailand
Dr. Nguyen Duc Luong	Institute of Environmental Science and Engineering, National University of Civil Engineering, Vietnam
Mohd Lias Bin Kamal	Faculty of Applied Science, Universiti Teknologi MARA, Malaysia
Dr. N.L. Panwar	Assistant Prof., Department of Renewable Energy Engineering, College of Technology and Engineering, Maharana Pratap University of Agriculture and Technology, India
Dr. Caio Fortes	BASF, Brazil
Dr. Flavio Prattico	Department of Methods and Models for Economics, Territory and Finance, Sapienza University of Rome, Italy
Dr. Wennan ZHANG	Docent (Associate Prof.) and Senior Lecturer in Energy Engineering, Mid Sweden University, Sweden
Dr. Ing. Stamatis S. Kalligeros	Associate Prof., Hellenic Naval Academy, Greece
Carlos Rolz	Director of the Biochemical Engineering Center, Research Institute at Universidad del Valle, Guatemala
Ms. Lilias Makashini	Copperbelt University, Zambia
Dr. Ali Mostafaeipour	Associate Prof., Industrial Engineering Department, Yazd University, Iran
Dr. Camila da Silva	Prof., Maringá State University, Brazil
Dr. Anna Skorek-Osikowska	Silesian University of Technology, Poland
Dr. Shek Atiqure Rahman	Sustainable and Renewable Energy Engineering, College of Engineering, University of Sharjah, Bangladesh
Dr. Emad J Elnajjar	Associate Prof., Department of Mechanical Engineering, United Arab Emirates University, United Arab Emirates
Dr. Seyed Soheil Mousavi Ajarostaghi	Babol Noshirvani University of Technology, Babol, Iran
Dr. Dinesh K. Sharma	National Ecology and Environment Foundation, India
Dr. Lakshmana Kumar Ramasamy	Department of Corporate relations, Hindusthan College of Engineering and Technology, India
Dr. S. Venkata Ramana	SUSU/National Research University, Russian Federation
Dr. Priyanka Marathey	Department of Solar Energy, Pandit Deendayal Petroleum University, India
Osamah Siddiqui	University of Ontario Institute of Technology, Canada

Dr. Rupendra Kumar Pachauri	Assistant Prof., Electrical and Electronics Engineering Department, University of Petroleum and Energy Studies, India
Dr. Jun Mei	School of Chemistry and Physics, Science and Engineering Faculty, Queensland University of Technology, Australia
Dr. Valeria Di Sarli	Institute for Research on Combustion, National Research Council of Italy, Italy
Dr. Utkucan Şahin	Assistant Prof., Department of Energy Systems Engineering, Faculty of Technology, Muğla Sıtkı Koçman University, Turkey
Dr. ALIASHIM ALBANI	School of Ocean Engineering, Universiti Malaysia Terengganu, Malaysia
Dr. Ashwini Kumar	Assistant Prof., College of Engineering, HSBPVT's Parikrama Group of Institutions, India
Dr. Hasan AYDOGAN	Associate Prof., Mechanical Engineering Department, Selcuk University, Turkey
Dr. Jiekang Wu	Professor, School of Automation, Guangdong University of Technology, China
Dr. Ong Huei Ruey	DRB-HICOM University of Automotive, Malaysia
Dr. Miguel Ángel Reyes Belmonte	IMDEA Energy Institute, Spain
Dr. Chitra Venugopal	Associate Professor in Electrical Engineering, University of Trinidad and Tobago, Trinidad
Dr. Amit Kumar Singh	Assistant Prof., Instrumentation & Control Engineering Department, Dr. B.R.A. National Institute of Technology, India
Dr. Suvanjan Bhattacharyya	University of Pretoria, South Africa
Dr. Karunesh Tiwari	Babu Banarasi Das University, India
Dr. Sharadrao A. Vhanalkar	Karmaveer Hire Arts, Science, Commerce and Education College, India
Dr. Prasenjit Chatterjee	Assistant Prof. and Head, MCKV Institute of Engineering, India
Dr. S. Balamurugan	Mindnotix Technologies, India
Dr. Mohammad Nurunnabi	University of Oxford, United Kingdom
Dr. Kenneth Okedu	Caledonian College of Engineering, Oman
Dr. Cheng Zhang	Sr. Materials Engineer, Medtronic, Inc., United States
Dr. Chandani Sharma	Assistant Prof., Department of Electrical Engineering, Graphic Era University, India
Dr. Kashif Irshad	Assistant Prof., Mechanical Engineering Department, King Khalid University, Saudi Arabia
Dr. Abhijit Bhagavatula	Principal Lead Engineer, Southern Company Services, United States
Dr. S. Sathish	Associate Prof., Department of Mechanical Engineering, Hindustan University, India
Mr. A. Avinash	Assistant Prof., KPR Institute of Engineering & Technology, India
Dr. Bindeshwar Singh	Assistant Prof., Kamla Nehru Institute of Technology, India
Dr. Yashar Hashemi	Tehran Regional Electric Company, Iran
Dr. Navanietha Krishnaraj R	South Dakota School of Mines and Technology, United States
Dr. SANDEEP GUPTA	JECRC University, India
Dr. Shwetank Avikal	Graphic Era Hill University, India
Dr. Xianglin Zhai	Poochon Scientific LLC, United States
Dr. Rui Li	Associate Prof., College of Engineering, China Agricultural University, China
Dr. Adam Elhag Ahmed	National Nutrition Policy Chair, Department of Community Services, College of Applied Medical Sciences, King Saud University, Saudi Arabia
Dr. Jingbo Li	Massachusetts Institute of Technology, United States
Dr. Srikanth Mutnuri	Associate Prof., Department of Biological Sciences, Associate Dean for International Programmes and Collaboration, Birla Institute of Technology & Science, India
Dr. Bashar Malkawi	Global Professor of Practice in Law, James E. Rogers College of Law, University of Arizona, United States
Dr. Simona Silvia Merola	Istituto Motori - National Research Council of Naples, Italy
Dr. Hakan Caliskan	Faculty of Engineering, Department of Mechanical Engineering, Usak University, Turkey
Dr. Umashankar Subramaniam	Associate Prof., College of Engineering, Prince Sultan University, Saudi Arabia
Dr. Tayfun GÜNDOĞDU	Faculty of Electrical and Electronic Engineering, Department of Electrical Engineering, Istanbul Technical University, Turkey
Dr. Yukesh Kannah R	Department of Civil Engineering, Anna University Regional Campus, India

Table of Contents

Volume 9, Issue 1, March 2023

Recent Studies on Alternative Fuel of Dimethyl Ether

Current Status of Research on Biodiesel as an Alternative Fuel for Internal Combustion Engines

Current Status of Research on Methanol as an Alternative Fuel to Conventional Fuels

Artificial Intelligence, Machine Learning and Neural Networks for Tomography in Smart Grid – Performance Comparison between Topology Identification Methodology and Neural Network Identification Methodology for the Distribution Line and Branch Line Length Approximation of Overhead Low-Voltage Broadband over Power Lines Network Topologies

Effects of Angstrom-Prescott and Hargreaves-Samani Coefficients on Climate Forcing and Solar PV Technology Selection in West Africa

Trends in Renewable Energy
OPEN ACCESS ISSN: 2376-2144
Peer-Reviewed Review Article futureenergysp.com/index.php/tre

Recent Studies on Alternative Fuel of Dimethyl Ether

Jixiang Zhang

School of Mechanical Engineering/Institute of Vehicles and New Energy Technology, North China University of Water Resources and Electric Power, Zhengzhou City, Henan, China

Received September 29, 2022; Accepted October 24, 2022; Published November 7, 2022

With the development of industrialization, a large number of non-renewable fuels (such as coal and crude oil) are consumed, and the harmful substances produced in the combustion process of a large number of fossil fuels have caused serious pollution to the atmosphere, and the harmful gases produced by combustion have caused disastrous damage to the ecological balance. Therefore, finding clean energy and exploring alternative fuels are very important in today's society. This paper mainly reviews the studies on the alternative fuels of dimethyl ether (DME). Firstly, the types of alternative fuels currently researched by society and their respective advantages and disadvantages are analyzed, and the preparation of dimethyl ether and its advantages and disadvantages are analyzed in detail. In addition, the physicochemical properties, combustion and emission characteristics of dimethyl ether and diesel are compared and analyzed. The conclusion is that the injection delay angle of dimethyl ether is larger than that of diesel, the ignition delay period is shorter than that of diesel, and the maximum explosion pressure, maximum pressure rise rate and combustion noise of dimethyl ether are lower than that of diesel. The diffusion combustion speed of DME is faster than that of diesel, and the combustion duration is shorter than that of diesel. At the same time, as an alternative energy, dimethyl ether engine has a significant reduction in NOx emission, a very low level of HC and CO emission, and zero soot emission. In conclusion, the DME engine has good performance and emission characteristics.

Keywords: Dimethyl ether; Diesel engine; Alternative fuel; Clean fuel

Introduction

A good ecological environment is not only the basis for human survival, but also the prerequisite for the sustainable and stable development of society. With the rapid development of global industry and economy, the main energy sources of human society, such as coal, crude oil and natural gas, have been irreversibly depleted after hundreds of years of over exploitation and huge consumption. As a populous country, China's per capita reserves of major fossil energy are far below the world's per capita level. In addition, the rough economic development model consumes a lot of energy, resulting in low production efficiency. Moreover, China has always been dependent on major fossil energy sources. It is a major problem that China's development is constrained by the energy problem. The implementation of sustainable development strategy, energy security and stable economic development must first solve the energy problem.

In addition, with the continuous increase of the total energy consumption, a large number of harmful substances generated during the burning of fossil fuels have caused

**Corresponding author:* 1916775930@qq.com

Tr Ren Energy, 2023, Vol.9, No.1, 1-10. doi: 10.17737/tre.2023.9.1.00148

serious pollution to the atmosphere, and the harmful gases generated during the burning have caused catastrophic damage to the ecological balance. These damages may include a series of chain reactions (such as climate warming, glacier melting, and sea level rise), and some coastal areas are in danger of being submerged. The above problems are threatening the survival of mankind and have already aroused great concern and concern of our government [1]. Under the dual pressure of energy pressure and environmental pressure, it is urgent for our government and researchers to work together to accelerate the development and utilization of new, cleaner and more environmentally friendly alternative energy.

Table 1. Main Components and Hazards of Automobile Exhaust

Component	Main hazards
CO	If CO in the atmosphere enters the human body, it will quickly combine with hemoglobin, weakening the ability of blood to provide for human tissues, causing chronic poisoning such as headache and dizziness caused by hypoxia, and making the reaction function, sensory function, memory function, etc. unable to work normally.
HC	Olefins have anesthetic effect and irritation to mucous membrane. HC will react with NO_2 to generate photochemical smoke. Aromatic hydrocarbons are harmful to blood, liver and nervous system. Polycyclic aromatic hydrocarbons and their derivatives have certain carcinogenic effect, and aldehydes are harmful to eye mucous membrane, respiratory tract and blood.
NO_x	It slowly oxidizes NO_2 in the atmosphere and combines with water to form nitric acid after being inhaled by the human body, causing cough, asthma, even emphysema and myocardial damage. NO_x is one of the main factors to form chemical smog.
PM	The main component is carbon, which can be suspended in the atmosphere for a long time without sedimentation. It will penetrate deep into human lungs, causing mechanical overload, damage the self purification devices of various channels in the lungs, and promote the toxic effect of other pollutants.

Automobile is an indispensable means of transportation in modern social life. With the continuous increase of car ownership, the exhaust emissions of traditional gasoline and diesel vehicles have an increasing impact on the environment. Among them, the pollution caused by automobile exhaust accounts for 60%~70% of the total air pollution. Due to multiple reasons such as automobile exhaust emissions and the environment, most parts of China are almost covered by a thick haze every day, which also makes the words "air quality" and "PM2.5" become frequently used words "smog" attacking the city. Under the heavy fog, automobile exhaust emissions become the culprit causing smog, and become the target of public criticism for a time. Among them, the hazards of the main components of exhaust gas from automobile internal combustion engines are shown in Table 1 [2]. These ingredients will have more and more negative effects on the environment and human body as the number of cars increases.

From the perspective of long-term energy strategy, we should actively develop alternative clean fuels to reduce dependence on fossil fuels such as oil. Therefore, the government should encourage and support the design, R&D and application of alternative fuel vehicles in policy, and give preferential policies in terms of taxation in the early stage of the development of alternative fuel vehicles, even for a period of time, to encourage the reduction of the consumption of fossil fuels such as oil, thus reducing environmental pollution [3].

Application of Alternative Fuels in Internal Combustion Engines

Common Alternative Fuels

At present, the most widely researched and applied alternative fuels mainly include liquefied/vaporized natural gas, liquefied petroleum gas, alcohol fuel, biofuel, hydrogen fuel, dimethyl ether (DME), mixed fuel, etc. [4-7]. A comparison of physical and chemical properties between traditional fuels and alternative clean fuels is shown in Table 2.

1) Liquefied/vaporized natural gas and liquefied petroleum gas

Liquefied/vaporized natural gas (LNG) and liquefied petroleum gas (LPG) have been widely used in urban public transport, and their outstanding feasibility has been confirmed. Liquefied/vaporized natural gas (LNG) and liquefied petroleum gas (LPG) have the following advantages: environmental protection, almost no black smoke in the emission, only a small amount of sulfur, and no benzene and lead, which greatly reduces the environmental pollution. With good antiknock property and much higher octane number than gasoline, the engine's power performance and thermal efficiency can be improved by appropriately increasing the compression ratio and adopting supercharging technology. With low vaporization temperature, it can enter the cylinder in the form of gas, with less carbon deposition, extending the engine overhaul cycle. It has high safety and adopts various structures and technologies to make the gas burn in a fully enclosed environment. The economy is good, and the price is lower than that of gasoline. However, since the natural gas is mainly stored in the west of China, and the application of natural gas is limited to local industries, the large-scale application of natural gas in China is limited [8].

2) Biodiesel

Biodiesel has many advantages, such as rich resources, which can be obtained by esterification of plant or animal fats, and it is a renewable resource. Besides, it has high energy density, excellent economic performance and emission performance. It can be directly used without changing the original structure of compression ignition engines. However, if it is used for a long time, it will produce carbon deposits inside the fuel injectors, and cause deterioration of lubricating oil and other problems [9]. In addition, it is necessary to ensure sufficient raw materials and high costs in the production process.

3) Alcohol fuel

The sources of methanol and ethanol in alcohol fuels are very rich. They can not only be extracted from coal, heavy oil and natural gas, but also from renewable resources such as sugar cane, sugar beet and plant fiber. Moreover, the technology is relatively mature. The biggest advantage of methanol and ethanol as alternative fuels is that there is almost no soot generated during combustion, which is very clean, and CO, HC and NO_X emissions are lower than those of compression ignition engines [10]. Therefore, alcohol fuel, one of the petroleum alternative fuels, has a great application prospect in the future.

4) Hydrogen

Hydrogen is an efficient and clean fuel. When burning hydrogen and gasoline of the same quality, the heat release of hydrogen is 3 times that of gasoline. The combustion product of hydrogen is only water, which will not lead to carbon deposition in the engine and will not pollute the environment. However, hydrogen is a secondary energy and needs to be produced by other energy sources, which leads to high production costs [11]. Moreover, the difficulties in storage and transportation of hydrogen also lead to the limitations of its wide application.

Table 2. Comparison of physical and chemical properties between traditional fuels and alternative clean fuels

Nature	**Gasoline**	**Diesel**	**Hydrogen**	**Dimethyl ether**	**Methanol**	**Ethanol**	**CNG**	**LPG**
Molecular formula	C_5-C_{12}	C_xH_y	H_2	CH_3OCH_3	CH_3OH	CH_3CH_2OH	CH_4	$C_3H_8+C_4H_{10}$
Octane number	90-106	20-30	0	-	111	111	130	107
Cetane number	13-17	40-55	0	55-60	<15	<8	Low	<10
Theoretical air fuel ratio A/F	14.8	14.6	34.3	8.9	6.5	9.0	17.2	15.53
Boiling point/°C	30-220	180-370	-253	25.1	65	78	-162	-35
Flash point/°C	-43	60	-252.8	-41.4	11	21	-187	-104
Autoignition temperature/°C	350-400	250	570	235	450	423	650	460
Liquid phase density/$kg \cdot L^{-1}$	0.72-0.75	0.84	0.169	0.66	0.79	0.79	0.47	0.52
Low calorific value/$MJ \cdot kg^{-1}$	44.5	42.5	10.8	28.8	19.9	27.6	50.1	46.0
Latent heat of vaporization/k$J \cdot kg^{-1}$	297	250	305	460	110	904	510	401
Vapor pressure/MPa	0.45-0.9	<0.01	10.67	0.5	0.2	0.18	-	0.1
20 °C dynamic viscosity/Pa·s	0.42	2.4	-	0.15	0.6	1.2	-	0.6
Volume ratio of combustible range/%	1.3-7.6	0.6-6.5	4.0-74.5	3.4-17	5.5-26	3.5-1.5	5-15	2.4-9.5
Mass fraction of oxygen atom/%	0%	0%	0%	34.8%	50%	34.8%	0%	0%
Mass fraction of carbon atom/%	85%-88%	86%	0%	52.2%	37.5%	52.2%	75%	82%

5) Dimethyl ether

In recent years, more and more countries around the world have studied dimethyl ether. The main reason is that dimethyl ether has a high cetane number, a low autoignition temperature and excellent compression characteristics. So it is suitable to replace diesel in compression ignition engines. Research shows that the thermal efficiency of direct injection compression ignition engines using dimethyl ether is the same as that of diesel fuel. In addition, the running stability and combustion noise of the engine are almost at the same level as those of the gasoline engine [12], and the exhaust emissions are clean and clean. No auxiliary ignition device and exhaust catalytic post-treatment device are required, which greatly reduces NO_X emissions and realizes smokeless combustion.

Clean Alternative Fuel of Dimethyl Ether

In order to change the tense situation of energy supply and demand in China and reduce automobile exhaust pollution, an alternative fuel with extensive sources, mature production technology, good economy and low pollution emissions is urgently needed. Dimethyl ether, as a new alternative fuel for diesel engines in recent years [11-15], has aroused great interest, and related research is increasing and deepening.

Preparation of Dimethyl Ether

Dimethyl ether fuel comes from a wide range of sources, and can be produced in large quantities from coal, natural gas, coalbed methane, biological organics, etc. [15-16]. The preparation of dimethyl ether can be divided into direct method and indirect method [17]. Direct method refers to the direct preparation of dimethyl ether from synthesis gas. The indirect method refers to the synthesis gas, which is first made into methanol, and then dehydrated from methanol. China is rich in coal resources, accounting for 11% of the world's total reserves, and the price is low, only about 1/3 of the world average price. Therefore, burning coal to produce dimethyl ether can not only effectively reduce environmental pressure and ease energy security problems, but also promote the development of clean coal combustion technology, which is a good way to do more with one action.

Comparison of Combustion and Emissions between Dimethyl Ether Engine and Diesel Engine

Comparison of Combustion Characteristics between Dimethyl Ether Engine and Diesel Engine

Figure 1 shows the comparison of indicator diagram and heat release rate of dimethyl ether engine and diesel engine. It can be seen from the figure that the cetane number of dimethyl ether is higher than that of diesel, and the ignition delay period is shorter than that of diesel. During the ignition delay period, the diesel engine accumulates more fuel in the cylinder and burns together after ignition, resulting in a higher maximum explosive pressure than that of the DME engine. The injection delay of dimethyl ether is larger than that of diesel. When the fuel injection advance angle is the same, the injection advance angle of dimethyl ether is smaller than that of diesel. The position corresponding to the maximum cylinder pressure of the dimethyl ether engine is later than that of the diesel engine [19].

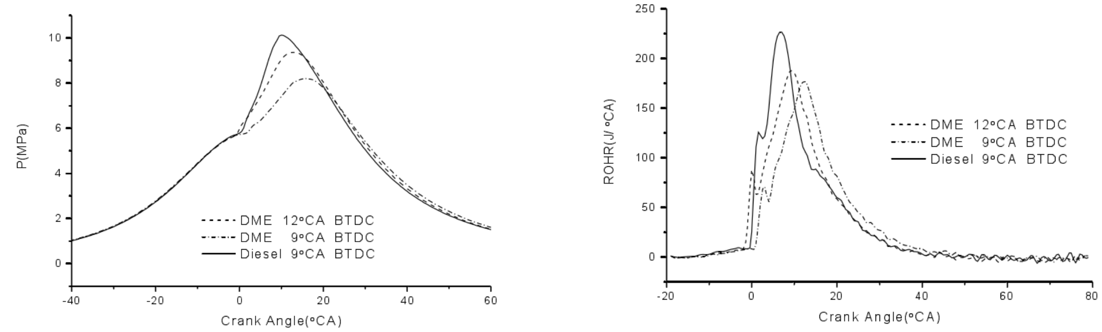

a) 800 r/min Pe=0.87 MPa

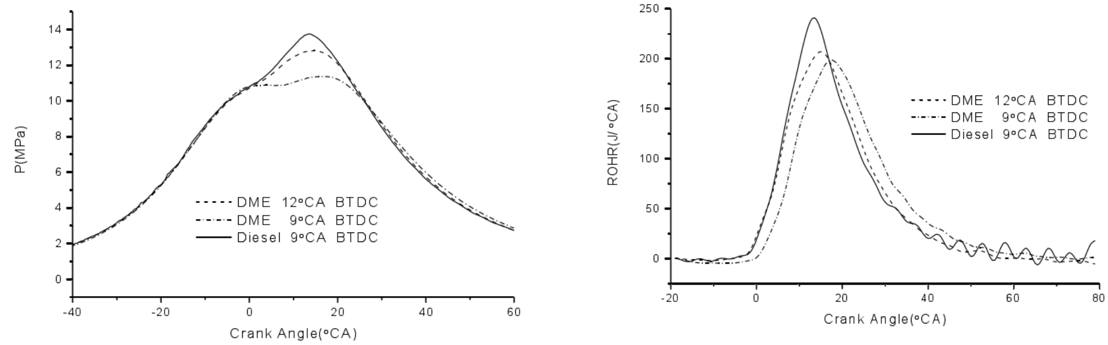

b) 1400 r/min Pe=1.52 MPa

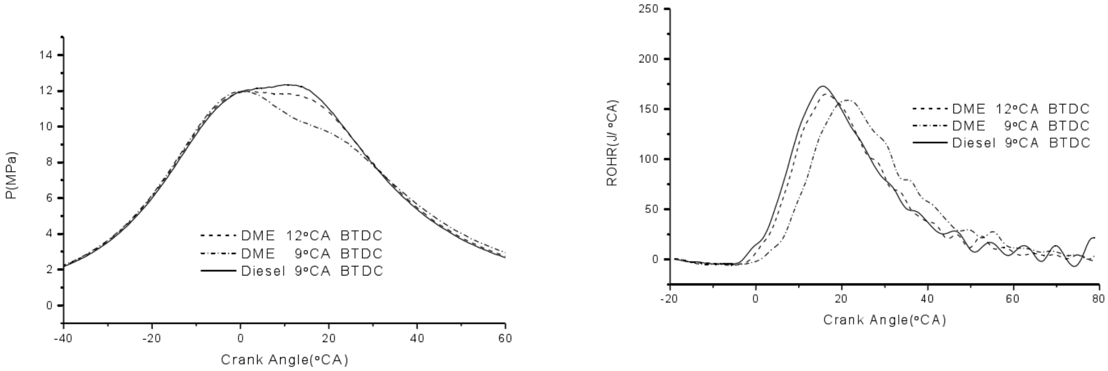

c) 2200 r/min Pe=1.21 MPa

Figure 1. Comparison of Cylinder Pressure and Heat Release Rate between DME Engine and Diesel Engine [19]

It can be seen from Figure 1 that the supercharged diesel engine has a high intake pressure and temperature, a short ignition delay period, less fuel to participate in premixed combustion, less heat released from premixed combustion, low premixed combustion heat release peak value, and high diffusion combustion heat release peak value. Due to the short ignition delay period of dimethyl ether, the heat released by premixed combustion is less, and the peak heat release of premixed combustion is lower than that of diesel engine.

To sum up, the injection delay angle of dimethyl ether is larger than diesel, the ignition delay period is shorter than diesel, and the maximum burst pressure, maximum pressure rise rate, and combustion noise are lower than diesel. The diffusion combustion speed of dimethyl ether is faster than that of diesel, and the combustion duration is shorter than that of diesel.

Emission Comparison between DME engine and Diesel engine

In 2004, Japan Institute of Industrial Technology (AIST) and Japan National Oil Corporation (JNOC) jointly conducted tests with different injection advance angles and engine speeds on a tandem pump diesel engine fueled with dimethyl ether [20]. The results showed that the maximum power and torque of the engine when fueled with dimethyl ether were equal to or greater than the original engine. Under the condition that NOx emission is maintained at the same level as that of the original engine, the thermal efficiency of DME at low and medium speed is often lower than that of diesel, and the thermal efficiency at high speed is equivalent to that of the original diesel.

Table 3. Emission Test Results of Dimethyl Ether Engine under Japanese 13 mode [21]

				[g/kWh]
	CO	HC	NOx	PM
Japanese 2003 limits	2.22	0.87	3.38	0.18
Diesel fuel operation	3.17	0.89	4.26	0.17
DME operation	0.117	0.222	4.26	0.0102
(Japanese 2003 regulation)	(-95%)	(-74%)	(-27%)	(-94%)

In 2004, Shinichi Goto of the Japanese Institute of Industrial Technology and Shinichi Suzuk of the Japanese oil company conducted an experimental study on a modified naturally aspirated diesel engine [21] using exhaust gas recirculation (EGR) and oxidation after treatment (DOC) technologies to burn dimethyl ether. Table 3 shows the emission results measured according to the Japanese 13 operating mode. Compared with the emission limit of Japanese 2003 regulations, NOx emissions decreased by 27%, CO decreased by 95%, HC emissions decreased by 74%, and particles emissions decreased by 94%.

In conclusion, the power performance of DME engine is superior to that of diesel engine. Under external characteristics, the fuel consumption rate of DME engine is lower than that of diesel engine at medium and low speed, and slightly higher at high speed. The NO_x emission of DME engine is significantly lower than that of diesel engine, the HC emission is also lower than that of diesel engine, and the CO emission is slightly higher than that of diesel engine. The HC and CO emissions of DME engine are at a very low level. In all operating conditions of the engine, the soot emission of the DME engine is zero. Dimethyl ether engine shows good performance and emission characteristics.

Advantages and Disadvantages of Dimethyl Ether as Diesel Engine Fuel

Through the research on the physical and chemical properties of dimethyl ether and the comparison between dimethyl ether and diesel oil, the following advantages and disadvantages are found [22]:

1) In the molecular formula of dimethyl ether, there are only C – H and C – O bonds, but no C – C bonds. The oxygen content is very high. Therefore, compared with diesel fuel, combustion will not produce soot, but also has good combustion effect and high thermal efficiency.

2) The cetane number of fuel is an important indicator of engine efficiency. The higher the cetane number, the stronger the ignition of fuel. The good ignition performance of dimethyl ether is due to its high cetane number, which ranges from 55 to 66, while that of diesel is only 40 to 55.

3) Dimethyl ether is a non petroleum energy and does not exist in nature, but it can be prepared from coal, natural gas and various biomass with low difficulty and easy preparation.

4) Dimethyl ether is easy to corrode rubber products during use, so it can only contact metal products directly during use and storage.

5) Under normal temperature and pressure, dimethyl ether is usually kept in a gaseous state. Based on this, in order to prevent dimethyl ether from vaporizing during combustion and affecting fuel performance, dimethyl ether needs to be pressurized. Generally, pressurize to 1.5 to 3 MPa and store dimethyl ether in liquid state.

6) Dimethyl ether is a colorless, non-toxic, non corrosive, non carcinogenic gas fuel. Due to its characteristics, it will not corrode metals, and its physical and chemical properties are stable. Even if it is placed in an aerobic environment for a long time, it will not produce oxidation reactions, and there will be oxides. Compared with propane and butane, dimethyl ether is extremely safe to use.

7) The calorific value of dimethyl ether is lower than that of diesel fuel, so more dimethyl ether is needed to achieve the same heat release as diesel fuel.

CONCLUSIONS

1. Dimethyl ether has high cetane number, low autoignition temperature and excellent compression characteristics, so it is suitable to replace diesel in compression ignition engines

2. The injection delay angle of dimethyl ether is larger than that of diesel, the ignition delay period is shorter than that of diesel, and the maximum explosion pressure, maximum pressure rise rate and combustion noise are lower than that of diesel. The diffusion combustion speed of dimethyl ether is faster than that of diesel, and the combustion duration is shorter than that of diesel.

3. The power performance of DME engine is better than that of diesel engine. Under external characteristics, the fuel consumption rate of DME engine is lower than that of diesel engine at medium and low speed, and slightly higher at high speed. The NOx emission of DME engine is significantly lower than that of diesel engine, the HC emission is also lower than that of diesel engine, and the CO emission is slightly higher than that of diesel engine. The HC and CO emissions of DME engine are at a very low level. In all operating conditions of the engine, the soot emission of the DME engine is zero. Dimethyl ether engine shows good performance and emission characteristics.

CONFLICTS OF INTEREST

The author declares that there is no conflict of interests regarding the publication of this paper.

REFERENCES

[1] Gao, J. (2019). *Study on Dynamic Mechanism of Dimethyl Ether Wide Range Combustion Frame.* Northwest University, Thesis.

[2] Shi, L. (2015). *Effect of dimethyl ether on combustion and emission of spark ignition engine.* Beijing University of Technology, Thesis.

[3] Tan, J., Huang, H., and He, T. (2009). Basic problems of regional operation research of alternative fuel vehicles. *Natural Gas Industry*, 29 (10), 128-132, 152.

[4] Han, Z. (2014). Rationality Analysis on Dimethyl Ether as Alternative Fuel. *Shandong Chemical Industry*, 2014 (3), 115-117.

[5] Wu, J. (2007). *Experimental Study on Combustion and Emission Control of Supercharged Dimethyl Ether Engine.* Shanghai Jiaotong University, Thesis.

[6] Thomas, G., Feng, B., Veeraragavan, A., Cleary, M. J., and Drinnan, N. (2014). Emissions from DME combustion in diesel engines and their implications on meeting future emission norms: A review. *Fuel Processing Technology*, 119, 286-304. DOI: https://doi.org/10.1016/j.fuproc.2013.10.018

[7] Kim, H. J., and Park, S. H. (2016). Optimization study on exhaust emissions and fuel consumption in a dimethyl ether (DME) fueled diesel engine. *Fuel*, 182, 541-549. DOI: https://doi.org/10.1016/j.fuel.2016.06.001

[8] Park, S. H., and Lee, C. S. (2014). Applicability of dimethyl ether (DME) in a compression ignition engine as an alternative fuel. *Energy Conversion and Management*, 86, 848-863. DOI: https://doi.org/10.1016/j.enconman.2014.06.051

[9] Li, G. B. (2011). Dimethyl Ether (DME): A New Alternative Fuel for Diesel Vehicle. *Advanced Materials Research*, 156-157, 1014-1018. DOI: 10.4028/www.scientific.net/AMR.156-157.1014

[10] Arcoumanis, C., Bae, C., Crookes, R., and Kinoshita, E. (2008). The potential of di-methyl ether (DME) as an alternative fuel for compression-ignition engines: A review. *Fuel*, 87(7), 1014-1030. DOI: https://doi.org/10.1016/j.fuel.2007.06.007

[11] Semelsberger, T. A., Borup, R. L., and Greene, H. L. (2006). Dimethyl ether (DME) as an alternative fuel. *Journal of Power Sources*, 156(2), 497-511. DOI: https://doi.org/10.1016/j.jpowsour.2005.05.082

[12] Bae, C., and Kim, J. (2017). Alternative fuels for internal combustion engines. *Proceedings of the Combustion Institute*, 36(3), 3389-3413. DOI: https://doi.org/10.1016/j.proci.2016.09.009

[13] Chen, Y., Ma, J., Han, B., Zhang, P., Hua, H., Chen, H., and Su, X. (2018). Emissions of automobiles fueled with alternative fuels based on engine technology: A review. *Journal of Traffic and Transportation Engineering (English Edition)*, 5(4), 318-334. DOI: https://doi.org/10.1016/j.jtte.2018.05.001

[14] Panigrahy, S., and Mishra, S. C. (2018). The combustion characteristics and performance evaluation of DME (dimethyl ether) as an alternative fuel in a two-section porous burner for domestic cooking application. *Energy*, 150, 176-189. DOI: https://doi.org/10.1016/j.energy.2018.02.121

[15] Ju, D., Zhang, T., Xiao, J., Qiao, X., and Huang, Z. (2015). Effect of droplet sizes on evaporation of a bi-component droplet at DME (dimethyl ether)/n-heptane-fueled engine conditions. *Energy*, 86, 257-266. DOI: https://doi.org/10.1016/j.energy.2015.04.030

[16] Park, S. H., Kim, H. J., and Lee, C. S. (2010). Effects of dimethyl-ether (DME) spray behavior in the cylinder on the combustion and exhaust emissions

characteristics of a high speed diesel engine. *Fuel Processing Technology*, 91(5), 504-513. DOI: https://doi.org/10.1016/j.fuproc.2009.12.013

[17] Zhang, J. (2009). *Combustion and emission characteristics and performance optimization of dimethyl ether engine*. Shanghai Jiaotong University, Thesis.

[18] Li, D., Huang, Z., Qiao, X., Luo, L., and Peng, X. (2005). Study on homogeneous compression ignition combustion of dimethyl ether fuel. *Journal of Internal Combustion Engine*, 23 (3), 6.

[19] Zhang, C., Yang, Q., and Hu, Z. (2004). Experimental Study on ZS195 Diesel Engine Fueled with DME Diesel Blends. *Journal of Internal Combustion Engine*, 22 (004), 305-309.

[20] Oguma, M., Goto, S., and Watanabe, T., (2004). Engine Performance and Emission Characteristics of DME Diesel Engine With Inline Injection Pump Developed for DME. *SAE Technical Paper 2004-01*-1863. DOI: https://doi.org/10.4271/2004-01-1863

[21] Sun, Y. (2014). *Numerical Simulation Study on the Effects of Hydrogen and Dimethyl Ether Blending in Intake Air on Diesel Engine Combustion and Emissions*. Dalian University of Technology, Thesis.

[22] Wu, J. (2016). Experimental Study on Improving Fuel Economy of Dimethyl Ether Engine. *Journal of Wuhan University of Science and Technology*, 39 (1), 4.

Trends in Renewable Energy
OPEN ACCESS **ISSN: 2376-2144**
Peer-Reviewed Article
futureenergysp.com/index.php/tre

Current Status of Research on Biodiesel as an Alternative Fuel for Internal Combustion Engines

Ganli Liu

School of Mechanical Engineering/Institute of Vehicles and New Energy Technology, North China University of Water Resources and Electric Power, Zhengzhou City, Henan, China

Received September 17, 2022; Accepted November 12, 2022; Published November 27, 2022

In this paper, the research on biodiesel or blending with other fuels is reviewed. Based on the current status of biodiesel research, this paper introduces the current research progress, combustion and emission characteristics, blending with other fuels, and development direction of biodiesel. The combustion, emission, and spray of biodiesel are not exactly the same as diesel, so it is not suitable to be used directly in diesel engines. Biodiesel can be blended with diesel, ethanol, ammonia and other fuels to improve its power performance and reduce harmful emissions. This review can serve as an important reference for those who want to engage in biodiesel research, and a quick understanding of biodiesel research before.

Keywords: Renewable Energy; Alternative fuels; Biodiesel; Combustion; Emission; Spraying characteristics

Introduction

With the development of society, the total energy consumption is increasing. At present, the primary energy used in the world mainly includes fossil energy such as crude oil, coal and natural gas, among which crude oil accounts for more than one-third of the total global energy consumption [1] (as shown in Fig.1). China's limited oil reserves and heavy reliance on overseas imports have become an important issue affecting China's energy security. In the field of transportation, such as automobiles, ships and aviation, oil consumption accounts for more than 50% of the total consumption [2]. According to the statistical analysis of the China Association of Automobile Manufacturers [3], the production and sales of automobiles increased by 4.15~5.57 % year-on-year. Among them, commercial vehicles which mainly use diesel engines, increased by 9.41~10.58 % year-on-year. With the further improvement of China's economic level, China's fuel consumption will continue to grow in the coming period. Figure 1 shows the graph of crude oil consumption and crude oil production in China in recent years, which shows that China's fuel energy gap is gradually expanding.

The internal combustion engine will remain the primary source of power in automobiles for the foreseeable future, and the growth in vehicle sales has increased the consumption of oil [4]. The huge production of automobiles also increases the burden on the environment, which is more obvious in commercial vehicles. Diesel engines have high power and durability and are widely used in trucks and medium to large buses. However, the diffusion combustion method of diesel as a heavy oil makes the fuel

**Corresponding author:* 812524678@qq.com

Tr Ren Energy, 2023, Vol.9, No.1, 11-21. doi: 10.17737/tre.2023.9.1.00146

unevenly distributed in space, forming a considerable proportion of combustion-rich areas and leading to the generation of large amounts of particulate matter. In addition, the uneven distribution of fuel also makes the formation of higher temperature peaks in the combustion chamber, generating more NO_x, and the combustion emissions of diesel engines also generate CO, hydrocarbons (THC), etc. To cope with these problems, countries around the world have developed strict emission regulations [5]. For example, Europe began to implement Euro V vehicle emission standards in 2009. In 2019, China began to implement national V vehicle emission standards nationwide. Technological innovations in internal combustion engines also contribute to the reduction of pollutant emissions and oil consumption, and are divided into three main categories [6]. The first type is to change the internal combustion method of the engine, such as the use of exhaust gas recirculation system in diesel engines to re-burn the exhaust gas and thus reduce the NO_x in the exhaust gas. The second type of pollutant purification technology is the addition of catalysts to the exhaust process to achieve the purpose of purification, such as the three-way catalytic technology already used in gasoline engines, which greatly reduces NO_x and THC emissions. The third category is the search for green and renewable alternative fuels for internal combustion engine fuel, including ethanol, dimethyl ether, biodiesel, etc. The development of alternative fuels for internal combustion engines and the establishment of a diversified energy supply system will not only help to improve engine emissions, but also further reduce dependence on petroleum.

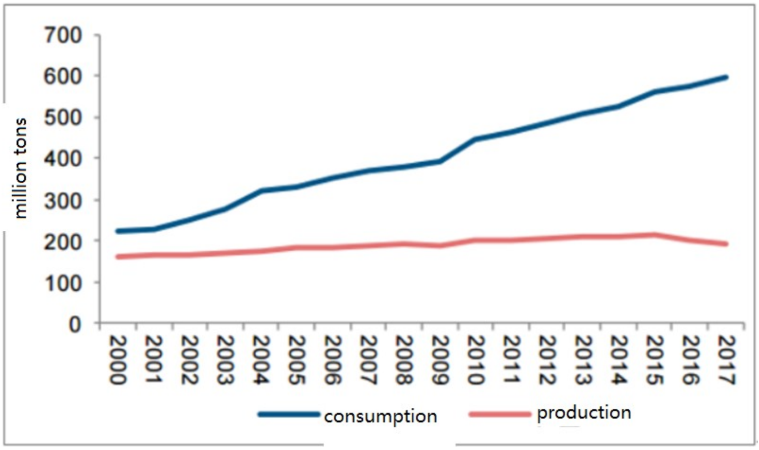

Fig. 1. China's oil consumption and production in recent years [1]

As a renewable green energy, biodiesel is widely valued in all countries around the world. Based on the current status of biodiesel research, this paper introduces the current research progress, combustion and emission characteristics of biodiesel, blending with other fuels, and development direction of biodiesel. This paper is an important reference for those who want to engage in biodiesel research and a quick understanding of biodiesel research.

Physical and Chemical Properties of Biodiesel

Biodiesel is a methyl ester or ethyl ester fuel made from oilseed crops, wild oilseed plants, aquatic plant oils (like engineered microalgae), animal fats and grease, and restaurant waste oil, etc. This fuel can be synthesized through an ester exchange process.

There are more than 30 kinds of vegetable oil-based biodiesels known to be used in internal combustion engines, and their main characteristics are as follows [7].
(1) The calorific value of biodiesel is lower than diesel. But the density is higher than diesel, and the volumetric calorific value is similar to diesel. So, the engine oil supply system almost does not need to be changed.
(2) The viscosity of biodiesel is higher than diesel, which affects the spraying characteristics and cold starting performance. But the viscosity of vegetable oil decreases faster with the increase of temperature.
(3) The cetane number of biodiesel is lower than diesel. The flash point and ignition temperature of biodiesel are worse than diesel. When used in diesel engine, it generally needs to increase the injection advance angle.
(4) Biodiesel generally contains oxygen, which is good for combustion.
(5) Biodiesel can be mixed with diesel in any ratio.
(6) Biodiesel contains small amount of water, ash, carbon residue and impurities.
(7) The main component of biodiesel is unsaturated fatty acid, which is easy to oxidize and deteriorate easily.

Combustion, Spraying, Power Economy and Emission Characteristics of Biodiesel

Combustion Characteristics

The physical parameters of biodiesel are close to those of conventional diesel. Biodiesel and diesel have good miscibility, so it can be blended with conventional diesel in any ratio and used directly in existing engines. However, the combustion characteristics of biodiesel and diesel in engines are very different, which depends on the physical and chemical properties of biodiesel and blending concentration. Many scholars have conducted a lot of related researches. In terms of the output power, the maximum output power of biodiesel is slightly lower than that of diesel, because the calorific value of biodiesel is lower than that of diesel. Sinha and Agarwal [8] reported that when using lower concentrations of rice bran biodiesel (B5, B10 and B20), the maximum engine output was equal to or slightly higher than that of the diesel engine. The evaporative characteristics of the fuel, the viscosity, and the oxygen content of the biodiesel all affected the exothermic rate of the combustion process, especially at high rpm. The lower biodiesel concentration increased the output power of the tested engine, and the degree of influence is shown in Figure 2.

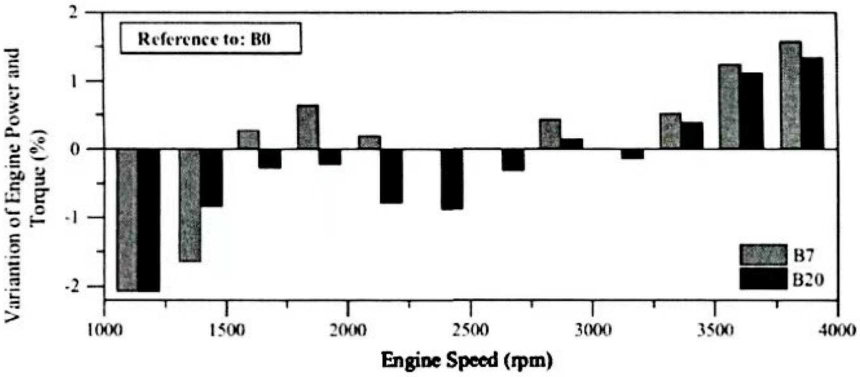

Fig. 2. Effect of biodiesel blends on engine output power and torque [8]

In terms of engine thermal efficiency, most studies reported that the thermal efficiency of biodiesel and its blends is higher than that of diesel, mainly related to the blending ratio, fuel oxygen content, fuel viscosity and density. For example, *Mahanta et al.* [9] reported that the thermal efficiency of B20 biodiesel was higher than that of diesel fuel due to the oxygen atoms of biodiesel that contributed to more adequate combustion of the fuel in the combustion chamber. Agarwal [10] tested the effect of different blending ratios of biodiesel relative to diesel fuel on the peak engine thermal efficiency (as shown in Figure 3) and found that the B20 blend had the highest thermal efficiency. Du *et al.* [11] pointed out that the thermal efficiency of biodiesel, biodiesel-ethanol and biodiesel-methanol blends were higher than that of diesel at all operating conditions. This is due to the small amount of ethanol in the fuel blend that improves the combustion characteristics of the fuel. In addition, the use of higher injection pressure can improve the atomization characteristics of biodiesel droplets and increase the thermal efficiency of the fuel.

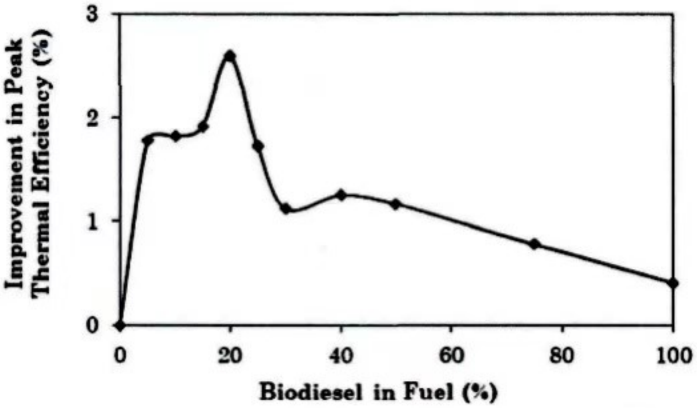

Fig. 3. Effect of biodiesel blending ratio on the improvement of peak thermal efficiency [10]

Emission Characteristics

China's latest National VI standard makes further restrictions on pollutant emissions, in which the emission requirements for CO and THC (Total Hydro Carbons) are reduced by one-third compared to National V, and the overall pollutant limits are 40-50% stricter compared to National V [12]. For biodiesel, the emissions of THC, CO, and PM decreased with the increase of blending ratio, while NO_x increased slightly [13-16]. Grimaldi *et al.* [17] reported that the CO emissions of biodiesel were similar to those of diesel at 2500 rpm of the engine, and the CO emissions of biodiesel decreased significantly at 4000 rpm of the engine speed. Gumus *et al.* [18] observed that CO emissions decreased as the biodiesel blend percentage increased, and that CO emissions decreased with increasing injection pressure in the engine for all biodiesel blends. THC emissions are affected by feedstock and fuel properties such as oxygen content, cetane number, engine injection pressure, fuel injection time delay, etc. Su *et al.* [19] showed that biodiesel blends emit significantly lower THC emissions at full load compared to diesel. Gumus *et al.* also [18] studied the THC emissions of biodiesel at different blending ratios and injection pressures and found that the THC emissions decreased with increasing biodiesel blending ratio and fuel injection pressure (as shown in Figure 4).

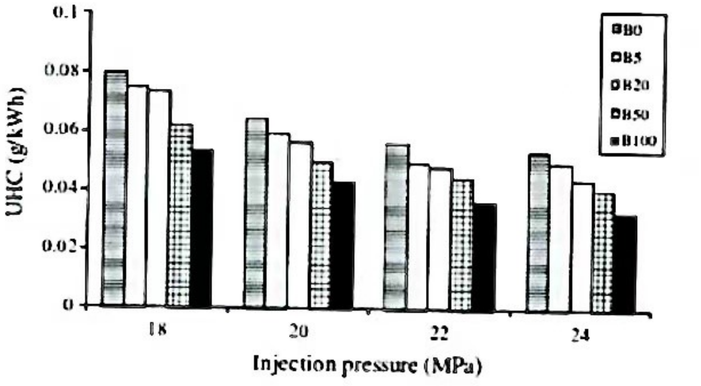

Fig. 4. Variation of THC emission with injection pressure [18]

Most relevant studies have shown that biodiesel produces higher NO_x than diesel in unmodified engines. Gimuis *et al.* [20] concluded that NO_x emissions increase with increasing engine load due to higher peak combustion chamber temperatures. Sharp *et al.*[21] investigated the relationship between NO_x emissions and fuel performance, showing that NO_x emissions decreased with increasing fuel oxygen content in the test fuel and increased with increasing carbon chain length. Mueller *et al.* [22] concluded that the increase in NO_x in biodiesel engines cannot be quantified by changes in a single fuel performance. Rather, it is the result of many coupled mechanisms whose effects enhance or cancel each other under different conditions.

In terms of particulate matter (PM) emissions (e.g., Figure 5), Lapuerta *et al.* [23] tested PM emissions from four biodiesels in a 2.2 L turbo diesel engine and showed that all four biodiesels emitted substantially less PM than diesel. The Dhar and Agarwal [24] study noted that PM emissions from both B20 and B50 were lower than those from diesel, and that as injection pressure increased, particulate matter particle size decreased.

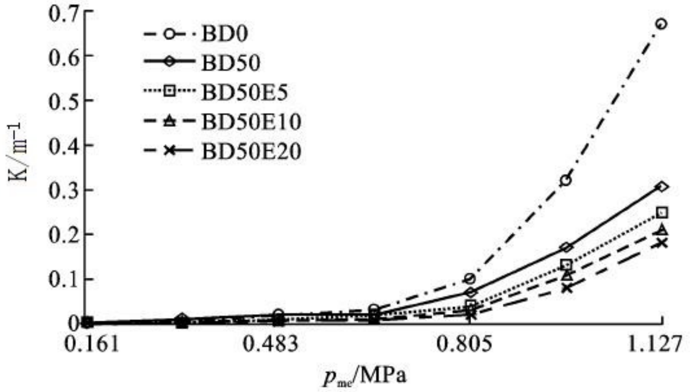

Fig. 5. Variation of the PM emission [23]

Spraying Characteristics

The most important factor affecting engine combustion is the quality of the in-cylinder fuel-air mixture. The formation of the mixture is closely related to the in-cylinder environment, the spray characteristics of the fuel, and the atomization effect. The spray characteristics of biodiesel are an important factor affecting its operation and emission in the engine [25]. From the above review, it can be seen that the engine injection pressure, atomization method and the physical parameters of biodiesel itself will directly affect the combustion and working characteristics of the fuel in the engine, which in turn determines the fuel economy and emission performance of the engine. Therefore, the spray characteristics of biodiesel in diesel engines are the key factors affecting the efficient and clean combustion of the engine. Compared with diesel fuel, the density, viscosity and surface tension of biodiesel are larger, which will directly affect the spray characteristics of biodiesel in engines. Among them, the viscosity affects the fuel flow at different temperatures and the spray parameters when the fuel is injected into the combustion chamber, which may eventually lead to deposits in the engine, especially at higher viscosities. Many studies in the literature have shown that the viscosity of biodiesel tends to decrease non-linearly with increasing temperature, but remains higher than that of diesel [26]. Density is also an important physical parameter of biodiesel and has a more significant effect on the macroscopic spray characteristics of the fuel. During the spraying process, denser fuels have higher momentum and tend to produce larger spray penetration and collision with the piston, so the density of biodiesel needs to be controlled in practical use. For example, the density of biodiesel at room temperature is limited to the range of 860~900 kg/m^3 in Europe. Knothe *et al.* [27] studied the density variation trend of biodiesel in the range of 15~40°C and derived the correlation equation. In addition, the surface tension of the liquid affects the droplet formation and fragmentation during the spraying process, which in turn affects the atomization characteristics of the fuel. The surface tension of biodiesel is higher than that of diesel, which is not conducive to the breaking into fine droplets during the spraying process and affects the atomization characteristics of biodiesel. Lee *et al.* [28] investigated the spray penetration, soot mean diameter (SMD) and mean velocity distribution of biodiesel blends. The results showed that the biodiesel blends had similar spray development trends as diesel, but were larger due to the higher viscosity and surface tension of biodiesel. Han *et al.* [29] studied the spray characteristics of three components of biodiesel, methyl laurate, methyl oleate and ethyl oleate, and the results showed that methyl oleate and ethyl oleate produced larger spray penetration distances due to their higher viscosity and surface tension (as shown in Figure 6). Cao *et al.* [30] investigated the spray characteristics of biodiesel blends with non-edible oils, and the results showed that the spray penetration and spray velocity increased and the spray cone angle decreased as the percentage of biodiesel in the blends increased. The macroscopic spray characteristics of biodiesel-diesel blends with different blending ratios were investigated by Xie *et al.* [31]. The results indicated that the spray cone angle increased and the spray penetration and peak tip velocity decreased with increasing ambient pressure. It was also found that the higher viscosity and surface tension of biodiesel inhibited the fragmentation of the liquid jet.

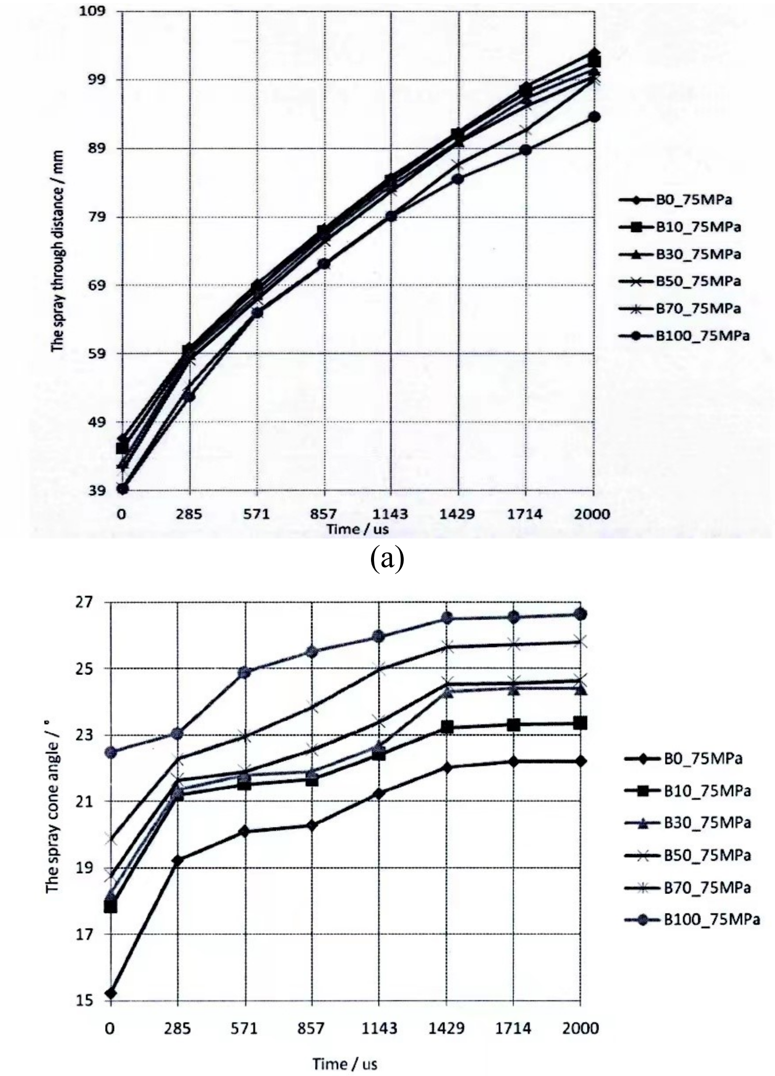

(a)

(b)

Fig. 6. Comparison of different biodiesel macro spray parameters with diesel [27]

Blending and Combustion of Biodiesel with Other Fuels

Biodiesel has the characteristics of higher viscosity and lower calorific value [32]. This makes the fuel consumption of engines burning biodiesel higher than that of diesel. And the thermal efficiency is reduced. Therefore, many researchers have used biodiesel blended with other fuels to improve the fuel properties of biodiesel [33].

Qiu *et al.* [34] blended biodiesel with different proportions of ammonia for combustion simulation. Their simulation results show that biodiesel blended with a certain amount of ammonia can promote combustion, which can improve engine performance and reduce harmful emissions. However, the engine power is slightly reduced with the addition of ammonia. Zuo *et al.* [35] conducted experiments on biodiesel-diesel blends. They found that the ignition point of biodiesel-diesel blends was earlier than diesel at full load. Due to the advanced ignition point, the maximum cylinder pressure and peak exothermic rate of biodiesel-diesel blends are lower than that of diesel during the main combustion phase. Geng *et al.* [36] experimented the addition of 5%, 10% and 20% ethanol to biodiesel-diesel blends. The results show that the maximum in-cylinder pressure and the maximum instantaneous heat release rate of the blended fuel are higher than those of diesel fuel at small loads. With the increase of ethanol blending ratio, the NO_x and HC emissions of biodiesel-diesel-ethanol blends increased slightly. But they were lower than the emission level of diesel.

CONCLUSIONS

In summary, several conclusions can be drawn as follow:
1) The combustion, emission, and spray of biodiesel are not exactly the same as diesel, so it is not suitable to be used directly on diesel engines.
2) Biodiesel can be blended with diesel, ethanol, ammonia and other fuels to improve its power performance and reduce harmful emissions.
3) The current studies on biodiesel are mostly based on the external conditions of combustion and the blending combustion between different fuels. There is a relative lack of studies to describe the combustion process from the chemical reaction kinetics perspective. The study of the combustion process of fuels from the chemical reaction kinetics point of view allows to obtain the fundamental reactions that play an important role in in-cylinder combustion. Therefore, the study of the combustion process from the chemical reaction kinetics point of view is a new direction.

CONFLICTS OF INTEREST

The author declares that there is no conflict of interests regarding the publication of this paper.

REFERENCES

[1] Graham-Rowe, D. (2011). Agriculture: Beyond food versus fuel. *Nature*, 474(7352), S6-S8. DOI: 10.1038/474S06a
[2] Dale, S. (2021). BP statistical review of world energy. *BP Plc, London, United Kingdom*, 14-16. https://www.imemo.ru/files/File/ru/events/2021/BP-2021.pdf (accessed on 11/21/2022)
[3] China Association of Automobile Manufacturers. (2018). *China Automobile Industry Production and Sales Statistics*. http://auto-stats.org.cn/ (accessed on 11/21/2022)
[4] China National Energy Administration. (2014). *Biodiesel Industry Development Policy*. http://sdb.nea.gov.cn/Upload/main/ContentManage/Article/File/2021/03/17/202103171238513623.doc (accessed on 11/21/2022)
[5] Song, J.Y., and Mao, K.L. (2019). Recent trends of biodiesel fuel and its feedstock in Europe. *Applicable Chemistry*, 44(08), 1515-1519.
[6] Liu, Z.C., Xu, S.H., and Yao, R. J. (2021). *Properties and applications of liquid fuels*. China Petrochemical Press, Beijing.

[7] Wang, L.B., Hai-Yan, Y.U., Xiao-Hui, H.E., and Liu, R.Y. (2018). Influence of fatty acid composition of woody biodiesel plants on the fuel properties. *Journal of Fuel Chemistry and Technology*, 40(4), 397-404.

[8] Sinha, S., and Agarwal, A.K. (2005). Performance evaluation of a biodiesel (rice bran oil methyl ester) fuelled transport diesel engine. *SAE technical paper*, *1*, 1730.

[9] Mahanta, P., Mishra, S. C., and Kushwah, Y. S. (2006). An experimental study of Pongamia pinnata L. oil as a diesel substitute. *Proceedings of the Institution of Mechanical Engineers, Part A: Journal of Power and Energy*, 220(7), 803-808.

[10] Agarwal, D. (2019). *Experimental study and simulation optimization of biodiesel/ethanol blended fuel internal combustion engine*. Huazhong University of Science and Technology, Thesis.

[11] Du, J., Dai, P., Xu, X., Mei, D., Wu, H., Chen, C., and Tao, J. (2017). Combustion process in a diesel engine using diesel blends with short-chain ethanol and ester. *Journal of Yangzhou University (Natural Science Edition*). 20(4), 42-46. DOI: 10.19411/j.1007-824x.2017.04.010

[12] Dong, Y., Lin, L., and Xu, B. (2017). Preparation of diesel-ethanol emulsified fuel with soybean phospholipids as emulsifier. *China Oils and Fats*, 32(12), 41-44. DOI: 10.3321/j.issn:1003-7969.2007.12.012

[13] Liu, S.H., and Zhou, L.B. (2017). *Internal Combustion Mechanics*, 4th Edition. Mechanical Industry Press, Beijing.

[14] Yuan, Y., Gu, M., Dai, P., and Mei, D. (2017). Catalytic transfer hydrogenation of biodiesel to improve its combustion characteristics. *Transactions of the Chinese Society of Agricultural Engineering*, 33(11), 54-59.

[15] Fu, W. (2019). *Study on the spray characteristics of biodiesel and its fuel blends*. University of Science and Technology of China, Thesis.

[16] Li, L. (2020). *Experimental study and theoretical analysis of ethanol/biodiesel combustion process*. Jiangsu University, Thesis.

[17] Grimaldi, C. N., Postrioti, L., Battistoni, M., and Millo, F. (2002). Common rail HSDI diesel engine combustion and emissions with fossil/bio-derived fuel blends. *SAE Transactions*, 1453-1461.

[18] Gumus, M., Sayin, C., and Canakci, M. (2011). The impact of fuel injection pressure on the exhaust emissions of a direct injection diesel engine fueled with biodiesel–diesel fuel blends. *Fuel*, 95, 486-494. DOI: https://doi.org/10.1016/j.fuel.2011.11.020

[19] Su, P., Zhang, R., and Mei, D. (2019). Thermogravimetric analysis of ethanol diesel and its emission characteristics. *Transactions of the Chinese Society of Agricultural Engineering*, 29(16), 50-56.

[20] Pradelle, F., Leal Braga, S., Fonseca de Aguiar Martins, A. R., Turkovics, F., and Nohra Chaar Pradelle, R. (2019). Experimental assessment of some key physicochemical properties of diesel-biodiesel-ethanol (DBE) blends for use in compression ignition engines. *Fuel*, 248, 241-253. DOI: https://doi.org/10.1016/j.fuel.2019.03.087

[21] Sharp, C.A., Ryan III, T.W., and Knothe, G. (2005). Heavy-duty diesel engine emissions tests using special biodiesel fuels. *SAE transactions*, 114, 1204-1212.

[22] Mueller, C.J., Boehman, A.L., and Martin, G.C. (2009). An experimental investigation of the origin of increased NOx emissions when fueling a heavy-duty

compression-ignition engine with soy biodiesel. *SAE International Journal of Fuels and Lubricants*, 2(1), 789-816.

[23] Lapuerta, M., Armas, O., and Rodríguez-Fernández, J. (2008). Effect of biodiesel fuels on diesel engine emissions. *Progress in Energy and Combustion Science*, 34(2), 198-223. DOI: https://doi.org/10.1016/j.pecs.2007.07.001

[24] Singh Chouhan, A. P., Singh, N., and Sarma, A. K. (2013). A comparative analysis of kinetic parameters from TGDTA of Jatropha curcas oil, biodiesel, petroleum diesel and B50 using different methods. *Fuel*, 109, 217-224. DOI: https://doi.org/10.1016/j.fuel.2012.12.059

[25] Attia, A. M. A., Nour, M., and Nada, S. A. (2018). Study of Egyptian castor biodiesel-diesel fuel properties and diesel engine performance for a wide range of blending ratios and operating conditions for the sake of the optimal blending ratio. *Energy Conversion and Management*, 174, 364-377. DOI: https://doi.org/10.1016/j.enconman.2018.08.016

[26] Pires de Oliveira, I., Caires, A. R. L., Baskar, K., Ponnusamy, S., Lakshmanan, P., and Veerappan, V. (2020). Biodiesel as an additive for diesel-ethanol (diesohol) blend: physical-chemical parameters and origin of the fuels' miscibility. *Fuel*, 263, 116753. DOI: https://doi.org/10.1016/j.fuel.2019.116753

[27] Pedrozo, V. B., May, I., Guan, W., and Zhao, H. (2018). High efficiency ethanol-diesel dual-fuel combustion: A comparison against conventional diesel combustion from low to full engine load. *Fuel*, 230, 440-451. DOI: https://doi.org/10.1016/j.fuel.2018.05.034

[28] Kim, H., Kim, Y., and Lee, K. (2013). An Experimental Study on the Spray, Combustion, and Emission Characteristics of Two Types of Biodiesel Fuel. *Energy & Fuels*, 27(9), 5182-5191. DOI: 10.1021/ef400936a

[29] Han, D., Zhai, J., Duan, Y., Ju, D., Lin, H., and Huang, Z. (2017). Macroscopic and microscopic spray characteristics of fatty acid esters on a common rail injection system. *Fuel*, 203, 370-379. DOI: https://doi.org/10.1016/j.fuel.2017.04.098

[30] Cao, Y., Liu, Y., Hu, N., Hu, X., Zhang, Y., Zhao, Y., and Wu, A. (2019).Current Status and Prospects of Fuel Ethanol Production. *Biotechnology Bulletin*, 35(4), 163-169.

[31] Li, X., Xie, D., Wang, Y., and Zhang, Y. (2011). Study on the solubility of diesel-biodiesel-ethanol and its blending fuel properties. *Applied Chemical Industry*, 40(3), 376-380, 386. DOI: 10.3969/j.issn.1671-3206.2011.03.002

[32] Mei, D., Sun, C., Gu, M., Zhang, Q., and Yuan, Y. (2017). Physical and chemical properties and thermogravimetric performance of hydrogenated biodiesel. *Energy Sources, Part A: Recovery, Utilization, and Environmental Effects*, 39(16), 1739-1745. DOI: 10.1080/15567036.2017.1347731

[33] Xiao, J.C. (2022). *Chemical kinetic mechanism of biodiesel combustion process*. Nanchang University, Thesis.

[34] Qiu, Y., Wei, H., Wei, L., Li, J., Zhou, D., Wu, G., and Li, C. (2022). Effect of ammonia blending of biodiesel on combustion and emission performance of homogeneous compression-ignition engines. *China Oils and Fats*, 31(10), 19-25. DOI: 10.19902/j.cnki.zgyz.1003-7969.210805

[35] Zuo, L., Mei, D.Q., Zhang, D.P., Dai, S., and Wang, J. (2020). Combustion and emission characteristics of hydrogenated biodiesel-ethanol-diesel in high-pressure common rail diesel engines. *Journal of Xi'an Jiaotong U*niversity, 54(9), 189-196.

[36] Geng, L. (2021). Analysis of physicochemical properties and improvement of spray characteristics of biodiesel-diesel blends. Xi'an: Chang'an University, Thesis.

Trends in Renewable Energy
OPEN ACCESS **ISSN: 2376-2144**
Peer-Reviewed Review Article
futureenergysp.com/index.php/tre

Current Status of Research on Methanol as an Alternative Fuel to Conventional Fuels

Dongchao Lan

School of Mechanical Engineering/Institute of Vehicles and New Energy Technology, North China University of Water Resources and Electric Power, Zhengzhou City, Henan, China

Received September 20, 2022; Accepted November 13, 2022; Published December 11, 2022

With the rapid development of China's economy and society, the domestic demand for automobiles is growing explosively. At the same time, the dependence of China's crude oil on foreign countries exceeds 65%. This is a great hidden danger to the sustainable development of China's economy and energy security. Automobile consumes a large amount of petroleum resources, and automobile exhaust is one of the main factors causing environmental pollution. In view of the dual pressure of energy saving and emission reduction, methanol has been favored by many researchers for its many advantages (such as cleanliness, environmental protection, renewable and high accessibility). In this paper, the resource extensibility of methanol, the physicochemical properties of methanol, the application characteristics of methanol in internal combustion engine and the comparison of the combustion performance of methanol with traditional fuels are summarized and analyzed.

Keywords: Energy crisis; Environmental pollution; Methanol; Combustion characteristic

Introduction

With the rapid development of China's economy, automobiles and engineering and transportation vehicles become explosive growth, which will bring energy crisis and environmental pollution and other problems [1-2]. According to the analysis of data released by “World Energy Statistical Yearbook 2022”, China's oil production will be equal to China's oil consumption in 2022. From Figure 1, it can be seen that China's oil production has not changed much, but its oil consumption has been rising [3]. Along with the growth of chemical energy consumption, the problem of environmental pollution has become more and more serious, according to the data from the Annual Report on Environmental Management of Mobile Sources in China in 2021, in 2020, the national emissions of carbon monoxide (CO), hydrocarbons (HC), nitrogen oxides (NO_x), and particulate matter (PM) from automobiles are 6.938 million tons, 1.724 million tons, 6.137 million tons, and 6.4 million tons, respectively. It can be seen from Fig. 1 that diesel vehicles emit more than 80% of the total vehicle emissions of nitrogen oxides (NO_x) and more than 90% of the particulate matter (PM), while gasoline vehicles emit more than 80% of the total vehicle emissions of carbon monoxide (CO) and more than 70% of the hydrocarbons (HC) [4].

**Corresponding author:* 857568152@qq.com

Tr Ren Energy, 2023, Vol.9, No.1, 22-33. doi: 10.17737/tre.2023.9.1.00147

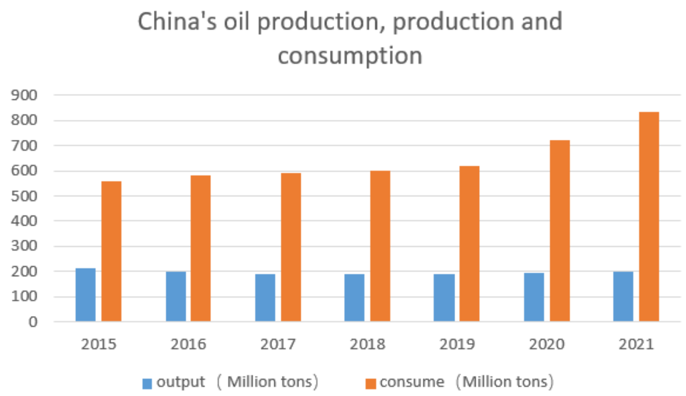

Fig. 1. China's oil production versus consumption [3]

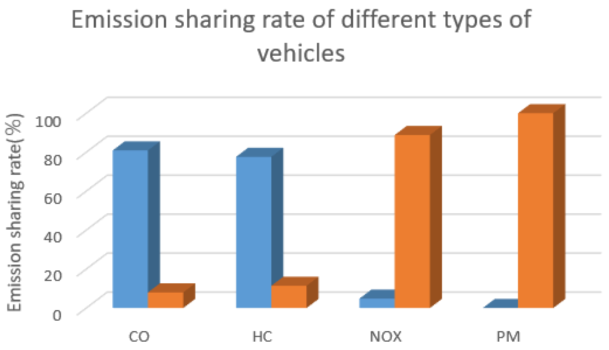

Fig. 2. Pollutant emission share of vehicles by fuel types [3]

In order to solve the problems of fossil energy shortage and environmental pollution, the search for clean and renewable energy has become an urgent need. Methanol, as one of many alternative fuels, has attracted a lot of attention in recent years by virtue of its wide source and versatility. Methanol has distinctive characteristics compared to traditional fossil fuels [5-6]. For example, it has high octane number and good anti-detonation property, which can increase the engine compression ratio to improve engine performance and reduce fuel consumption. It has high latent heat of vaporization and lower combustion temperature in the engine, which helps to reduce heat loss and NO_x emission [7-8]. However, the low cetane number of methanol makes it difficult for direct compression ignition in compression-ignition engines, and other auxiliary means are needed to help its ignition and combustion [9]. The high lower ignition concentration limit, low vapor pressure, and high latent heat of vaporization of methanol all make cold starting of methanol-fueled engines difficult and prone to formaldehyde and unburned methanol emissions. Although there are still many problems to be solved in burning methanol in internal combustion engines, methanol is still considered as one of the most promising alternative fuels [10-12].

Sources and Physicochemical Properties of Methanol

Sources of Methanol

Methanol feedstock comes from a wide range of sources and mature production processes, which is mainly through coal chemical and natural gas synthesis. The main sources include coal, natural gas, coal bed methane, and biomass [13]. Most of the coal used for methanol production in China is poor quality coal with high sulfur content, which has low production cost. Meanwhile, it can be desulfurized during the production process, which is conducive to environmental protection, and can also yield by-products such as sulfur and urea [14].

Physical and Chemical Properties of Methanol

Table 1 shows a comparison of some physical parameters of methanol with gasoline and diesel. It can be found that the latent heat of vaporization of methanol is four times higher than that of gasoline and diesel, and the evaporation process will absorb more heat and lower the average temperature in the cylinder. Methanol has a high auto-ignition temperature, so it is difficult to directly compress and ignite, and auxiliary means are needed to help methanol ignite. Methanol has a small molecular weight, a simple chemical structure, a low carbon to hydrogen ratio, and contains its own oxygen, so it is easier to burn completely, which helps to reduce CO and HC emissions. It is theoretically possible to burn methanol in diesel engines without generating carbon smoke [15-18].

Table 1. Comparison of the main property parameters of methanol with gasoline and diesel

Nature/Unit	Methanol	Petrol	Diesel
Chemical formula	CH_3OH	C16~C23	C16~C23
Freezing point (°C)	-96	-57	-1~-4
Boiling point (°C)	64.7	27~225	180~370
Flash point (°C)	12	45	75
Natural temperature (°C)	500	350~468	270~350
Latent heat of vaporization (kg/kJ)	1167	310	270
Low calorific value (kJ/kg)	19930	43030	42500
Octane number (MON)	94.6	81~84	-
Cetane number	3	0~10	45~55
Theoretical mass to air-fuel ratio	6.5	14.8	14.6

From Table 1, it is known that methanol as an alternative fuel for internal combustion engines has the following main characteristics.

(1) Compared with gasoline and diesel, methanol has a lower freezing point and can be used in lower climates.

(2) The high latent heat of vaporization of methanol, the lower vapor pressure and boiling point will make the cold start of the engine difficult. On the other hand, it will also lower the intake temperature and increase the charge factor of the engine [19].

(3) The oxygen content and ignition limit of methanol are higher, and the dilute combustion characteristics are better, so that the engine has a larger working condition coverage. Especially in gasoline engines, it will reduce the chance of misfire due to imprecise control of air-fuel ratio causing too lean combustible mixture. The laminar flame speed of methanol is faster, and the combustion rate in engines is higher than that of gasoline, which can improve the isotonicity of in-cylinder combustion [20].

(4) Methanol has a higher octane number and can be used as an additive and alternative fuel to increase the octane number of gasoline. The cetane number of methanol is much less than that of diesel, while the natural temperature is higher than that of diesel, making its compression ignition difficult. Therefore, to use methanol in

compression ignition engines, the spontaneous ignition performance of methanol needs to be improved or ignited by spark plugs, electric plugs, and by spraying in diesel fuel [21].

(5) Methanol is an oxygenated fuel with an oxygen content of up to 50%, and the self-oxygenation effect of the fuel facilitates fuller fuel combustion, high combustion efficiency, and no carbon soot generation, as well as reduced HC and CO emissions [22].

Combustion Characteristics of Methanol Internal Combustion Engines

Application of Methanol in Ignition Internal Combustion Engines

The application of methanol in ignition internal combustion engines can be divided into methanol-gasoline blended combustion, pure methanol combustion, and indirect utilization of methanol. By indirect utilization, it means that methanol is not directly allowed to be burned as a fuel in the engine, but the combustible gases (such as H_2 and CO), which are generated through the reforming cracking reaction of methanol, are fed into the cylinder for combustion [23].

Methanol Gasoline Blending and Combustion

Ling *et al.* [24] from Zhejiang University investigated the emission characteristics of methanol gasoline in an MR479q engine. Bench tests showed that adding methanol to gasoline reduced conventional emissions (such as NO_x, CO, and unburned HC), but unconventional emissions (such as formaldehyde and unburned methanol) increased significantly. When the proportion of methanol in the fuel was 70%, NO_x was reduced by 29%~54%, CO by 66%~71% and unburned HC by 71%~80% compared with gasoline engines. In terms of emission generation mechanism, the 3D simulation results show that HC, aromatic hydrocarbons and unburned methanol are mainly generated by factors such as in-cylinder gap effect and carbon accumulation, while CO and formaldehyde are mainly generated by complex chemical reaction processes. With the increase of compression ratio, CO emission decreases and NO_x emission increases.

Wang *et al.* [25] from the State Key Laboratory of Internal Combustion Engine, Tianjin University, investigated the emission characteristics of methanol engine based on an electronically controlled M85 methanol engine. The conventional and non-conventional emissions were investigated by exhaust gas analyzer and gas chromatograph, respectively. The test results showed that M85 methanol fuel can significantly reduce the conventional emissions, while the non-conventional emissions contain almost no methanol but high formaldehyde content, which is due to the fact that the three-way catalytic converter does not easily convert formaldehyde and the higher the load, the lower the purification efficiency, while the purification efficiency for methanol is almost 100%.

Wu *et al.* [26] conducted a bench test study on the engine performance of M10, M15, M50 methanol gasoline and 93# gasoline and found that compared to 93# gasoline, the power change of burning M10, M15 and M50 increased by -2%~6.25%, -2%~9.38% and 2%~12.5%, respectively, which shows that in terms of power performance, methanol gasoline fuel has little change compared to 93 # gasoline. As the methanol ratio increases, the power improvement changes, but in terms of overall operating conditions, the power improvement is not significant. Compared to 93# gasoline fuel consumption rate, M10, M15, and M50 converted to equivalent fuel consumption rate increased by 1.52%, 0.37%, and 15%, respectively. This shows that the change in fuel economy of methanol gasoline is not very obvious. The changes in HC emissions for all four fuels decreased with increasing speed. Among the three types of methanol gasoline, HC emissions decreased gradually with the increase of methanol proportion, and the highest decrease was 80%. CO emissions were significantly reduced compared with 93# gasoline, and CO emissions also decreased gradually with the increase of methanol content, and the highest decrease was 77.78%. With the increase of methanol blending ratio, the NO_X emission becomes lower and lower, with the highest reduction of 69.23%.

From the above studies, it can be concluded that methanol and gasoline have similar physicochemical properties, and methanol gasoline with low methanol ratio can be used directly in gasoline engines, while methanol gasoline with high ratio can also be used in ignition engines with simple adjustments. The improvement in economy and power over conventional fuels is small, but the emission characteristics are greatly improved, while the inherent characteristics of methanol fuels can cause cold start difficulties and unconventional pollutant emissions.

Pure Methanol Combustion

Zhu *et al.* [27] used a model of turbocharged inline 4-cylinder gasoline engine as a prototype to study the effect of methanol combustion on engine performance and emissions. Compared to gasoline combustion, the engine showed a significant improvement in power after switching to methanol, with a maximum increase of 5.22%. From the test results, the equivalent fuel consumption rate can be reduced by 10.53~ 18.52 % when switching to methanol burning, compared to the original engine burning gasoline at low to medium speed. At low and medium loads, CO emissions do not change much. But when at high loads, burning methanol can significantly reduce CO emission. CO is reduced by 29.6% at the highest load when compared to the original engine when burning methanol. At the average effective pressure of 0.4 MPa, 0.8 MPa and maximum load, HC emissions were 90.5%, 84.2% and 37.4% lower with methanol than with gasoline, respectively. Since the latent heat of vaporization of methanol is much higher than that of gasoline, this greatly reduces the mixture temperature and thus the maximum combustion temperature. Also, because methanol burns faster than gasoline, the high temperature reaction time is shortened, and the combined effect of these two conditions results in lower NO_X emissions. The test results showed that the NO_X in the exhaust gas was reduced by 95.6%, 16.4% and 14.8% when methanol was burned compared with gasoline at the average effective pressure of 0.2 MPa, 1.2 MPa and maximum load, respectively.

Wang *et al.* [28] from Jiangsu University conducted an experimental study on a four-cylinder EFI gasoline engine with a displacement of 2.0 L using pure methanol as fuel. The results showed that the maximum torque of the methanol engine was lower than that of the gasoline engine when the speed was below 2500 r/min, and higher than that of the original engine when the speed exceeded 2500 r/min. The equivalent fuel consumption was reduced by up to about 10% compared with the original engine. If the compression ratio increased from 10 to 11.5, the maximum torque of the engine increased by 3.4%~6.3%, and the equivalent fuel consumption of the methanol engine decreased by 2%~5%. For the problem of cold starting of the methanol engine, three additives, gasoline, isopentane and petroleum ether were added to the methanol fuel. When the ambient temperature was -20℃, the engine could be started smoothly within 4 s with these three additives.

From the above research analysis, it is concluded that burning pure methanol fuel is easier to achieve with less modification to the traditional internal combustion engine, and it can significantly improve the power of the engine in terms of combustion characteristics, improve the fuel economy of the engine under low load, and significantly improve the emission characteristics of the engine under high load.

Indirect Utilization of Methanol

Yao *et al.* [29] evaluated the impact of methanol cracked gas application technology on an ignition engine by studying the application of methanol cracked gas in a 477F engine. When methanol cracked gas was burned, the engine dynamics decreased, although it still remained above 95% of its original engine. The power performance of the methanol cracker engine with a palladium-based catalyst was better than that of the methanol cracker gas engine with a copper-based catalyst. Compared with the gasoline fuel consumption rate, the methanol-equivalent fuel consumption rate produced with the copper-based catalyst decreased by 22% to 26%. The methanol cracking gas-equivalent fuel consumption rate produced with the palladium-based catalyst decreased by 24% to 31%. Overall, the economic advantage of burning methanol cracked gas over gasoline is greater.

The HC emissions from the combustion of methanol cracked gas produced with copper-based and palladium-based catalysts, respectively, were relatively similar and consistent for the engine application, but the emissions were about 90% lower compared to gasoline combustion. The CO emissions from the combustion of methanol cracked gas with copper-based and palladium-based catalysts, respectively, are very similar, but the CO emissions from methanol cracked gas engines are reduced by about 90% compared to gasoline. Similarly, the NO_X emission patterns from methanol cracked gas combustion with the two different catalyst types are very similar and the NO_X emissions are relatively similar, but with significant reductions of up to 80% compared to virgin gasoline. From this study, it is concluded that methanol cracked gas as an engine fuel can effectively improve engine fuel economy and reduce HC, CO and NO_X emissions.

Application of Methanol in Compression-Ignition Internal Combustion Engines

The application of methanol in compression-ignition engines is more difficult than in ignition engines because of the large difference between the properties of methanol and diesel fuel. However, the diesel engine has the advantages of high thermal efficiency and high power compared to the ignition engine, so the research on methanol as its alternative fuel is also more valuable. Since it is difficult to achieve direct compression ignition of methanol, the application of methanol in compression-ignition internal combustion engines is concentrated on diesel ignition, diesel-methanol blended combustion and electric heating plug combustion methods.

Diesel Ignition

Fang et al. [30] from Jilin University conducted an experimental study on the performance and emissions of direct injection compression-ignition engines with dual injection system when burning diesel methanol, and found that the methanol engine showed a maximum decrease in smoke of up to 66% and a decrease in NO_x emissions of about 60%-70% compared to the original diesel engine, but CO and HC emissions increased more.

Shi *et al.* [31] conducted methanol injection tests in diesel engines in the intake tract. At low load conditions, injection of methanol reduced the dynamics by a maximum of 5%, which was due to the decrease in cylinder temperature caused by its high latent heat of vaporization. As the load increases, the engine dynamics increases when methanol is injected into the intake tract, and the maximum increase is 2.9%. However, as the amount of methanol injected increases, *i.e.*, as the percentage of total fuel increases, the power tends to increase and then decrease.

Zhang *et al.* [32] converted a supercharged intercooled engine into a diesel pilot-fired methanol dual-fuel engine by adding a methanol supply system for a bench test study. With the increase of methanol blending ratio, the HC emission of the dual-fuel engine also increased significantly, with a maximum increase of 2000%. At a certain blending ratio, HC emissions decreased as the load increased. The CO emissions of the dual-fuel engine increased significantly. The CO emissions of the dual-fuel engine increased continuously with the increase of methanol blending ratio. At the same blending ratio, the CO emission of dual-fuel engine tends to decrease with the increase of load. With the increase of methanol blending ratio, the NO_X emission of dual-fuel engine combustion decreases. For a certain blending ratio, the higher the load ratio, the more NO_X emissions. With the increasing of methanol blending ratio, the dual-fuel carbon soot emission decreases.

From the above study, the analysis concluded that the diesel priming method can reduce the smoke but the concentration of some pollutant emissions is high, and the existing diesel engine on the transformation is difficult and costly, it is difficult to implement the promotion.

Diesel-Methanol Blending and Combustion

Rao *et al.* [33] burned microemulsified methanol diesel in a D1110 diesel engine and found no significant difference in power and fuel consumption rate for burning pure diesel without making parameter adjustments to the engine, and NO_x, CO and carbon soot emissions were significantly reduced.

Soni *et al.* [34-35] investigated the effects of methanol blending ratio, swirl ratio, exhaust gas recirculation method and water blending method on emissions by numerical simulations and found that when the percentage of methanol in diesel fuel was increased from 10% to 30%. NO, CO and HC emissions were significantly reduced by 65%, 68% and 56%, respectively, and also indicating that blending the right amount of water in the fuel was beneficial to reduce NO, carbon soot, CO and HC emissions.

Duan *et al.* [36] showed that burning M15 increased the output power by 1.82%~7.14% compared to burning 0# diesel, but burning M30 decreased the power by burning M15 and M30, respectively. Compared to burning 0# diesel, burning M15 resulted in a 3.85% to 9.36% reduction in equivalent fuel consumption rate, and burning M30 resulted in a 5.14% to 15.26% reduction in equivalent fuel consumption rate. This shows that burning methanol blended fuel can significantly improve the economy. Compared with burning 0# diesel, when burning M15 and M30, CO emissions are reduced by 44.74~50 % and 50~68.97 %, HC emissions are reduced by 40.48~48.89 % and 48.89~70.59 %, respectively; NO_X emissions are reduced by 10.71%~33.33% and 25~35.71 %, respectively; and particulate matter emissions with smokiness were reduced by 57.14% and 64.29%, respectively.

From the above research analysis, it is concluded that methanol and diesel blending forms are methanol diesel and emulsified diesel, and both blended fuels are made of diesel, methanol, and additives in a certain ratio through a strict process of blending. Compression-ignition internal combustion engines using diesel-methanol blending combustion method can significantly improve the engine economy and can significantly improve the emission characteristics of internal combustion engines, but if we want to obtain the best power, there is an optimal methanol blending ratio.

Electric Heating Plug to Help Ignite

Electric thermal plugs can effectively improve the cold startability of the engine. Li *et al.* [37] investigated the reasons for successful diesel fuel ignition when the electric thermal plugs assisted combustion through an experimental study of a single-cylinder diesel engine with a compression ratio of 15.5 and a static combustion bomb, and concluded that the electric thermal plugs ignite the diesel fuel by increasing the local temperature to above 413°C.

Yang *et al.* [38] investigated the combustion characteristics of pure methanol combustion by direct injection compression ignition on a two-cylinder diesel engine. According to the characteristics of high latent heat of vaporization and high auto-ignition temperature of methanol fuel, measures such as increasing compression ratio and intake heating were adopted to successfully obtain stable operation of pure methanol in direct injection compression-ignition mode, and it can effectively reduce NO_x emission of diesel engine with fuel economy comparable to that of the original engine.

Wang *et al.* [39] studied a diesel engine burning pure methanol fuel by adding electric heating plugs, increasing the compression ratio and injection pump diameter to a 1115 single-cylinder diesel engine. They found that the power and economy of the methanol engine were better than the original diesel engine after the test. The NO_x emissions were reduced by 45% on average, and the HC and CO emissions were reduced by 70% on average at high loads, but higher than the original engine at low and medium loads.

From the above research and analysis, it is concluded that the electric heating plug combustion method can effectively improve the cold starting performance of internal combustion engines and effectively reduce the emission of NO_x, HC, CO and other pollutants at high load. But at low and medium loads, its emission performance is worse than that of the original engine.

Summary and Outlook

This paper reviews many technical means of methanol fuel combustion for internal combustion engines, analyzes its performance and emission characteristics, points out the difficulties and development prospects in the application process, and provides ideas and methods for the research field of methanol as an alternative fuel for internal combustion engines, taking into account the current situation of domestic and foreign research. The results show that the power, fuel economy and emission characteristics of internal combustion engines can be improved after using methanol.

For ignition internal combustion engines, the power of methanol can be maintained at more than 95% of the original engine, and the engine power can be improved under certain operating conditions. In terms of economy, when methanol blending technology is used, the improvement of economy is more obvious as the proportion of methanol increases, and the economy decreases when the proportion is smaller; when methanol cracking technology is used, the equivalent fuel consumption rate is reduced the most and the economy is the best. Especially from the emission performance, the emission of CO, HC and CO_2 can be significantly reduced.

For compression-ignition internal combustion engines, the use of methanol has a negative impact on diesel engine dynamics at low load conditions, while the combustion of methanol can improve dynamics as the load increases. From the economics point of view, all the technologies can improve the economy in general, except for the use of electric plug combustion, which can lead to higher equivalent fuel consumption rate under certain conditions. In terms of emission characteristics, both Soot and NOx emissions are significantly improved by burning methanol. The use of electric plug combustion and diesel ignition method will make HC and CO emissions worse, but will improve NO_x and carbon soot emissions, and the electric plug combustion method will improve NO_x and carbon soot more significantly, while the use of emulsification method can reduce HC, CO, carbon soot and NO_x emissions. Therefore, overall, the use of emulsification of methanol is the best technology for the application.

In summary, there are some problems in the current stage of methanol combustion in internal combustion engines, including poor cold start, high emission of non-conventional pollutants such as formaldehyde and methanol under low load, and poor fuel economy and power under some working conditions. In view of the various problems faced by the current methanol-fired technology for internal combustion engines, it is very beneficial to carry out the following researches to further improve the existing methanol-fired technology for internal combustion engines and promote the practical application of methanol in internal combustion engines:

(1) Mechanisms of emission generation and control methods. In addition to conventional pollutants, the study of non-conventional pollutant emissions such as formaldehyde and unburned methanol is also very important. To solve the emission problem of internal combustion engine when burning methanol, especially to make the high pollutant emission problem during cold start or low load operation.

(2) Research on the reaction mechanism of methanol, including research on the combustion mechanism of methanol mixed with other fuels and pure methanol combustion. To clarify the characteristics of methanol combustion to help solve the problems of difficult cold start and unstable ignition when internal combustion engines are burning methanol.

(3) The research of methanol additives, by adding additives to change the combustion characteristics and physical properties of methanol, reduce the difficulty of burning methanol in internal combustion engines, and improve the applicability of methanol alternative fuels.

CONFLICTS OF INTEREST

The author declares that there is no conflict of interests regarding the publication of this paper.

REFERENCES

[1] Singh, A. P., Sharma, N., Kumar, V., and Agarwal, A. K. (2021). Experimental investigations of mineral diesel/methanol-fueled reactivity controlled compression ignition engine operated at variable engine loads and premixed ratios. 22(7), 2375-2389. DOI: 10.1177/1468087420923451

[2] Singh, A. P., and Agarwal, A. K. (2021). Introduction to Novel Internal Combustion Engine Technologies for Performance Improvement and Emission Reduction. In: *Novel Internal Combustion Engine Technologies for Performance Improvement and Emission Reduction*, A. P. Singh, and A. K. Agarwal, eds., Springer Singapore, Singapore, pp: 3-6. DOI: 10.1007/978-981-16-1582-5_1

[3] Li, H., Zhang, J., Chen, J., Chen, W., Zhao, Y., Lin, M., Li, L., Zhang, X., and Dai, X. Global energy transition faces challenges in 2021 -Based on the bp Statistical Yearbook of World Energy (2022). *Natural Gas and Oil*, http://kns.cnki.net/kcms/detail/51.1183.TE.20221013.1732.002.html (accessed on 11/26/2022).

[4] Ministry of Ecology and Environment of the PRC. (2021). China Mobile Source Environmental Management Annual Report. Web: http://www.gov.cn/xinwen/2021-09/11/5636764/files/3ac6b9802f8b47fc8200403308a0d25d.pdf (accessed on 11/26/2022)

[5] Kovács, M., Papp, M., Zsély, I. G., and Turányi, T. (2021). Main sources of uncertainty in recent methanol/NOx combustion models. 53(7), 884-900. DOI: https://doi.org/10.1002/kin.21490

[6] Dierickx, J., Verbiest, J., Janvier, T., Peeters, J., Sileghem, L., and Verhelst, S. (2021). Retrofitting a high-speed marine engine to dual-fuel methanol-diesel operation: A comparison of multiple and single point methanol port injection. *Fuel Communications*, 7, 100010. DOI: https://doi.org/10.1016/j.jfueco.2021.100010.

[7] Chen, H., He, J., Chen, Z., and Geng, L. (2021). A comparative study of combustion and emission characteristics of dual-fuel engine fueled with diesel/methanol and diesel–polyoxymethylene dimethyl ether blend/methanol. *Process Safety and Environmental Protection*, 147, 714-722. DOI: https://doi.org/10.1016/j.psep.2021.01.007

[8] Kalwar, A., Singh, A. P., and Agarwal, A. K. (2020). Utilization of primary alcohols in dual-fuel injection mode in a gasoline direct injection engine. *Fuel*, 276, 118068. DOI: https://doi.org/10.1016/j.fuel.2020.118068

[9] Chen, Z., Chen, H., Wang, L., Geng, L., and Zeng, K. (2020). Parametric study on effects of excess air/fuel ratio, spark timing, and methanol injection timing on combustion characteristics and performance of natural gas/methanol dual-fuel engine at low loads. *Energy Conversion and Management*, 210, 112742. DOI: https://doi.org/10.1016/j.enconman.2020.112742

[10] Zhang, M., Hong, W., Xie, F., Liu, Y., Su, Y., Li, X., Liu, H., Fang, K., and Zhu, X. (2019). Effects of diluents on cycle-by-cycle variations in a spark ignition engine fueled with methanol. *Energy*, 182, 1132-1140. DOI: https://doi.org/10.1016/j.energy.2019.06.110

[11] Shao, Y., Sun, Q., Li, A., He, Z., Xu, Z., Qian, Y., Lu, X., Huang, Z., and Zhu, L. (2019). Effects of natural gas, ethanol, and methanol enrichment on the

performance of in-cylinder thermochemical fuel reforming (TFR) spark-ignition natural gas engine. *Applied Thermal Engineering*, 159, 113913. DOI: https://doi.org/10.1016/j.applthermaleng.2019.113913

[12] Sharma, N., Patel, C., Tiwari, N., and Agarwal, A. K. (2019). Experimental investigations of noise and vibration characteristics of gasoline-methanol blend fuelled gasoline direct injection engine and their relationship with combustion characteristics. *Applied Thermal Engineering*, 158, 113754. DOI: https://doi.org/10.1016/j.applthermaleng.2019.113754

[13] Chen, Z., Wang, L., and Zeng, K. (2019). A comparative study on the combustion and emissions of dual-fuel engine fueled with natural gas/methanol, natural gas/ethanol, and natural gas/n-butanol. *Energy Conversion and Management*, 192, 11-19. DOI: https://doi.org/10.1016/j.enconman.2019.04.011

[14] Prayogi, Y., Syaiful, and Sinaga, N. (2019). Performance and exhaust gas emission of gasoline engine fueled by gasoline, acetone and wet methanol blends. *IOP Conference Series: Materials Science and Engineering*, 535(1), 012013. DOI: 10.1088/1757-899X/535/1/012013

[15] Song Y. (2019).Experimental study on the effect of alcohol injection moment on the combustion and emission characteristics of methanol/diesel dual-fuel engine. Chang'an University, Thesis.

[16] Lian, R., Zhu, W., Xiao, C., Hu, Z., Pan, L. (2019) Research on promotion and value of DMCC heavy-duty trucks. *Automobile Applied Technology*, 2019(03), 10-12.

[17] Wu S. (2019). Prospect of military methanol vehicle application[J]. Development & Innovation of Machinery & Electrical Products, 32(01), 49-51.

[18] Hussein, M. R. A., Hassoon, M. A. S., and Al-Abbas, D. A. H. (2018). Experimental Study into Combustion Characteristics of IC Engines Operated with Blended Fuels. *IOP Conference Series: Materials Science and Engineering*, 433(1), 012053. DOI: 10.1088/1757-899X/433/1/012053

[19] Gupta, A., and Mishra, P. C. (2018). Emission and friction analysis of IC engine running in methanol blend. *Tribology in Industry*, *40*(1), 10.

[20] Yuan, Q. (2017). Effect of ignition moment on methanol engine combustion. *Technology Innovation and Application*, 2017(22), 181-182.

[21] Huang C.F., Hao C.X., Wang J.F., and Xie Q. (2017). Analysis of pollutant emissions from motor vehicles--Part II of the Annual Report on Environmental Management of Motor Vehicles in China. *Environmental Protection*, 45(13), 42-47.

[22] HAN, S. B., and PARK, J. Y. (2016). Performance and Emission Characteristics of Ethanol and Methanol Gasoline Blended Fuels in a Spark Ignition Engine. *Transactions of the Korean Hydrogen and New Energy Society*, *27*(4), 441-446. DOI: https://doi.org/10.7316/khnes.2016.27.4.441

[23] Kamil, M., and Nazzal, I. T. (2016). Performance evaluation of spark ignited engine fueled with gasoline-ethanol-methanol blends. *Journal of Energy and Power Engineering*, *10*(6), 343-351. DOI: 10.17265/1934-8975/2016.06.002

[24] Li, C. (2016). *Design and development of low emission methanol-diesel dual fuel intelligent combustion system*. Tianjin University, Thesis.

[25] Ling, X.C. (2015). *Simulation and experimental study of emission generation mechanism of engine burning methanol-gasoline fuel mixture*. Zhejiang University, Thesis.

[26] Wu, Z., Wang, Y., and Hou, G. (2014). Experimental study on the performance of different proportation methanol gasoline mixed burning. *Journal of Changchun Institute of Technology(Natural Sciences Edition)*, 15(02), 69-72.

[27] Zhu, J. (2017). *Comparative study on the performance of engine fueled gasoline and methanol*. Huazhong University of Science and Technology, Thesis.

[28] Wang, Y. (2016). *Experimental study on the combustion of M100 methanol in electronically controlled gasoline engine*. Jiangsu University,2016, Thesis.

[29] Yao, C., Li, X.C., Tang, C., Zang, R., and Wu, Y. (2013). Combustion Characteristic of Methanol Dissociated Gas Engine Through Cu/Pd-Based Catalysts. *Transactions of CSICE*, 30(6), 486-491.

[30] Fang, X., Liu, X., Jin, W., and Yan, S. (2003). A Study on a DI Compression Ignition Engine with Diesel-Methanol Injection by Dual Injection Systems. *Transactions of CSICE*, 21(6), 411-414. DOI:10.16236/j.cnki.nrjxb.2003.06.005.

[31] Shi, W., Wang, T., Liao, W., Wang, D., Wang, H., and Deng, Y. (2012). Effect of methanol injection at intake port on turbocharged and intercooled diesel engines. *Vehicle Engine*, 2012(06), 46-50.

[32] Li, G., Zhang, C., and Li, Y. (2017) Combustion cycle variation of electronically controlled common rail diesel engine fueled with methanol-diesel dual fuel. *Journal of Chang'an University (Natural Science Edition)*, 37(02), 107-114. DOI:10.19721/j.cnki.1671-8879.2017.02.013.

[33] Rao, H., Wang, T., Wang, K., and Zhu, J. (2008). Experimental Research on Methanol-diesel Micro-emulsified Fuel in DI Engine. *Vehicle Engine*, 2008(05), 89-92.

[34] Soni, D. K., and Gupta, R. (2016). Optimization of methanol powered diesel engine: A CFD approach. *Applied Thermal Engineering*, 106, 390-398. DOI: https://doi.org/10.1016/j.applthermaleng.2016.06.026

[35] Soni, D. K., and Gupta, R. (2016). Numerical investigation of emission reduction techniques applied on methanol blended diesel engine. *Alexandria Engineering Journal*, 55(2), 1867-1879. DOI: https://doi.org/10.1016/j.aej.2016.02.019

[36] Duan, M.W., Yang, W.C., Tan, S.B., Ma, K., Qiao, B.C., and Luo, Y. (2015). Study on the application of microemulsion methanol diesel in diesel engines. *Small Internal Combustion Engine and Vehicle Technology*, 44(05), 85-88+93.

[37] Li, J., Gong, C., Liu, B., Su, Y., Dou, H., and Liu, X. (2009). Combustion and Hydrocarbon (HC) Emissions from a Spark-Ignition Engine Fueled with Gasoline and Methanol during Cold Start. *Energy & Fuels*, 23(10), 4937-4942. DOI: 10.1021/ef900502e

[38] Yang, M.H., Wei, X.Y., and Hu, G.D. (1990). Experimental study of compression-ignition pure methanol engine. *Journal of Dalian University of Technology*, 1990(06), 697-704.

[39] Wang, J., Zhu, J., Wang, Y., Liu, L., and Gao, C.H. (2014). Performance and emission study of high compression ratio methanol engine. *Agricultural Mechanization Research*, 36(09), 229-232. DOI:10.13427/j.cnki.njyi.2014.09.052

Trends in Renewable Energy
OPEN ACCESS ISSN:2376-2144
Peer-Reviewed Article futureenergysp.com/index.php/tre

Artificial Intelligence, Machine Learning and Neural Networks for Tomography in Smart Grid – Performance Comparison between Topology Identification Methodology and Neural Network Identification Methodology for the Distribution Line and Branch Line Length Approximation of Overhead Low-Voltage Broadband over Power Lines Network Topologies

Athanasios G. Lazaropoulos[1,2,*] and Helen C. Leligou[2]

1: School of Electrical and Computer Engineering / National Technical University of Athens /
9 Iroon Polytechniou Street / Zografou, GR 15780
2: Department of Industrial Design and Production Engineering / School of Engineering / University of West Attica / 250 Thivon & P. Ralli / Athens, GR 12244

Received December 8, 2022; Accepted January 5, 2023; Published January 9, 2023

Until now, the neural network identification methodology for the branch number identification (NNIM-BNI) has identified the number of branches for a given overhead low-voltage broadband over powerlines (OV LV BPL) topology channel attenuation behavior [1]. In this extension paper, NNIM-BNI is extended so that the lengths of the distribution lines and branch lines for a given OV LV BPL topology channel attenuation behavior can be approximated; say, the tomography of the OV LV BPL topology. NNIM exploits the Deterministic Hybrid Model (DHM) and the OV LV BPL topology database of Topology Identification Methodology (TIM). By following the same methodology of the original paper, the results of the neural network identification methodology for the distribution line and branch line length approximation (NNIM-LLA) are compared against the ones of the newly proposed TIM-based methodology, denoted as TIM-LLA.

Keywords: Smart Grid; Broadband over Power Lines (BPL) networks; Power Line Communications (PLC); Distribution and Transmission Power Grids; Neural Networks; Machine Learning; IT; Modeling; Artificial Intelligence

1. Introduction

The evolution of the today's traditional power grid to a modern power grid that is upgraded with an intelligent IP-based communications network may support a myriad of broadband applications [1-5]. Among the communications solutions that may allow this smart grid transformation, Broadband over Power Lines (BPL) technology exploits the available wired power grid infrastructure while permitting the coexistence with other communications solutions through their BPL wireline/wireless interfaces [5-8]. However, the wired power grid infrastructure remains a hostile propagation and transmission

*Corresponding author: AGLazaropoulos@gmail.com

Tr Ren Energy, 2023, Vol.9, No.1, 34-77. doi: 10.17737/tre.2023.9.1.00149

medium for BPL signals that suffer in these communications channels from high and frequency-selective channel attenuation and noise [9-15].

Until now, a plethora of channel models has been proposed or properly adjusted from other communications technologies in the literature for characterizing BPL channels; say, deterministic, statistical, bottom-up, top-down BPL channel models or appropriate syntheses of the aforementioned ones [9], [11], [16-28]. Similarly to [1], the deterministic hybrid model (DHM) is here applied in the overhead low voltage (OV LV) BPL networks for modeling BPL signal propagation and transmission across them and thus providing critical broadband performance metrics, which further act as the big data feed for the broadband applications. In this extension paper, Topology Identification Methodology (TIM), which has been proposed in [29, 30] and is one of the broadband applications supported by BPL technology in the smart grid, stores in its TIM BPL topology database, analyzes and reports with the DHM the channel attenuation measurements of various BPL topologies. In [29, 30], TIM approximates the exact topological characteristics (*i.e.*, number of branches, length of branches, length of main lines and branch terminations) of an examined BPL topology by comparing its channel attenuation measurements with the theoretical channel attenuation results stored in the TIM BPL topology database. In [1], TIM has been extended to TIM-based Branch Number Identification methodology (TIM-BNI) so that the number of branches of an OV LV BPL topology whose theoretical channel attenuation results are known can be approximated when this examined OV LV BPL topology is not among the OV LV BPL topologies of the TIM BPL topology database. In this extension paper, TIM and TIM-BNI are further extended to the new TIM-based methodology for approximating the distribution line and branch line lengths (TIM-LLA) of an examined OV LV BPL topology when the examined topology is not among the OV LV BPL ones of the TIM BPL topology database.

In [1], the set of the supported broadband applications by the smart grid has been enriched by experimenting with artificial intelligence (AI) and machine learning (ML) capabilities. By exploiting the available big data of the TIM BPL topology database for the OV LV BPL topologies and the neural network architectures / training, the neural network identification methodology for the branch number identification (NNIM-BNI) of OV LV BPL topologies has been proposed in [1]. Alternatively to TIM-LLA, NNIM-BNI is upgraded in this extension paper so as to approximate the distribution line and branch line lengths (NNIM-LLA) of an examined OV LV BPL topology when this topology is not included in the TIM BPL topology database. By following the same methodology of [1] and exploiting its findings and conclusions for better approximation performances of the family products of TIM and NNIM, new default operation settings are applied in this extension paper. Finally, the performance results of NNIM-LLA are going to be compared against the ones of TIM-LLA for different operation scenarios and OV LV BPL topologies.

The rest of this paper is organized as follows: Section 2 briefly presents DHM, TIM-BNI and NNIM-BNI. Certain aspects that have been highlighted in the original paper and concern the operation of TIM-BNI and NNIM-BNI are demonstrated in this Section. Section 3 focuses on the proposal of TIM-LLA and NNIM-LLA as well as the corresponding performance metrics. Section 4 introduces the new default operation settings while the performance metric results for TIM-LLA and NNIM-LLA are presented for the indicative OV LV BPL topologies of the original paper. Section 5 concludes this extension paper.

2. DHM, TIM-BNI and NNIM-BNI

In this Section, a brief synopsis of the basic elements that have been presented in [1] and are going to influence the operation and performance of TIM-LLA and NNIM-LLA is given. More specifically, DHM is presented by focusing on its output of channel attenuation that is appropriately included into TIM OV LV BPL topology database. Then, TIM-BNI and NNIM-BNI, which have been proposed in [1], are briefly discussed as well as the corresponding useful conclusions of [1] that are going to be used in this extension paper and may further affect the operation and performance of TIM-LLA and NNIM-LLA.

2.1 DHM and TIM OV LV BPL Topology Database

In accordance with [1], DHM is a synthetic BPL channel model where a bottom-up, a top-down, a coupling scheme and other performance metric computation modules may be concatenated [9-12], [16], [31], [32]. With reference to eq. (2) of [1], the coupling scheme channel transfer function, which is the system output of the first three DHM modules, relates the output BPL signals with the input ones through:

$$H^{\mathrm{OVLV},C}\{\cdot\} = \left[\mathbf{C}^{\mathrm{out}}\right]^{\mathrm{OVLV},C} \cdot \mathbf{H}^{\mathrm{OVLV}}\{\cdot\} \cdot \left[\mathbf{C}^{\mathrm{in}}\right]^{\mathrm{OVLV},C} \tag{1}$$

where $[\cdot]^{\mathrm{c}}$ denotes the applied coupling scheme, $\mathbf{C}^{\mathrm{in}}$ and $\mathbf{C}^{\mathrm{out}}$ are the input and output coupling matrices and $\mathbf{H}^{\mathrm{OVLV}}\{\cdot\}$ is the channel transfer function matrix. From eq. (1), it is clear that the channel attenuation is a frequency dependent DHM output that depends on the applied coupling scheme, the OV LV multiconductor transmission line (MTL) configuration and the examined OV LV BPL topology [33, 34]. Therefore, a correspondence between the topological characteristics of an OV LV BPL topology and its channel attenuation is established from eq. (1) when the applied coupling scheme and the OV LV MTL configuration are given. When a great number of OV LV BPL topologies are assumed, respective topological characteristics and channel attenuation data can be available from eq. (1) thus acting as the big data feed of the TIM OV LV BPL topology database.

TIM OV LV BPL topology database, which acts as the big data pool for both TIM- and NNIM-based methodologies of the original paper and this extension one, is in fact the core part of TIM [29]. In this extension paper and with reference to Figure 1b of [1], the following data are maintained for each OV LV BPL topology of the TIM OV LV BPL topology database of this extension paper, namely: (i) its ID number p in the TIM OV LV BPL topology database when P is the number of all OV LV BPL topologies in the TIM OV LV BPL topology database; (ii) the actual number of branches N; (iii) the actual lengths of the distribution lines $\mathbf{L} = [L_1 \quad L_2 \quad \cdots \quad L_{N+1}]$; (iv) the actual lengths of the branch lines $\mathbf{L_b} = [L_{\mathrm{b}1} \quad L_{\mathrm{b}2} \quad \cdots \quad L_{\mathrm{b}N}]$; and (v) the coupling scheme channel transfer function values with respect to the frequency. According to [1], [29], the size of the TIM OV LV BPL topology database depends on the TIM OV LV BPL topology database specifications, which are part of the default operation settings of this extension paper, havinh to do with the topological characteristics of the OV LV BPL topologies stored in the database such as the maximum number of branches $N_{\max}$, the length spacing L_{s} for both branch distance and branch length, the maximum branch length $L_{\mathrm{b,max}}$ and the operation frequency range. Here, it should be reminded that TIM is a BPL broadband application that aims at identifying an OV LV BPL topology with respect to its topological characteristics when its theoretical or actual coupling scheme transfer function behavior is known even if measurement differences may occur [29], [35], [36].

2.2 TIM-BNI and NNIM-BNI

TIM-BNI has been proposed and assessed in [1]. TIM-BNI has aimed at approximating the branch number of an examined OV LV BPL topology by comparing its coupling scheme channel transfer function values of eq. (1) against the respective ones of all the OV LV BPL topologies of the TIM OV LV BPL topology database. Note that the indicative OV LV BPL topologies, which have been reported in Table 1 of [1], have not been included in the TIM OV LV BPL topology database except for the OV LV BPL Line-of-Sight (LOS) topology case. In order to approximate the branch number, TIM-BNI has identified the R OV LV BPL topologies of the TIM OV LV BPL topology database that have better approximated the channel attenuation behavior of the examined indicative OV LV BPL topology. To identify the R closest approximations, TIM-BNI has applied the performance metric of the root-mean-square deviation (RMSD) of the amplitude of the coupling scheme channel transfer function in dB, as shown in eqs (3) and (4) of [1]. The average value of the branch numbers of the R OV LV BPL topologies of the TIM OV LV BPL topology database that have presented the R lowest RMSDs among the P computed ones has defined the TIM-BNI approximation of the branch number of the examined indicative OV LV BPL topology $N_{\mathrm{TIM-BNI}}$ [1]. Factors that affect the accuracy performance of the TIM-BNI approximations are the required accuracy degree of the TIM OV LV BPL topology database, the number R of the OV LV BPL topologies of the TIM OV LV BPL topology database with the lowest RMSDs and the representativeness of the TIM OV LV BPL topology database.

Similarly to TIM-BNI, NNIM-BNI has been proposed and assessed in [1] while its operation philosophy lies in the areas of AI, ML and neural networks [37-40]. The operation of NNIM-BNI has been based on: (i) the TIM OV LV BPL topology database; and (ii) the MATLAB neural network program of [38], [41] that implements the fully connected neural network architecture of Figure 2 of [1] through the training, validation and testing phases. Since NNIM-BNI may train neural networks of variable numbers of hidden layers, NNIM-BNI has exploited the performance metric of RMSD of the amplitude of the coupling scheme channel transfer function in dB, as shown in eq (5) of [1]. In fact, NNIM-BNI has approximated the branch numbers $N_{\mathrm{NNIM-BNI}}$ of the examined indicative OV LV BPL topology per hl hidden layer but also reports RMSD of each approximation. In a similar way, factors that affect the accuracy performance of the NNIM-BNI approximations are the required accuracy degree of the TIM OV LV BPL topology database, the number HL of the hidden layers assumed, the participation percentage of the three phases and the representativeness of the TIM OV LV BPL topology database.

3. TIM-LLA and NNIM-LLA

In this Section, TIM-LLA and NNIM-LLA are proposed. Prior to this proposal, additional specifications that affect the definition of the TIM OV LV BPL topology database for its operation with TIM-LLA and NNIM-LLA are required to be given. After the proposal, similarly to [1], suitable performance metrics, which allow the approximation assessment of the distribution line and branch line lengths of the examined indicative OV LV BPL topologies in each methodology are reported. Note that the number of branches of the examined indicative OV LV BPL topologies is assumed to be known prior to apply both methodologies.

3.1 Additional Specifications for TIM OV LV BPL Topology Database

With reference to Sec.2.2, the number of OV LV BPL topologies vary in the TIM OV LV BPL topology depending on the assumed TIM OV LV BPL topology database specifications [1], [29], [30]. By considering the assumption of the known number of branches of the examined indicative OV LV BPL topologies and the conclusion of [1] regarding the need for database representativeness, only the OV LV BPL topologies of the TIM OV LV BPL topology database with the same number of branches with the examined indicative OV LV BPL topology are going to be examined during the operation of TIM-LLA and NNIM-LLA. In addition, so as not to disrupt the approximations due to the symmetry of BPL topologies (*e.g.*, the OV LV BPL topology with lengths of its distribution lines $\mathbf{L}=[100m \quad 900m]$ and of its branch lines $\mathbf{L_b}=[20m]$ is symmetrical to the OV LV BPL topology with respective lengths $\mathbf{L}=[900m \quad 100m]$ and $\mathbf{L_b}=[20m]$) [42], [43], only one of the symmetrical OV LV BPL topologies is stored in the OV LV BPL topology database.

3.2 TIM-LLA

Similarly to [1], each indicative OV LV BPL topology that is going to be examined in this extension paper is not included in the TIM OV LV BPL topology database by definition. Hence, TIM-LLA is going to approximate the distribution and branch line lengths of the examined indicative OV LV BPL topology by comparing its coupling scheme channel transfer function values against the respective ones of all the OV LV BPL topologies of the TIM OV LV BPL topology database with the same number of branches. The performance metric of RMSD of the amplitude of coupling scheme transfer functions in dB that is expressed by eqs. (3) and (4) of [1] is also here applied in order to identify the OV LV BPL topologies of the TIM OV LV BPL topology database that achieve the best approximations of the channel attenuation behavior of the examined indicative OV LV BPL topology. The average value for each of the lengths of the *R* OV LV BPL topologies of the TIM OV LV BPL topology database that present the *R* lowest RMSDs among the *P* computed ones defines the TIM-LLA approximation of the respective lengths of the examined indicative OV LV BPL topology (i.e., the TIM-LLA approximation lengths of the distribution and branch lines are $\mathbf{L}_{\mathrm{TIM-LLA}}=[L_{1,\mathrm{TIM-LLA}} \quad L_{2,\mathrm{TIM-LLA}} \quad \cdots \quad L_{N+1,\mathrm{TIM-LLA}}]$ and $\mathbf{L}_{\mathrm{b,TIM-LLA}}=[L_{\mathrm{b1,TIM-LLA}} \quad L_{\mathrm{b2,TIM-LLA}} \quad \cdots \quad L_{\mathrm{b}N,\mathrm{TIM-LLA}}]$, respectively). Similarly to TIM-BNI, it is clear that TIM-LLA performance towards the distribution and branch line length identification of OV LV BPL topologies, that is numerically assessed in Section 4, is affected by the required accuracy degree of the TIM OV LV BPL topology database and the number *R* of the lowest RMSDs.

3.3 NNIM-LLA

With reference to Figure 2 of [1], NNIM-LLA is going to adopt a similar neural network architecture with NNIM-BNI; say, a fully connected neural network with *HL* hidden layers of neurons where its input is *P* column vectors; the *p, p*=1,…,*P* column vector consists of the differences between the amplitude of the coupling scheme channel transfer functions of the arbitrary *p* OV LV BPL topology of the TIM OV LV BPL topology database in dB and the amplitude of the coupling scheme channel transfer functions of LOS case in dB at each frequency of the operating frequency range. After the input layer, *HL* hidden layers occur; each *hl* of the *HL* hidden layers receives as input a column vector from the previous one while it gives as output a column vector for the following one where the activation function, the array of weights and array of biases of the *hl* hidden layer are taken into consideration. The output of the fully connected neural network that coincides with the output of the *HL* hidden layer defines the NNIM-LLA approximation of the respective lengths of the examined indicative OV LV BPL topology (i.e., the NNIM-LLA approximation lengths of the distribution and branch lines are $\mathbf{L}_{\mathrm{NNIM-LLA}} = [L_{1,\mathrm{NNIM-LLA}} \quad L_{2,\mathrm{NNIM-LLA}} \quad \cdots \quad L_{N+1,\mathrm{NNIM-LLA}}]$ and $\mathbf{L}_{\mathrm{b,NNIM-LLA}} = [L_{\mathrm{b1,NNIM-LLA}} \quad L_{\mathrm{b2,NNIM-LLA}} \quad \cdots \quad L_{\mathrm{b}N,\mathrm{NNIM-LLA}}]$, respectively). Similarly to [1], NNIM-LLA exploits the MATLAB neural network training program of [38], [41] while the big data handling of the TIM OV LV BPL topology database is divided into three phases; say, training, validation and testing phase. As in the case of TIM-LLA, NNIM-LLA applies the RMSD performance metric of the examined indicative OV LV BPL topologies for different numbers of the hidden layers during all its three phases. Therefore, TIM-LLA may give as output its approximation for the lengths of the distribution and branch lines as well as their approximation RMSDs per hidden layer. Similarly to NNIM-BNI, it is clear that NNIM-LLA performance, which is numerically assessed in Section 4 in comparison with the TIM-LLA performance, is affected by the required accuracy degree of the TIM OV LV BPL topology database and the participation percentage of the three phases of the MATLAB neural network training program.

4. Numerical Results and Discussion

In this Section, numerical results concerning the performance of TIM-LLA and NNIM-LLA are presented as well as their evaluation. Actually, this extension paper follows the same structure regarding the demonstration of the numerical results with [1]. First, the default operation settings for the base scenario are given in Sec. 4.1 by also taking under consideration the findings and conclusions of [1]. Second, the effect of the *R* value of the OV LV BPL topologies of the TIM OV LV BPL topology database with the lowest RMSDs that is considered during the computation of the average values of the lengths of the distribution and branch lines is examined during the operation of TIM-LLA in Sec. 4.2. Third, the role of the participation percentages of the three phases of NNIM-LLA during its operation is assessed in Sec. 4.3. Finally, an overall numerical performance comparison between TIM-LLA and NNIM-LLA is attempted in Sec. 4.4.

4.1 Base Scenario and Default Operation Settings B

As the base scenario of the operation of TIM-LLA and NNIM-LLA is concerned, certain default operation settings should be assumed. Actually, the default operation settings of [1], denoted as default operation settings A in the rest of this extension paper, are here enriched so as to exploit the experience from the operation of TIM-BNI and NNIM-BNI, that act as the predecessor family products of the TIM-LLA and NNIM-LLA, respectively, and boost the accuracy for the challenging issue of OV LV BPL topology tomography. More specifically, the following default operation settings B are assumed:

- The applied OV LV MTL configuration and the typical OV LV BPL topology that are used in this extension paper are shown in Figures 1(a) and 1(b) of [1], respectively. With reference to Figure 1(b), three indicative OV LV BPL topologies, which are shown in green background color, are reported in terms of their topological characteristics in Table 1. The three indicative OV LV BPL topologies of interest (i.e., urban case A, suburban case and rural case), which have already been used for the evaluation of TIM-BNI and NNIM-BNI, are going to be further adopted in this extension paper so that the approximation performances of TIM-LLA and NNIM-LLA can also be evaluated. In accordance with [1], the branch terminations are assumed to be open-circuit while the transmitting and receiving ends are assumed to be matched [9]-[12], [16]. WtG[1] coupling scheme is applied across the indicative and TIM OV LV BPL topologies of this extension paper.
- As the preparation of the TIM OV LV BPL topology database is concerned for the evaluation of TIM-LLA and NNIM-LLA, the indicative urban case A, suburban case and rural case will be excluded from the TIM OV LV BPL topology database so that TIM-LLA and NNIM-LLA blindly perform their approximations. As already been mentioned, depending on the examined indicative OV LV BPL topology, the number of branches is known thus influencing the segmentation and the accuracy of the TIM OV LV BPL topology database in each case (i.e., only the OV LV BPL topologies with the same number of branches with the examined one are considered from the TIM OV LV BPL topology database in each approximation execution by TIM-LLA and NNIM-LLA).
- During the preparation of the TIM OV LV BPL topology database [29], [30], the length spacings for branch distance and branch length are assumed to be equal to 100m and 100m, respectively, while the branch line length may range from 0m to 300m. In accordance with [1], the distribution line length and, thus, the length between the transmitting and receiving ends of all the OV LV BPL topologies of this paper is assumed to be equal to 1000m. Despite the higher maximum branch line length of 300m in comparison with the 100m of [1], the high length spacings of 100m in comparison with the 25m of [1] imply that: (i) better execution times during the TIM OV LV BPL topology database and the simulation process occur; and (ii) the branch line lengths of rural OV LV BPL topologies (the maximum one is equal to 300m in this extension paper) can range from 0m to 300m. In accordance with [1], there is a trade-off relationship between the accuracy of the TIM OV LV BPL topology database and the length spacings. Therefore, high RMSDs due to high differences between the actual and approximated branch lengths are expected in this paper due to the combination of high branch line length spacing and maximum branch line length.

Table 1
Indicative OV LV BPL Topologies [1]

OV LV BPL Topology Name	**Number of Branches (N)**	**Length of Distribution Lines**	**Length of Branch Lines**
Urban case A (Typical urban case)	3	L_1=500m, L_2=200m, L_3=100m, L_4=200m	L_{b1}=8m, L_{b2}=13m, L_{b3}=10m
Urban case B (Aggravated urban case)	5	L_1=200m, L_2=50m, L_3=100m, L_4=200m, L_5=300m, L_6=150m	L_{b1}=12m, L_{b2}=5m, L_{b3}=28m, L_{b4}=41m, L_{b5}=17m
Suburban case	2	L_1=500m, L_2=400m, L_3=100m	L_{b1}=50m, L_{b2}=10m
Rural case	1	L_1=600m, L_2=400m	L_{b1}=300m
Line-of-Sight (LOS) case	0	L_1=1000m	-

- In accordance with Sec. 3.1, symmetrical OV LV BPL topologies are excluded from the TIM OV LV BPL topology database. This implies that TIM-LLA and NNIM-LLA are going to give as output original approximated OV LV BPL topologies that is the first of the two parts of the full answer; the second and last part of the full answer is the symmetrical approximated OV LV BPL topology to the original one. For example, if NNIM-LLA gives as output the approximation lengths of the distribution and branch lines $\mathbf{L}_{\mathrm{NNIM-LLA}}=[100\mathrm{m} \quad 500\mathrm{m} \quad 400\mathrm{m}]$ and $\mathbf{L}_{\mathrm{b,NNIM-LLA}}=[50\mathrm{m} \quad 75\mathrm{m}]$ of the original approximated OV LV BPL topology, the symmetrical approximated OV LV BPL topology has lengths of the distribution and branch lines that are equal to $\mathbf{L}_{\mathrm{NNIM-LLA}}=[400\mathrm{m} \quad 500\mathrm{m} \quad 100\mathrm{m}]$ and $\mathbf{L}_{\mathrm{b,NNIM-LLA}}=[75\mathrm{m} \quad 50\mathrm{m}]$, respectively. Similarly to the urban case A, suburban case and rural case, it should be noted that the symmetrical OV LV BPL topologies of the aforementioned three indicative OV LV BPL topologies are also excluded from the TIM OV LV BPL topology database so that TIM-LLA and NNIM-LLA blindly perform their approximations.
- Due to the improved results presented in Sec. 4.2 of [1] concerning the assumption of wide and dense frequency ranges, the frequency range and the flat-fading subchannel frequency spacing are assumed to be equal to 3-88MHz and 1MHz, respectively, in this extension paper.
- Similarly to [1], the performance metric of RMSD is going to be used by TIM-LLA; say, the RMSD of the amplitudes of coupling scheme channel transfer functions in dB of the OV LV BPL topologies from the TIM OV LV BPL topology database with respect to the ones of each of the indicative OV LV BPL topologies of Table 1 as described in eq. (3) of [1]. For the base scenario where the default operation settings B are assumed, the average value for each of the lengths of the five OV LV BPL topologies of the TIM OV LV BPL topology database (i.e., R=5) that present the five lowest RMSDs among the P computed ones defines the TIM-LLA approximation of the respective length of each of the examined indicative OV LV BPL topologies of Table 1 (i.e., the TIM-LLA approximation lengths of the distribution and branch lines are $\mathbf{L}_{\mathrm{TIM-LLA}}=[L_{1,\mathrm{TIM-LLA}} \quad L_{2,\mathrm{TIM-LLA}} \quad \cdots \quad L_{N+1,\mathrm{TIM-LLA}}]$ and $\mathbf{L}_{\mathrm{b,TIM-LLA}}=[L_{\mathrm{b1,TIM-LLA}} \quad L_{\mathrm{b2,TIM-LLA}} \quad \cdots \quad L_{\mathrm{b}N,\mathrm{TIM-LLA}}]$, respectively). The TIM-LLA

performance assessment is going to be fulfilled through the comparison between the TIM-LLA distribution and branch line lengths and the real ones while the performance metric of RMSD again assesses the overall TIM-LLA approximation for the three examined indicative OV LV BPL topologies of Table 1.

- With reference to [1], the default participation percentages of the three phases of the MATLAB neural network training program of [38], [41], say, training, validation and testing phase, during the operation of NNIM-LLA are assumed to be equal to 70%, 15% and 15%, respectively. Similarly to [1], the output of NNIM-LLA is going to be the NNIM-LLA approximation lengths of the distribution lines $\mathbf{L}_{\mathrm{NNIM-LLA}} = [L_{1,\mathrm{NNIM-LLA}} \quad L_{2,\mathrm{NNIM-LLA}} \quad \cdots \quad L_{N+1,\mathrm{NNIM-LLA}}]$ and of the branch lines $\mathbf{L}_{\mathrm{b,NNIM-LLA}} = [L_{\mathrm{b}1,\mathrm{NNIM-LLA}} \quad L_{\mathrm{b}2,\mathrm{NNIM-LLA}} \quad \cdots \quad L_{\mathrm{b}N,\mathrm{NNIM-LLA}}]$ per hidden layer when the maximum number of hidden layers HL is assumed to be equal to 5. In addition, three executions of NNIM-LLA are going to be reported in each examined case when the participation percentages of the three phases are given. The results of NNIM-LLA are going to be compared with the real ones in each case while the performance metric of RMSD is going to assess the overall NNIM-LLA approximation.

In Table 2, the length approximations of the distribution and branch lines of TIM-LLA and NNIM-LLA are reported when the aforementioned default operation settings B are assumed and the urban case A of Table 1 is examined. Apart from the original approximations that are given in black font color, the symmetrical approximations of TIM-LLA and NNIM-LLA for the urban case A are also given in blue font color. In addition, the real lengths of the distribution and branch lines of the urban case A are presented for comparison reasons while the RMSDs of TIM-LLA and NNIM-LLA approximations for the urban case are also computed. Similarly to [1], the three executions of NNIM-LLA are reported for the urban case A per hidden layer. Tables 3 and 4 are same with Table 2 but for the suburban and rural case of Table 1, respectively. Note that RMSD is computed in Tables 2-4 when 4 distribution line segments and 3 branches are assumed for all the three examined indicative OV LV BPL topologies for comparison reasons. RMSD is marked with X and is not computed when at least one of the approximated distribution and branch line lengths is below zero during the NNIM-LLA approximations (i.e., unacceptable approximations for the rest of this paper).

To permit an easier and graphical comparison of TIM-LLA and NNIM-LLA among the three indicative OV LV BPL topologies of Table 1, the RMSD results of Table 2 are presented in Figure 1. More specifically, with reference to the RMSD of the original and symmetrical approximations, TIM-LLA and NNIM-LLA are plotted with respect to the number of hidden layers for the urban case A. The best approximations between the original and symmetrical approximations are shown for TIM-LLA and NNIM-LLA given the number of the hidden layers. For NNIM-LLA, the RMSD values concerning all the 3 executions of NNIM-LLA are separately demonstrated. In Figures 2 and 3, similar curves are given with Figure 1 but for the suburban and rural case with reference to Table 3 and 4, respectively.

Table 2
Distribution and Branch Line Length Approximations of TIM-LLA and NNIM-LLA for the Urban Case A and Default Operation Settings B (the symmetrical approximations are reported in blue font color)

Indicative OV LV BPL Topologies of Table 1		**Urban case A (Typical urban case)**	**RMSD**	**Notes**
Distribution Line Length L =$[L_1 \quad L_2 \quad L_3 \quad L_4]$ **Branch Line Length** $\mathbf{L}_\mathrm{b}$ =$[L_{\mathrm{b}1} \quad L_{\mathrm{b}2} \quad L_{\mathrm{b}3}]$		[500m 200m 100m 200m] [8m 13m 10m]	-	-
TIM-LLA **Approximated Distribution Line Length** $\mathbf{L}_{\mathrm{TIM-LLA}} = [L_{1,\mathrm{TIM-LLA}} \quad L_{2,\mathrm{TIM-LLA}} \quad L_{3,\mathrm{TIM-LLA}} \quad L_{4,\mathrm{TIM-LLA}}]$ **(Approximated Branch Line Length)** $\mathbf{L}_{\mathrm{b,TIM-LLA}} = [L_{\mathrm{b}1,\mathrm{TIM-LLA}} \quad L_{\mathrm{b}2,\mathrm{TIM-LLA}} \quad L_{\mathrm{b}3,\mathrm{TIM-LLA}}]$		[200m 80m 80m 640m] [80m 0 160m] [640m 80m 80m 200m] [160m 0m 80m]	215.89m 94.55m	Default Operation Settings B
NNIM-LLA **Approximated Distribution Line Length** $\mathbf{L}_{\mathrm{NNIM-LLA}} = [L_{1,\mathrm{NNIM-LLA}} \quad L_{2,\mathrm{NNIM-LLA}} \quad L_{3,\mathrm{NNIM-LLA}} \quad L_{4,\mathrm{NNIM-LLA}}]$ **Approximated Branch Line Length** $\mathbf{L}_{\mathrm{b,NNIM-LLA}} = [L_{\mathrm{b}1,\mathrm{NNIM-LLA}} \quad L_{\mathrm{b}2,\mathrm{NNIM-LLA}} \quad L_{\mathrm{b}3,\mathrm{NNIM-LLA}}]$	1st execution	[115.25m 241.32m 240.29m 403.15m] [149.09m 150.59m 151.83m] [403.14m 240.29m 241.32m 115.25m] [151.83m 150.59m 149.09m]	196.26m 117.79m	Default Operation Settings B + 1 hidden layer
	2nd execution	[57.79m 303.94m 345.78m 292.49m] [158.60m 151.65m 157.30m] [292.49m 345.78m 303.94m 57.79m] [157.30m 151.65m 158.60m]	220.04m 164.63m	
	3nd execution	[115.94m 241.76m 237.44m 404.86m] [149.16m 148.34m 151.15m [404.86m 237.44m 241.76m 115.94m] [151.15m 148.34m 149.16m]	195.77m 116.98m	
	1st execution	[159.16m 206.79m 109.35m 524.70m] [152.25m 166.69m 155.59m] [524.70m 109.35m 206.79m 159.61m] [155.59m 166.69m 152.25m]	202.61m 111.83m	Default Operation Settings B + 2 hidden layers
	2nd execution	[117.63m 36.03m 388.25m 458.10m] [148.52m 151.64m 143.13m] [458.10m 388.25m 36.03m 117.63m] [143.13m 151.64m 148.52m]	232.84m 122.32m	
	3nd execution	[114.03m 254.92m 243.90m 387.73m] [148.62m 149.89m 152.30m] [387.73m 243.90m 254.92m 114.03m] [152.30m 149.89m 148.62m]	195.19m 122.30m	
	1st execution	[1,138.6m -1,148.3m -1,526.4m 2,467.4m] [92.93m 199.43m 33.93m] [2,467.4m -1,526.4m -1,148.3m 1,138.6m] [33.93m 199.43m 92.93m]	X X	Default Operation Settings B + 3 hidden layers
	2nd execution	[226.51m 29.39m 184.02m 559.97m] [131.44m 137.30m 126.66m] [559.97m 184.02m 29.39m 226.51m] [126.66m 137.30m 131.44m]	201.72m 87.68m	
	3nd execution	[1,942.86m -4,384.77m -1,045.92m 4,421.53m] [198.84m 449.87m 80.76m] [4,421.523m -1045.92m -4384.77m 1942.86m]	X X	

		[80.76m 449.87m 198.84m]		
	1st execution	[2,418.6m -3,347.0m -3,311.1m 5,169.2m] [-34.68m 164.43m -245.33m] [5,169.2m -3,311.1m -3,347.0m 2,418.6m] [-245.33m 164.43m -34.68m]	X X	Default Operation Settings B + 4 hidden layers
	2nd execution	[-98.26m 503.72m 473.95m 122.57m] [70.64m 83.27m 45.29m] [122.57m 473.95m 503.72m -98.26m] [45.29m 83.27m 70.64m]	X X	
	3rd execution	[-23.78m 636.36m 85.31m 302.10m] [163.17m 141.32m 148.92m] [302.10m 85.31m 636.36m -23.78m] [148.92m 141.32m 163.17m]	X X	
	1st execution	[2,147.6m -2,267.3m -2,547.8m 3,359.6m] [-572.73m -445.75m -594.49m] [3,359.6m -2,547.8m -2,267.3m 2,147.6m] [-594.49m -445.75m -572.73m]	X X	Default Operation Settings B + 5 hidden layers
	2nd execution	[298.26m -43.39m -95.89m 830.53m] [-407.63m -413.91m -464.40m] [830.53m -95.89m -43.39m 298.26m] [-464.40m -413.91m -407.63m]	X X	
	3rd execution	[575.63m -563.26m -771.69m 1,701.78m] [-123.70m -172.83m -236.46m] [1,701.78m -771.69m -563.26m 575.63m] [-236.46m -172.83m -123.70m]	X X	

Table 3
Distribution and Branch Line Length Approximations of TIM-LLA and NNIM-LLA for the Suburban Case and Default Operation Settings B (the symmetrical approximations are reported in blue font color)

Indicative OV LV BPL Topologies of Table 1		**Suburban case**	**RMSD**	**Notes**
Distribution Line Length $\mathbf{L}=[L_1 \quad L_2 \quad L_3 \quad 0]$ **Branch Line Length $\mathbf{L}_\mathrm{b}=[L_{\mathrm{b1}} \quad L_{\mathrm{b2}} \quad 0]$**		[500m 400m 100m 0m] [50m 10m 0m]	-	-
TIM-LLA **Approximated Distribution Line Length $\mathbf{L}_{\mathrm{TIM-LLA}}=$** $[L_{1,\mathrm{TIM-LLA}} \quad L_{2,\mathrm{TIM-LLA}} \quad L_{3,\mathrm{TIM-LLA}} \quad 0]$ **(Approximated Branch Line Length)** $\mathbf{L}_{\mathrm{b,TIM-LLA}}=[L_{\mathrm{b1,TIM-LLA}} \quad L_{\mathrm{b2,TIM-LLA}} \quad 0]$		[120m 100m 780m 0m] [160m 140m 0m] [780m 100m 120m 0m] [140m 160m 0m]	322.00m 168.78m	Default Operation Settings B
NNIM-LLA **Approximated Distribution Line Length $\mathbf{L}_{\mathrm{NNIM-LLA}}=$** $[L_{1,\mathrm{NNIM-LLA}} \quad L_{2,\mathrm{NNIM-LLA}} \quad L_{3,\mathrm{NNIM-LLA}} \quad 0]$ **Approximated Branch Line Length $\mathbf{L}_{\mathrm{b,NNIM-LLA}}=$** $[L_{\mathrm{b1,NNIM-LLA}} \quad L_{\mathrm{b2,NNIM-LLA}} \quad 0]$	1st execution	[55.07m 711.81m 233.12m 0m] [140.71m 159.39m 0m] [233.12m 711.81m 55.07m 0m] [159.39m 140.71m 0m]	221.51m 168.83m	Default Operation Settings B + 1 hidden layer
	2nd execution	[76.83m 665.77m 257.40m 0m] [144.41m 155.37m 0m] [257.40m 665.77m 76.83m 0m] [155.37m 144.41m 0m]	208.57m 150.81m	
	3rd execution	[49.86m 714.25m 235.89m 0m] [146.61m 163.70m 0m] [235.89m 714.25m 49.86m 0m]	224.50m 170.13m	

		[163.70m 146.61m 0m]		
	1st execution	[203.43m 164.18m 632.36m 0m] [57.94m 68.58m 0m] [632.36m 164.18m 203.43m 0m] [68.58m 57.94m 0m]	247.98m 111.14m	Default Operation Settings B + 2 hidden layers
	2nd execution	[60.75m 734.65m 204.60m 0m] [47.50m 71.93m 0m] [204.60m 734.65m 60.75m 0m] [71.93m 47.50m 0m]	213.71m 170.16m	
	3rd execution	[37.72m 762.84m 199.44m 0m] [134.24m 159.11m 0m] [199.44m 762.84m 37.72m 0m] [159.11m 134.24m 0m]	234.39m 190.19m	
	1st execution	[148.53m 385.22m 466.25m 0m] [0.04m -2.27m 0m] [466.25m 385.22m 148.53m 0m] [-2.27m 0.04m 0m]	X X	Default Operation Settings B + 3 hidden layers
	2nd execution	[843.26m -2,699.02m 2,852.79m 0m] [-334.88m -386.90m 0m] [2,852.79m -2699.02m 843.26m 0m] [-386.90m -334.88m 0m]	X X	
	3rd execution	[-48.50m 963.42m 85.48m 0m] [133.83m 215.75m 0m] [85.48m 963.42m -48.50m 0m] [215.75m 133.83m 0m]	X X	
	1st execution	[1,555.7m -5,874.3m 5,315.6m 0m] [-169.42m -186.57m 0m] [5,315.6m -5,874.3m 1,555.7m 0m] [-186.57m -169.42m 0m]	X X	Default Operation Settings B + 4 hidden layers
	2nd execution	[-840.97m 4,001.01m -2150.27m 0m] [-106.82m 106.07m 0m] [-2,150.27 4,001.01m -840.97m 0m] [106.07m -106.82m 0m]	X X	
	3rd execution	[-2,116.01m 9,237.87m -6,116.30m 0m] [-154.24m -2.59m 0m] [-6,116.30m 9,237.87m -2,116.01m 0m] [-2.59m -154.24m 0m]	X X	
	1st execution	[2,288.5m -8,430.0m 7,135.0m 0m] [565.12m 578.81m 0m] [7,135.0m -8,430.0m 2,288.5m 0m] [578.81m 565.12m 0m]	X X	Default Operation Settings B + 5 hidden layers
	2nd execution	[500.56m -774.33m 1,267.43m 0m] [130.94m 37.00m 0m] [1,267.43m -774.33m 500.56m 0m] [37.09m 130.94m 0m]	X X	

	3rd execution	[1,582.31m -5,718.78m 5,131.67m 0m] [-770.69m -853.92m 0m] [5,131.67m -5,718.78m 1,582.31m 0m] [-853.92m -770.69m 0m]	X X	

Table 4
Distribution and Branch Line Length Approximations of TIM-LLA and NNIM-LLA for the Rural Case and Default Operation Settings B (the symmetrical approximations are reported in blue font color)

Indicative OV LV BPL Topologies of Table 1		**Rural case**	**RMSD**	**Notes**
Distribution Line Length $\mathbf{L}=[L_1\quad L_2\quad 0\quad 0]$ **Branch Line Length** $\mathbf{L}_\mathrm{b}=[L_{\mathrm{b}1}\quad 0\quad 0]$		[600m 400m 0m 0m] [300m 0m 0m]	-	-
TIM-LLA **Approximated Distribution Line Length** $\mathbf{L}_{\mathrm{TIM-LLA}}=[L_{1,\mathrm{TIM-LLA}}\quad L_{2,\mathrm{TIM-LLA}}\quad 0\quad 0]$ **Approximated Branch Line Length** $\mathbf{L}_{\mathrm{b,TIM-LLA}}=[L_{\mathrm{b1,TIM-LLA}}\quad 0\quad 0]$		[220m 780m 0m 0m] [300m 0m 0m] [780m 220m 0m 0m] [300m 0m 0m]	203.12m 96.21m	Default Operation Settings B
NNIM-LLA **Approximated Distribution Line Length** $\mathbf{L}_{\mathrm{NNIM-LLA}}=[L_{1,\mathrm{NNIM-LLA}}\quad L_{2,\mathrm{NNIM-LLA}}\quad 0\quad 0]$ **Approximated Branch Line Length** $\mathbf{L}_{\mathrm{b,NNIM-LLA}}=[L_{\mathrm{b1,NNIM-LLA}}\quad 0\quad 0]$	1st execution	[265.66m 866.04m 0m 0m] [156.07m 0m 0m] [866.04m 265.66m 0m 0m] [156.07m 0m 0m]	223.51m 125.09m	Default Operation Settings B + 1 hidden layer
	2nd execution	[266.67m 733.33m 0m 0m] [233.33m 0m 0m] [733.33m 266.67m 0m 0m] [233.33m 0m 0m]	179.94m 75.59m	
	3rd execution	[264.20m 790.81m 0m 0m] [167.59m 0m 0m] [790.81m 264.20m 0m 0m] [167.59m 0m 0m]	201.08m 101.69m	
	1st execution	[247.53m 772.84m 0m 0m] [215.07m 0m 0m] [772.84m 247.53m 0m 0m] [215.07m 0m 0m]	196.56m 92.84m	Default Operation Settings B + 2 hidden layers
	2nd execution	[154.74m 839.50m 0m 0m] [198.02m 0m 0m] [839.50m 154.74m 0m 0m] [198.02m 0m 0m]	239.59m 135.18m	
	3rd execution	[204.86m 789.55m 0m 0m] [156.79m 0m 0m] [789.55m 204.86m 0m 0m] [156.79m 0m 0m]	216.59m 116.20m	
	1st execution	[216.21m 784.78m 0m 0m] [160.92m 0m 0m] [784.78m 216.21m 0m 0m] [160.92m 0m 0m]	212.03m 111.65m	Default Operation Settings B + 3 hidden layers
	2nd execution	[168.69m 817.75m 0m 0m] [159.63m 0m 0m]	233.07m	

		[817.75m 168.69m 0m 0m] [159.63m 0m 0m]	131.27m	
	3nd execution	[200.262m 799.74m 0m 0m] [300.01m 0m 0m] [799.74m 200.26m 0m 0m] [300.01m 0m 0m]	213.67m 106.76m	
	1st execution	[233.58m 728.75m 0m 0m] [274.36m 0m 0m] [728.75m 233.58m 0m 0m] [274.36m 0m 0m]	186.32m 80.11m	Default Operation Settings B + 4 hidden layers
	2nd execution	[244.33m 781.10m 0m 0m] [162.38m 0m 0m] [781.10m 244.33m 0m 0m] [162.38m 0m 0m]	203.78m 104.18m	
	3nd execution	[100.00m 900.00m 0m 0m] [300m 0m 0m] [900.00m 100.00m 0m 0m] [300.00m 0m 0m]	267.26m 160.36m	
	1st execution	[50m 950m 0m 0m] [300m 0m 0m] [950m 50m 0m 0m] [300m 0m 0m]	293.99m 187.08m	Default Operation Settings B + 5 hidden layers
	2nd execution	[209.52m 817.46m 0m 0m] [291.02m 0m 0m] [817.46m 209.52m 0m 0m] [291.02m 0m 0m]	216.08m 109.32m	
	3nd execution	[220.07m 779.93m 0m 0m] [300.00m 0m 0m] [779.93m 220.07m 0m 0m] [300.00m 0m 0m]	203.08m 96.18m	

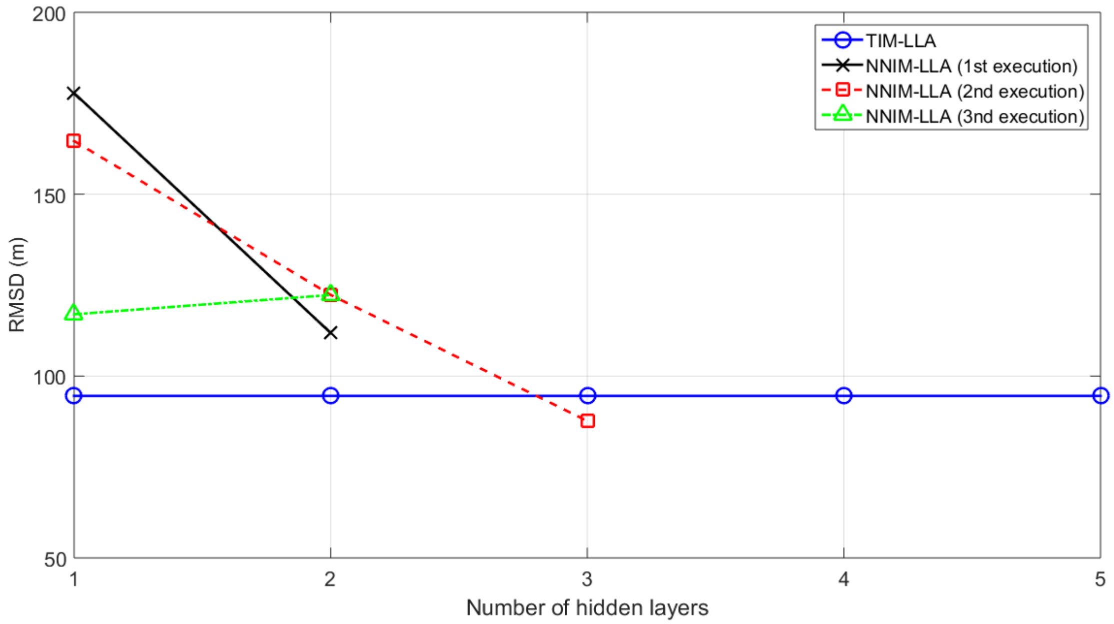

Figure 1. The best approximation RMSD of TIM-LLA and NNIM-LLA for the urban case A for different number of hidden layers when the default operation settings B are assumed.

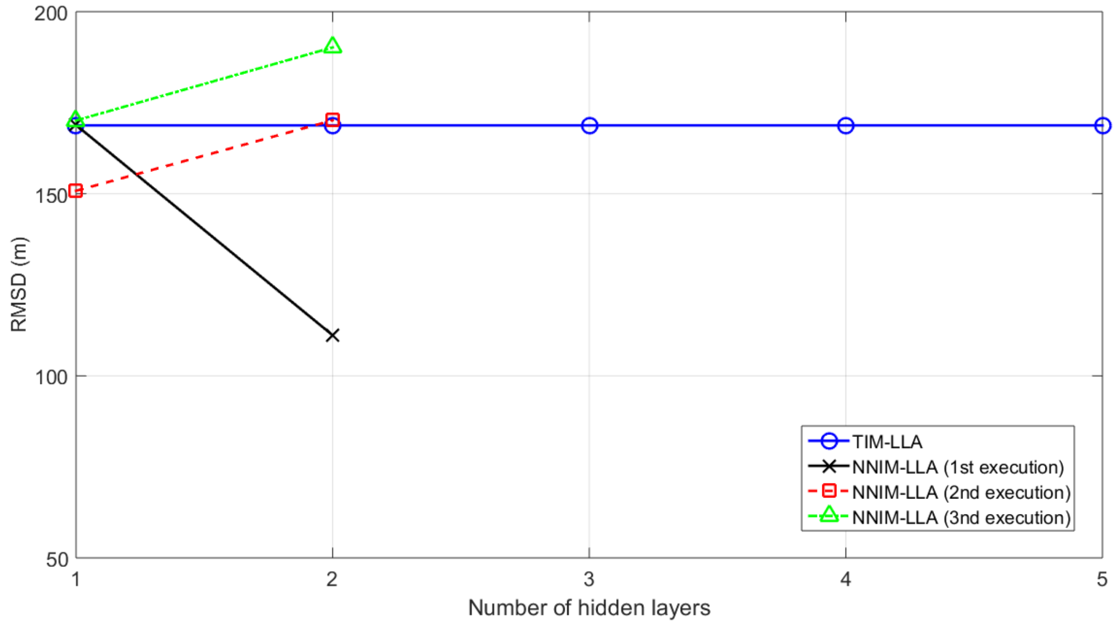

Figure 2. The best approximation RMSD of TIM-LLA and NNIM-LLA for the suburban case for different number of hidden layers when the default operation settings B are assumed.

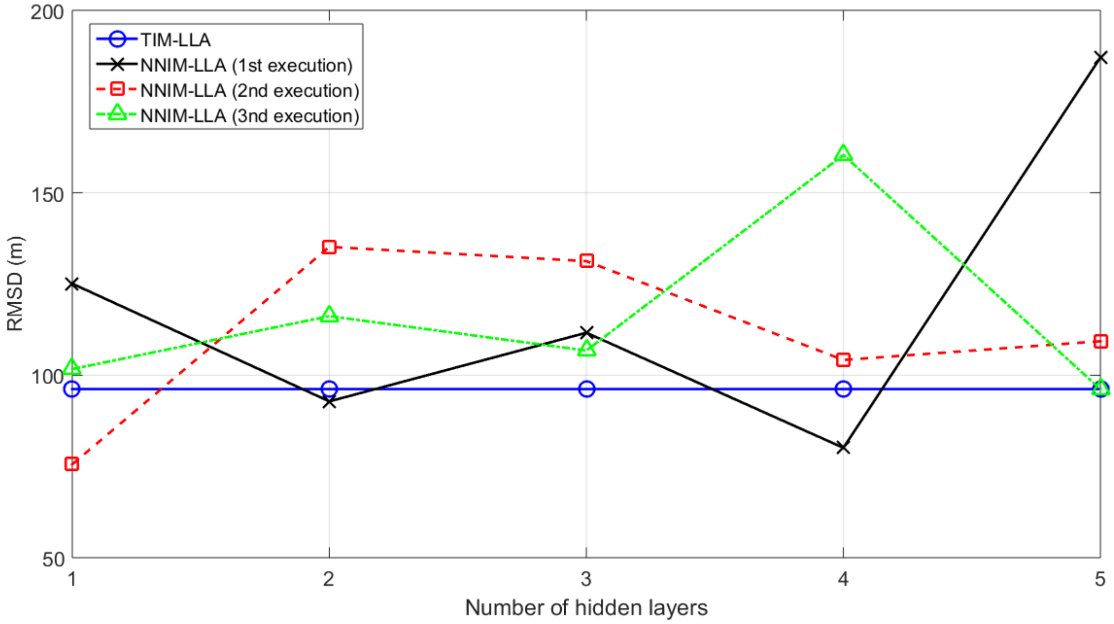

Figure 3. The best approximation RMSD of TIM-LLA and NNIM-LLA for the rural case for different number of hidden layers when the default operation settings B are assumed.

From Tables 2-4 and Figures 1-3, several interesting observations concerning the general approximation performance of TIM-LLA and NNIM-LLA can be discussed during the base scenario where the default settings B are applied, namely:

- With reference to the performance metric of RMSD, TIM-LLA better approximates the distribution and branch line lengths when the number of branches of the examined OV LV BPL topology remains high (*i.e.,* urban case A). For the suburban and rural case, there are at least two executions that the NNIM-LLA approximations present lower RMSDs in comparison with the TIM-LLA approximation, namely: (i) For the suburban case, the TIM-LLA best approximation RMSD is equal to 168.78m whereas the two NNIM-LLA approximations that present the lowest RMSD approximations are equal to 111.14m and 150.81m for 2 hidden layers (1st execution) and 1 hidden layer (2nd execution), respectively; and (ii) For the rural case, the TIM-LLA best approximation RMSD is equal to 96.21m whereas the three NNIM-LLA approximations that present the lowest approximation RMSDs are equal to 75.59m, 80.11m and 92.81m for 1 hidden layer (2nd execution), 4 hidden layers (1st execution) and 2 hidden layers (1st execution), respectively.
- TIM-LLA does not depend on the number of the hidden layers thus presenting a stable approximation behavior in Figures 1-3 for given OV LV BPL topology. In contrast, NNIM-LLA depends on the number of the hidden layers and the execution and it presents fluctuations when different numbers of hidden layers are applied for the different executions. In addition, unacceptable NNIM-LLA approximations may occur when high numbers of hidden layers are assumed; in the urban case A and suburban case, unacceptable approximations occur for numbers of hidden layers that are greater than 3 and 2, respectively. Anyway, as

the number of hidden layers rises, the differences among the executions of the NNIM-LLA approximations become considerable.

- By assuming up to 5 hidden layers and up to 3 executions per hidden layer, stochastic nature of NNIM-LLA is unveiled. In [1], the preparation of the TIM OV LV BPL topology database significantly has affected the branch number approximations of NNIM-BNI when the default operation settings A had been assumed; since the number of OV LV BPL topologies with 3 branches is significantly higher than the number of OV LV BPL topologies with 2 branches that is again significantly higher than the number of OV LV BPL topologies with 1 branch, NNIM-BNI seemed to favor approximations close to 3 branches since greater number of OV LV BPL topologies of 3 branches are initially present in the TIM OV LV BPL topology database due to its preparation process. The representative sets of the TIM OV LV BPL topology database improved the performance of NNIM-BNI. In this paper, the concept of the representative sets of the TIM OV LV BPL topology database of [1] has been adopted by default during the preparation of the default operation settings B; only the OV LV BPL topologies with the same number of branches with the examined one are considered from the TIM OV LV BPL topology database in each approximation of the TIM-LLA and NNIM-LLA. Hence, the preparation of the TIM OV LV BPL topology database with the default operation settings B appears to equally treat with the OV LV BPL topologies in terms of RMSDS and the relative position of the TIM-LLA and NNIM-LLA approximations.
- Although RMSD differences among the different NNIM-LLA executions may occur for given number of hidden layer and examined indicative OV LV BPL topology, these differences remain relatively small when the number of the hidden layers is also low so that only one execution is going to be applied for the following NNIM-LLA simulations, as already done in [1]. Numerically, the greatest RMSD differences between the best approximations of NNIM-LLA executions for given number of hidden layers and indicative OV LV BPL topology are: (i) *Urban case A*: 60.81m and 10.49m for 1 and 2 hidden layers, respectively. Note that there is no difference computation for the case of 3 layers where only one successful approximation occurs; (ii) *Suburban case*: 19.32m and 79.05m for 1 and 2 hidden layers, respectively; and (iii) *Rural case*: 49.50m, 42.32m, 24.51m, 80.25m and 90.90m for 1, 2, 3, 4 and 5 hidden layers, respectively.
- High length spacings of the TIM OV LV BPL topology database imply high RMSD values both in TIM-LLA and NNIM-LLA approximations. Lower length spacings during the preparation of TIM OV LV BPL topology database may allow more accurate approximations regarding the approximated branch lengths and lower RMSDs for both approximations.

After the application of the default operation settings B, TIM-LLA and NNIM-LLA appear almost equivalent approximation performances for the OV LV BPL topologies of 1, 2 and 3 branches. Wanting to further investigate the approximation performance and discover possible improvements of the two methods, TIM-LLA approximations slightly prevail for the OV LV BPL topologies of 3 branches whereas NNIM-LLA approximations are more accurate for the OV LV BPL topologies of 1 and 2 branches. With reference to Sec. 4.3 and 4.4 of [1], the impact of R on TIM-LLA performance and the impact of participation percentages on NNIM-LLA performance are examined in Secs. 4.2 and 4.3, respectively, so as to explore any scope for improving the TIM-LLA and NNIM-LLA approximation performances with reference to the base scenario of the default operation settings B.

4.2 The Impact of *R* on TIM-LLA Performance

In accordance with [1], the TIM-BNI branch number approximation $N_{\mathrm{TIM-BNI}}$ has come from the average value of the branch numbers of the *R* OV LV BPL topologies of the TIM OV LV BPL topology database that present the *R* lowest RMSDs among the computed ones. In the default operation settings A, the default value of *R* was equal to 5. In the default operation settings B of this paper, the same default value of *R*=5 is assumed for the TIM-LLA while the procedure for approximating the distribution and branch line lengths remains almost the same; say, for each of the line length approximations, the mean value of the *R* lowest TIM-LLA RMSDs is applied. In Table 5, the distribution and branch line length approximations of TIM-LLA are reported for the urban case A when the default operation settings B are assumed but for six different values of *R* (i.e., 1, 2, 3, 5, 7 and 10). Apart from the distribution and branch line length approximations, the actual distribution and branch line lengths of the urban case A are presented. Also, RMSDs of TIM-LLA approximations for the urban case A are reported when the previous six different values of *R* are applied. Tables 6 and 7 are same with Table 5 but for the suburban and rural case of Table 1, respectively. Similarly to the Tables 2-4, the original approximations are given in black font color whereas the symmetrical approximations of TIM-LLA are given in blue font color in Tables 5-7.

To facilitate the benchmark of TIM-LLA among the three indicative OV LV BPL topologies of Table 1 when different values of *R* are examined, the RMSD results of Tables 5-7 are presented in Figure 4. More analytically, with reference to the RMSD of the original and symmetrical approximations, best TIM-LLA approximations are plotted with respect to the value of *R* for the urban case A, suburban case and rural case. Similarly to Figures 1-3, the best approximation between the original and symmetrical approximations are shown for TIM-LLA given the value of *R*.

Table 5
Distribution and Branch Line Length Approximations of TIM-LLA for the Urban Case A, Default Operation Settings B and Different *R* Values (the symmetrical approximations are reported in blue font color)

Indicative OV LV BPL Topologies of Table 1	***R* Value**	**Urban case A** **(Typical urban case)**	**RMSD**	**Notes**
Distribution Line Length $\mathbf{L} = [L_1 \quad L_2 \quad L_3 \quad L_4]$ **Branch Line Length** $\mathbf{L}_{\mathrm{b}} = [L_{\mathrm{b1}} \quad L_{\mathrm{b2}} \quad L_{\mathrm{b3}}]$		[500m 200m 100m 200m] [8m 13m 10m]	-	-
TIM-LLA **Approximated Distribution Line Length** $\mathbf{L}_{\mathrm{TIM-LLA}} = [L_{1,\mathrm{TIM-LLA}} \quad L_{2,\mathrm{TIM-LLA}} \quad L_{3,\mathrm{TIM-LLA}} \quad L_{4,\mathrm{TIM-LLA}}]$ **Approximated Branch Line Length** $\mathbf{L}_{\mathrm{b,TIM-LLA}} = [L_{\mathrm{b1,TIM-LLA}} \quad L_{\mathrm{b2,TIM-LLA}} \quad L_{\mathrm{b3,TIM-LLA}}]$	1	[0m 0m 0m 1000m] [0m 0m 0m] [1,000m 0m 0m 0m] [0m 0m 0m]	366.52m 220.50m	Default Operation Settings B except for *R* value
	2	[200m 50m 50m 700m] [50m 0m 100m] [700m 50m 50m 200m] [100m 0m 50m]	231.47m 103.67m	Default Operation Settings B except for *R* value
	3	[233.33m 66.67m 66.67m 633.33m] [66.67 0m 133.33m] [633.33m 66.67m 66.67m 233.33m] [133.33m 0m 66.67m]	205.84m 90.13m	Default Operation Settings B except for *R* value
	5	[200m 80m 80m 640m] [80m 0 160m] [640m 80m 80m 200m] [160m 0m 80m]	215.89m 94.55m	Default Operation Settings B
	7	[185.71m 58.71m 58.71m 642.86m] [100m 0m 157.14m] [642.86m 85.71m 85.71m 185.71m] [157.14m 0m 100m]	219.89m 95.91m	Default Operation Settings B except for *R* value
	10	[160m 180m 90m 570m] [100m 0m 170m] [570m 90m 180m 160m] [170m 0m 100m]	202.57m 92.21m	Default Operation Settings B except for *R* value

Table 6
Distribution and Branch Line Length Approximations of TIM-LLA for the Suburban Case, Default Operation Settings B and Different *R* Values (the symmetrical approximations are reported in blue font color)

Indicative OV LV BPL Topologies of Table 1	***R* Value**	**Suburban case**	**RMSD**	**Notes**
Distribution Line Length $\mathbf{L} = [L_1 \quad L_2 \quad L_3 \quad 0]$ **Branch Line Length** $\mathbf{L}_{\mathrm{b}} = [L_{\mathrm{b1}} \quad L_{\mathrm{b2}} \quad 0]$		[500m 400m 100m 0m] [50m 10m 0m]	-	-
TIM-LLA **Approximated Distribution Line Length** $\mathbf{L}_{\mathrm{TIM-LLA}} = [L_{1,\mathrm{TIM-LLA}} \quad L_{2,\mathrm{TIM-LLA}} \quad L_{3,\mathrm{TIM-LLA}} \quad 0]$ **Approximated Branch Line Length** $\mathbf{L}_{\mathrm{b,TIM-LLA}} = [L_{\mathrm{b1,TIM-LLA}} \quad L_{\mathrm{b2,TIM-LLA}} \quad 0]$	1	[0m 100m 900m 0m] [100m 200m 0m] [900m 100m 0m] [200m 100m]	381.46m 203.75m	Default Operation Settings B except for *R* value
	2	[0m 100m 900m 0] [150m 150m 0m]	379.77m	Default Operation Settings B except

		[900m 100m 0m 0m] [150m 150m 0m]	203.40m	for *R* value
	3	[66.67m 100m 833.33m 0m] [166.67m 133.33m 0m] [833.33m 100m 66.67m 0m] [133.33m 166.67m]	347.31m 182.72m	Default Operation Settings B except for *R* value
	5	[120m 100m 780m 0m] [160m 140m 0m] [780m 100m 120m] [140m 160m 0m]	322.00m 168.78m	Default Operation Settings B
	7	[128.57m 100m 771.43m 0m] [157.14m 142.86m 0m] [771.43m 100m 128.57m 0m] [142.86m 157.14m 0m]	318.01m 166.80m	Default Operation Settings B except for *R* value
	10	[200m 100m 700m 0m] [150m 150m 0m] [700m 100m 200m 0m] [150m 150m 0m]	282.26m 155.66m	Default Operation Settings B except for *R* value

Table 7
Distribution and Branch Line Length Approximations of TIM-LLA for the Rural Case, Default Operation Settings B and Different *R* Values (the symmetrical approximations are reported in blue font color)

Indicative OV LV BPL Topologies of Table 1	***R* Value**	**Rural case**	**RMSD**	**Notes**
Distribution Line Length $\mathbf{L}=[L_1\quad L_2\quad 0\quad 0]$ **Branch Line Length** $\mathbf{L}_{\mathrm{b}}=[L_{\mathrm{b1}}\quad 0\quad 0]$		[600m 400m 0m 0m] [300m 0m 0m]	-	-
TIM-LLA **Approximated Distribution Line Length** $\mathbf{L}_{\mathrm{TIM-LLA}}=[L_{1,\mathrm{TIM-LLA}}\quad L_{2,\mathrm{TIM-LLA}}\quad 0\quad 0]$ **Approximated Branch Line Length** $\mathbf{L}_{\mathrm{b,TIM-LLA}}=[L_{\mathrm{b1,TIM-LLA}}\quad 0\quad 0]$	1	[200m 800m 0m 0m] [300m 0m 0m] [800m 200m 0m 0m] [300m]	213.81m 106.90m	Default Operation Settings B except for *R* value
	2	[150m 850m 0m 0m] [300m 0m 0m] [850m 150m 0m 0m] [300m 0m 0m]	240.54m 133.63m	Default Operation Settings B except for *R* value
	3	[200m 800m 0m 0m] [300m 0m 0m] [800m 200m 0m 0m] [300m 0m 0m]	213.81m 106.90m	Default Operation Settings B except for *R* value
	5	[220m 780m 0m 0m] [300m 0m 0m] [780m 220m 0m 0m] [300m 0m 0m]	203.12m 96.21m	Default Operation Settings B
	7	[171.43m 828.57m 0m 0m] [214.29m 0m 0m] [828.57m 171.43m 0m 0m] [214.29m 0m 0m]	231.36m 126.40m	Default Operation Settings B except for *R* value

	10	[210m 790m 0m 0m] [150m 0m 0m] [790m 210m 0m 0m] [150m 0m 0m]	216.04m 116.31m	Default Operation Settings B except for *R* value

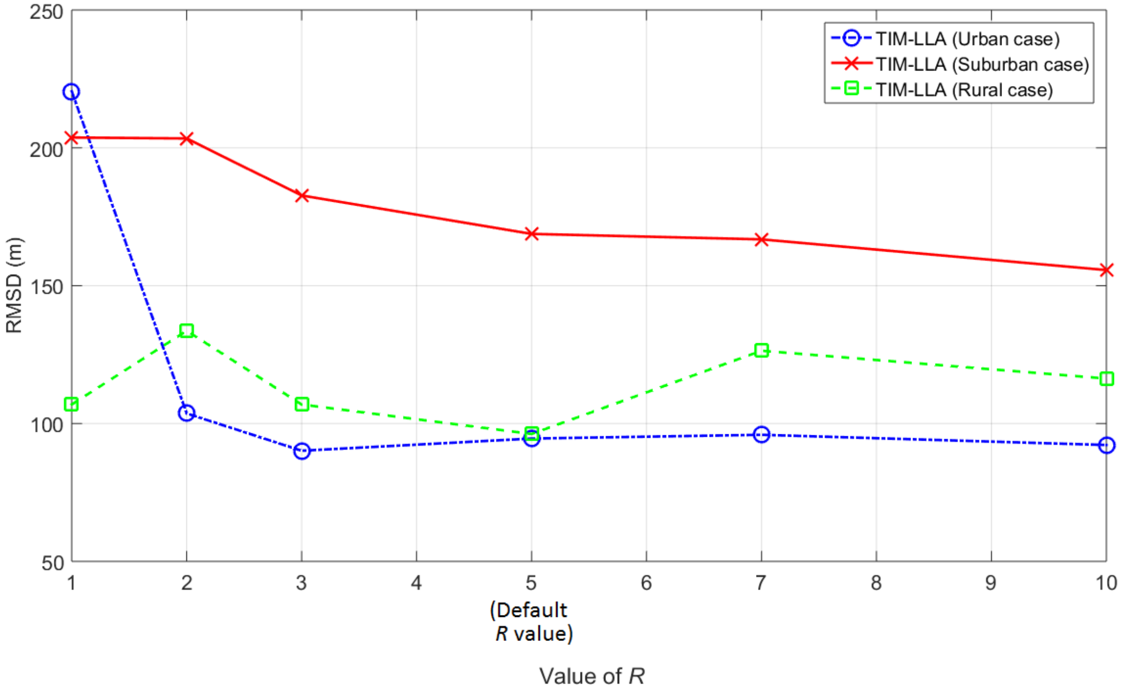

Figure 4. The best approximation RMSD of TIM-LLA for the urban case A, suburban case and rural case for different values of *R* when the default operation settings B are assumed.

From Tables 5-7 and Figure 4, the following remarks concerning the RMSD dependence on the value of *R* can be pointed out, namely:

- When *R* is equal to 1, only one OV LV BPL topology from the TIM OV LV BPL topology database is chosen by the TIM-LLA for approximating each of the examined indicative OV LV BPL topologies. More specifically:
    - When the urban case A is examined, TIM-LLA gives as its best approximation an OV LV BPL topology where its first distribution line length $L_{1,\mathrm{TIM-LLA}}$ is equal to 1000m and the other three ones are equal to 0m. As the approximated branch line lengths of the best TIM-LLA approximation are concerned, these are all equal to 0. Examining the aforementioned best OV LV BPL topology approximation of TIM-LLA, this approximation seems to the LOS case of Table 1. Actually, the short branch line lengths of the urban case A cannot be accurately approximated by TIM-LLA due to the assumed high spacing of branch lengths (i.e., 100m). Hence, the best OV LV BPL topology approximation of TIM-LLA is characterized by the shortest possible branch line lengths that are close to the actual ones anyway inferring their multipath character (i.e., 0m).

  Note that the RMSD of this *R* value is the worst one among the RMSDs of all the *R* values.
  - When the suburban and rural cases are examined, the approximated OV LV BPL topologies by the TIM-LLA are characterized by RMSD values that are close to their respective best ones thus offering decent approximations.

  In total, TIM-LLA approximations of *R*=1 value are considered to be decent for the OV LV BPL topologies of lower number of branches (*i.e.*, 1 or 2 branches) whereas they become inaccurate when high number of branches occur (*i.e.,* 3 branches).
- When *R* is greater than 1, mean values among the chosen OV LV BPL topologies occur for the approximated distribution and branch line lengths thus allowing better approximations of the real distribution and branch line lengths. Indeed, the RMSDs of the best and the worst approximations for each of the examined indicative OV LV BPL topologies decrease as the value of *R* increases until the *R* becomes equal to 5 (*i.e.*, default value of the operation settings B). For *R* values that are greater than 5, RMSDs of the TIM-LLA approximations: (i) remain stable for the urban case A; (ii) slowly decrease for the suburban case; and (iii) increase for the rural case.
- Strictly numerically and with reference to Figure 4, the best of the best approximations of TIM-LLA for the three indicative OV LV BPL topologies are: (i) *Urban case A*: when the *R* value is equal to 3, its minimum RMSD of all TIM-LLA approximations is equal to 90.13m; (ii) *Suburban case*: when *R* is equal to 10, its minimum RMSD of all TIM-LLA approximations is equal to 155.66m; and (iii) *Rural case*: when the *R* value is equal to 5, its minimum RMSD of all TIM-LLA approximations is equal to 96.21m.

From the previous analysis, the assumption of the *R* value that is equal to 5 in the operation settings B allows TIM-LLA to decently approximate the distribution and branch line lengths of all the indicative OV LV BPL topologies of Table 1. Anyway, the *R* value of 5 came from the findings of [1] where this *R* value also helped towards satisfactory approximations concerning the number of branches of the indicative OV LV BPL topologies of Table 1. In order to examine whether further performance improvement is feasible for NNIM-LLA beyond the operation settings B, the impact of participation percentages on NNIM-LLA performance is examined in Sec. 4.3.

4.3 The Impact of Participation Percentages on NNIM-LLA Performance

Until now, the *R* value that affects the operation of TIM-LLA has been studied in the case that TIM-LLA performance can further be improved with respect to the performance after applying default operation settings B. In this subsection, the factor that affects the approximation performance of NNIM-LLA is analyzed; say, the participation percentages of the three phases of the NNIM-LLA operation; training, validation and testing phases. In Table 8, the distribution and branch line length approximations of NNIM-LLA are reported for the urban case A when the default operation settings B are assumed but for seven different combinations of the training, validation and testing participation percentages – *i.e.*, (10%, 45%, 45%), (30%, 35%, 35%), (50%, 25%, 25%), (70%, 15%, 15% default), (80%, 10%, 10%), (90%, 5%, 5%) and (98%, 1%, 1%)– . Apart from the distribution and branch line length approximations, the actual distribution and branch line lengths of the urban case A are presented. Also, RMSDs of

NNIM-LLA approximations for the urban case A, when the previous seven combinations of the training, validation and testing participation percentages are applied, are reported. Tables 9 and 10 are same with Table 8 but for the suburban and rural case of Table 1, respectively. Similarly to Tables 2-7, the original approximations are given in black font color whereas the symmetrical approximations of NNIM-LLA are given in blue font color in Tables 8-10.

To visualize the information of Tables 8-10, the RMSD results of Table 8 concerning the different participation percentages of the three phases of NNIM-LLA are presented in Figure 5 when the urban case A is approximated. More specifically, with reference to the RMSD of the original and symmetrical approximations, NNIM-LLA is plotted with respect to the number of hidden layers for the urban case A. The best approximations between the original and symmetrical approximations are shown for NNIM-LLA given the number of the hidden layers and the participation percentages of the three phases. Note that only one execution of NNIM-LLA is here demonstrated for each set of the participation percentages of the three phases. In Figures 6 and 7, similar curves are given with Figure 8 but for the suburban and rural case with reference to Table 9 and 10, respectively.

From Figures 5-7, the significance of the participation percentages of the three phases of NNIM-LLA is highlighted. In contrast with [1] where high participation percentages of the validation and testing phases favored low RMSDs, a more balanced ratio among the participation percentages is here promoted for achieving lower RMSDs. Strictly numerically and with reference to Figures 5-7, the best of the best approximations of NNIM-LLA for the three indicative OV LV BPL topologies are:

- *Urban case A*: when the participation percentages for training, validation and testing are equal to 50%, 25% and 25%, respectively, and 3 hidden layers are assumed, the minimum RMSD of all NNIM-LLA best approximations is equal to 103.31m. Anyway, the best RMSDs of all sets of participation percentages except for (10%, 45%, 45%) and (30%, 35%, 35%) remain very close to the minimum RMSD of 103.31m when hidden layers from 1 to 3 are assumed.
- *Suburban case*: when the participation percentages for training, validation and testing are equal to 80%, 10% and 10%, respectively, and 2 hidden layers are assumed, the minimum RMSD of all NNIM-LLA best approximations is equal to 72.58m. Anyway, the RMSDs of the sets (90%, 5%, 5%), (10%, 45%, 45%) and (98%, 1%, 1%) remain close to the aforementioned minimum one.
- *Rural case*: when the participation percentages for training, validation and testing are equal to 30%, 35% and 35%, respectively, and 4 hidden layers are assumed, the minimum RMSD of all NNIM-LLA best approximations is equal to 68.33m. Anyway, the RMSD of the sets (10%, 45%, 45%), (80%, 10%, 10%), (50%, 25%, 25%) and (70%, 15%, 15%) remain close to the aforementioned minimum one.

Table 8
Distribution and Branch Line Length Approximations of NNIM-LLA for the Urban Case A, Default Operation Settings B and Different Participation Percentage Values and Hidden Layers (the symmetrical approximations are reported in blue font color)

Indicative OV LV BPL Topologies of Table 1	**Participation Percentages for Training, Validation and Testing (%,%,%)**	**Urban case A (Typical urban case)**	**RMSD**	**Notes**
Distribution Line Length L =[L_1 L_2 L_3 L_4] **Branch Line Length $\mathbf{L_b}$** =[L_{b1} L_{b2} L_{b3}]		[500m 200m 100m 200m] [8m 13m 10m]	-	-
NNIM-LLA **Approximated Distribution Line Length $\mathbf{L_{NNIM-LLA}}$** = [$L_{1,NNIM-LLA}$ $L_{2,NNIM-LLA}$ $L_{3,NNIM-LLA}$ $L_{4,NNIM-LLA}$] **Approximated Branch Line Length $\mathbf{L_{b,NNIM-LLA}}$** = [$L_{b1,NNIM-LLA}$ $L_{b2,NNIM-LLA}$ $L_{b3,NNIM-LLA}$]	(10%,45%,45%)	[152.03m 75.72m 395.36m 373.71m] [150.18m 155.66m 163.99m] [373.71m 395.33m 75.72m 152.03m] [163.99m 155.66m 150.18m]	213.21m 131.65m	Default Operation Settings B + 1 hidden layer
	(30%,35%,35%)	[114.06m 230.89m 251.05m 403.99m] [148.62m 150.11m 152.63m] [403.99m 251.05m 230.89m 114.06m] [152.63m 150.11m 148.62m]	197.57m 116.66m	
	(50%,25%,25%)	[104.83m 239.65m 256.25m 398.64m] [146.47m 151.34m 149.72m] [398.64m 256.25m 239.65m 104.83m] [149.72m 151.34m 146.47m]	199.80m 119.43m	
	(70%,15%,15%) Default	[115.25m 241.32m 240.29m 403.14m] [149.09m 150.59m 151.83m] [403.14m 240.29m 241.32m 115.25m] [151.83m 150.59m 149.09m]	196.26m 117.79m	
	(80%,10%,10%)	[109.94m 202.13m 271.94m 415.98m] [149.63m 150.41m 151.07m] [415.98m 271.94m 202.13m 109.94m] [151.07m 150.41m 149.63m]	202.56m 113.15m	
	(90%,5%,5%)	[115.50m 240.79m 239.61m 404.10m] [149.30m 150.40m 152.04m] [404.10m 239.61m 240.79m 115.50m] [152.04m 150.40m 149.30m]	196.28m 117.57m	
	(98%,1%,1%)	[128.16m 74.86m 335.59m 461.38m] [152.87m 154.03m 153.24m] [461.38m 335.59m 74.86m 128.16m] [153.24m 154.03m 152.87m]	220.11m 111.52m	
	(10%,45%,45%)	[81.01m 281.34m 362.84m 269.12m] [123.07m 118.41m 101.52m] [269.12m 362.84m 281.34m 81.01m] [101.52m 118.41m 123.07m]	203.10m 150.95m	Default Operation Settings B + 2 hidden layers
	(30%,35%,35%)	[110.31m 319.60m 77.59m 494.45m] [147.84m 147.20m 158.14m] [494.45m 77.59m 319.60m 110.31m] [158.14m 147.20m 147.84m]	211.42m 136.71m	
	(50%,25%,25%)	[2,638.42m -3,780.68m -5,118.86m 7,205.92m] [-684.51m -723.02m -1,567.15m]	X	

		[7,205.92 -5,118.86m -3,780.68m 2,638.42m] [-1,567.15m -723.02m -684.51m]	X	
	(70%,15%,15%) Default	[159.16m 206.79m 109.35m 524.70m] [152.25m 166.69m 155.59m] [524.70m 109.35m 206.79m 159.16m] [155.59m 166.69m 152.25m]	202.61m 111.83m	
	(80%,10%,10%)	[115.07m 232.10m 267.55m 385.28m] [151.25m 150.15m 152.05m] [385.28m 267.55m 232.10m 115.07m] [152.05m 150.15m 151.25m]	196.80m 120.65m	
	(90%,5%,5%)	[111.40m 237.59m 270.54m 380.47m] [149.35m 150.32m 151.75m] [380.47m 270.54m 237.59m 111.40m] [151.75m 150.32m 149.35m]	197.49m 122.46m	
	(98%,1%,1%)	[122.05m 12.36m 365.42m 500.15m] [151.15m 151.52m 144.57m] [500.15m 365.42m 12.36m 122.05m] [144.57m 151.52m 151.15m]	237.96m 118.85m	
	(10%,45%,45%)	[130.75m 35.15m 384.33m 518.12m] [155.19m 171.88m 166.20m] [518.12m 384.33m -35.15m 130.75m] [166.20m 171.88m 155.19m]	252.13m X	Default Operation Settings B + 3 hidden layers
	(30%,35%,35%)	[48.76m 383.16m 313.44m 254.19m] [135.21m 151.39m 140.66m] [254.19m 313.44m 383.16m 48.76m] [140.66m 151.39m 135.21m]	219.76m 180.78m	
	(50%,25%,25%)	[194.67m 51.72m 85.22m 668.38m] [111.15m 121.44m 102.01m] [668.38m 85.22m 51.72m 194.67m] [102.01m 121.44m 111.15m]	228.56m 103.31m	
	(70%,15%,15%) Default	[1,138.55m -1,148.34m -1,526.45m 2,467.43m] [92.93m 199.43m 33.93m] [2,467.43m -1,526.45m -1,148.34m 1,138.55m] [33.93m 199.43m 92.93m]	X X	
	(80%,10%,10%)	[139.43m 163.65m 265.94m 430.50m] [148.44m 148.81m 150.59m] [430.50m 265.94m 163.65m 139.43m] [150.59m 148.81m 148.44m]	196.37m 103.39m	
	(90%,5%,5%)	[1,758.12m -1,863.26m -2,534.78m 3,494.16m] [-6.63m -66.63m 33.56m] [3,494.16m -2,534.78m -1,863.26m 1,758.12m] [33.56m -66.63m -6.63m]	X X	
	(98%,1%,1%)	[1,691.61m -1,781.63m -2,535.55m 3,422.96m] [134.46m 70.35m 113.19m] [3,422.96m -2,535.55m -1,781.63m 1,691.61m] [113.19m 70.35m 134.46m]	X X	
	(10%,45%,45%)	[59.73m 342.82m 342.04m 279.28m]	224.42m	Default

		[168.37m 175.88m 155.58m] [279.28m 342.04m 342.82m 59.73m] [155.58m 175.88m 168.37m]	177.65m	Operation Settings B + 4 hidden layers
	(30%,35%,35%)	[767.69m -744.19m -1,099.11m 2,058.23m] [426.92m 57.38m 131.21m] [2,058.23m -1,099.11m -744.19m 767.69m] [131.21m 57.38m 426.92m]	X X	
	(50%,25%,25%)	[1,213.45m -1,805.84m -1,945.48m 3,314.22m] [361.26m 53.03m 161.95m] [3,314.22m -1,945.48m -1,805.84m 1,213.45m] [161.95m 53.03m 361.26m]	X X	
	(70%,15%,15%) Default	[2418.57m -3346.98m -3311.13m 5169.19m] [-34.68m 164.43m -245.33m] [5169.19m -3311.13m -3346.98m 2418.57m] [-245.33m 164.43m -34.68m]	X X	
	(80%,10%,10%)	[1,476.12m -1,638.64m -2,102.72m 3,167.57m] [63.59m 156.05m 44.39m] [3,167.57m -2,102.72m -1,638.64m 1,476.12m] [44.39m 156.05m 63.59m]	X X	
	(90%,5%,5%)	[260.03m 70.47m -37.75m 704.40m] [-5.44m 0.78m 33.33m] [704.40m -37.75m 70.47m 260.03m] [33.33m 0.78m -5.44m]	X X	
	(98%,1%,1%)	[1,220.62m -1,354.31m -1,636.03m 2,742.52m] [-159.19m 2.78m -230.15m] [2,742.52m -1,636.03m -1,354.31m 1,220.62m] [-230.15m 2.78m -159.19m]	X X	
	(10%,45%,45%)	[86.68m 223.46m 285.89m 384.12m] [151.28m 149.58m 146.44m] [384.12m 285.89m 223.46m 86.68m] [146.44m 149.58m 151.28m]	206.20m 123.44m	Default Operation Settings B + 5 hidden layers
	(30%,35%,35%)	[1,329.10m -1,637.87m -2,422.43m 3,527.58m] [-268.04m -189.39m -182.65m] [3,527.58m -2,422.43m -1,637.87m 1,329.10m] [-182.65m -189.39m -268.04m]	X X	
	(50%,25%,25%)	[1,229.08m -1,748.39m -1,926.08m 3,299.86m] [-98.19m -193.91m -161.55m] [3,299.86m -1,926.08m -1,748.39m 1,229.08m] [-161.55m -193.91m -98.19m]	X X	
	(70%,15%,15%) Default	[2,147.65m -2,267.28m -2,547.68m 3,359.61m] [-572.72m -445.75m -594.49m] [3,359.61m -2,547.68m -2,267.28m 2,147.65m] [-594.49m -445.75m -572.72m]	X X	
	(80%,10%,10%)	[924.90m -1,041.43m -1,701.15m 2,614.81m] [6.23m -130.81m -117.23m] [2,614.81m -1,701.15m -1,041.43m 924.90m] [-117.23m -130.81m 6.23m]	X X	
	(90%,5%,5%)	[-2,978.36m 4,909.27m 6,219.73m -7,120.47m] [185.18m -395.09m 1,032.06m]	X	

		[-7,120.47m 6,219.73m 4,909.27m -2,978.36m] [1,032.06m -395.09m 185.18m]	X	
	(98%,1%,1%)	[-0.29m 435.05m 558.04m 11.29m] [164.40m 174.86m 216.50m]	X	
		[11.29m 558.04m 435.05m -0.29m] [216.50m 174.86m 164.40m]	X	

Table 9
Distribution and Branch Line Length Approximations of NNIM-LLA for the Suburban Case, Default Operation Settings B and Different Participation Percentage Values and Hidden Layers (the symmetrical approximations are reported in blue font color)

Indicative OV LV BPL Topologies of Table 1	**Participation Percentages for Training, Validation and Testing (%,%,%)**	**Suburban case**	**RMSD**	**Notes**
Distribution Line Length L =[L_1 L_2 L_3 0] **Branch Line Length L$_b$** =[L_{b1} L_{b2} 0]		[500m 400m 100m 0m] [50m 10m 0m]	-	-
NNIM-LLA **Approximated Distribution Line Length L$_{NNIM-LLA}$** = [$L_{1,NNIM-LLA}$ $L_{2,NNIM-LLA}$ $L_{3,NNIM-LLA}$ 0] **Approximated Branch Line Length L$_{b,NNIM-LLA}$** = [$L_{b1,NNIM-LLA}$ $L_{b2,NNIM-LLA}$ 0]	(10%,45%,45%)	[103.36m 699.47m 197.18m 0m] [100.47m 158.92m 0m]	200.42m	Default Operation Settings B + 1 hidden layer
		[197.18m 699.47m 103.36m 0m] [158.92m 100.47m 0m]	169.64m	
	(30%,35%,35%)	[43.07m 755.35m 201.58m 0m] [135.74m 158.83m 0m]	231.42m	
		[201.58m 755.35m 43.07m 0m] [158.83m 135.74m 0m]	187.55m	
	(50%,25%,25%)	[73.90m 691.65m 234.46m 0m] [146.66m 151.93m 0m]	211.86m	
		[234.46m 691.65m 73.90m 0m] [151.93m 146.66m 0m]	162.71m	
	(70%,15%,15%) Default	[55.07m 711.81m 233.12m 0m] [140.71m 159.39m 0m]	221.51m	
		[233.12m 711.81m 55.07m 0m] [159.39m 140.71m 0m]	168.83m	
	(80%,10%,10%)	[59.01m 711.03m 229.97m 0m] [142.19m 162.93m 0m]	220.39m	
		[229.97m 711.03m 59.01m 0m] [162.93m 142.19m 0m]	169.69m	
	(90%,5%,5%)	[146.19m 325.48m 528.55m 0m] [146.03m 156.65m 0m]	222.04m	
		[528.55m 325.48m 146.19m 0m] [156.65m 146.03m 0m]	74.05m	
	(98%,1%,1%)	[-1,347.51m 5,757.91m -3,349.96m 0m] [-79.40m 234.97m 0m]	X	
		[-3349.956m 5,757.91m -1,347.51m 0m] [234.97m -79.40m 0m]	X	
	(10%,45%,45%)	[-208.09m 1537.21m -369.88m 0m]	X	Default

		[-422.42m -344.21m 0m] [-369.88m 1537.21m -208.09m 0m] [-344.21m -422.42m 0m]	X	Operation Settings B + 2 hidden layers
	(30%,35%,35%)	[-931.03m 4272.94m -2333.96m 0m] [20.68m 265.88m 0m] [-2333.96m 4272.94m -931.03m 0m] [265.88m 20.68m 0m]	X X	
	(50%,25%,25%)	[-49.73m 1,068.10m -18.35m 0m] [33.96m 48.92m 0m] [-18.36m 1,068.10m -49.73m 0m] [48.92m 33.96m 0m]	X X	
	(70%,15%,15%) Default	[203.43m 164.18m 632.36m 0m] [57.94m 68.56m 0m] [632.36m 164.18m 203.43m 0m] [68.58m 57.94m 0m]	247.98m 111.14m	
	(80%,10%,10%)	[141.86m 341.28m 516.86m 0m] [150.07m 158.49m 0m] [516.86m 341.28m 141.86m 0m] [158.49m 150.07m 0m]	219.59m 72.58m	
	(90%,5%,5%)	[230.75m -42.17m 811.37m 0m] [274.11m 296.98m 0m] [811.37m 42.17m 230.75m 0m] [296.98m 274.11m 0m]	359.89m 250.80m	
	(98%,1%,1%)	[103.72m 576.04m 320.23m 0m] [-5.61m -2.81m 0m] [320.23m 576.04m 103.72m 0m] [-2.81m -5.61m 0m]	X X	
	(10%,45%,45%)	[170.90m 236.32m 595.01m 0m] [109.46m 66.63m 0m] [595.01m 236.32m 170.90m 0m] [66.63m 109.46m 0m]	235.09m 85.37m	Default Operation Settings B + 3 hidden layers
	(30%,35%,35%)	[139.00m 418.08m 442.87m 0m] [249.27m 267.46m 0m] [442.87m 418.08m 139.00m 0m] [267.46m 249.27m 0m]	224.94m 125.16m	
	(50%,25%,25%)	[158.62m 351.08m 491.39m 0m] [2.35m -30.28m 0m] [491.39m 351.08m 158.62m 0m] [-30.28m 2.35m 0m]	X X	
	(70%,15%,15%) Default	[148.53m 385.22m 466.25m 0m] [0.04m -2.27m 0m] [466.25m 385.22m 148.53m 0m] [-2.27m 0.04m 0m]	192.92m X	
	(80%,10%,10%)	[56.77m 785.41m 198.24m 0m] [141.69m 166.25m 0m]	235.27m	

		[198.24m 785.41m 56.77m 0m] [166.25m 141.69m 0m]	197.24m	
	(90%,5%,5%)	[-166.96m 1,787.74m -620.55m 0m] [-45.93m -75.84m 0m] [-620.55m 1,787.74m -166.96m 0m] [-75.84m -45.93m 0m]	X X	
	(98%,1%,1%)	[-33.60m 1,048.41m -16.66m 0m] [67.84m 120.55m 0m] [-16.66m 1,048.41m -33.60m 0m] [120.55m 67.84m 0m]	X X	
	(10%,45%,45%)	[143.64m 1,242.46m 953.47m 0m] [409.94m 157.46m 0m] [953.47m 1,242.46m 143.64m 0m] [157.46m 409.94m 0m]	495.18m 394.39m	Default Operation Settings B + 4 hidden layers
	(30%,35%,35%)	[-756.93m 3,263.07m -1,415.99m 0m] [191.40m 102.91m 0m] [-1,415.99m 3,263.07m -756.93m 0m] [102.91m 191.40m 0m]	X X	
	(50%,25%,25%)	[-219.37m 1,876.11m -564.73m 0m] [10.04m 16.53m 0m] [-564.73m 1,876.11m -219.37m 0m] [16.53m 10.04m 0m]	X X	
	(70%,15%,15%) Default	[1,555.73m -5,874.29m 5,315.56m 0m] [-169.42m -186.57m 0m] [5,315.55m 5,874.29m 1,555.73m 0m] [-186.57m -169.42m 0m]	X X	
	(80%,10%,10%)	[116.03m 580.39m 304.44m 0m] [-5.09m -5.56m 0m] [304.44m 580.39m 116.03m 0m] [-5.56m -5.09m 0m]	X X	
	(90%,5%,5%)	[5,533.40m -23,793.42m 19,254.14m 0m] [-1,097.74m -1,112.27m 0m] [19,254.14m -23,793.42m 5,533.40m 0m] [-1,112.27m -1,097.74m 0m]	X X	
	(98%,1%,1%)	[227.72m 381.73m 409.35m 0m] [113.07m 117.73m 0m] [409.35m 381.73m 227.72m 0m] [117.73m 113.07m 0m]	162.90m 75.66m	
	(10%,45%,45%)	[8.37m 220.28m 400.72m 0m] [134.44m 206.89m 0m] [400.72m 220.28m 8.37m 0m] [206.89m 134.44m 0m]	242.11m 113.80m	Default Operation Settings B + 5 hidden layers
	(30%,35%,35%)	[1,126.70m -5,642.68m 5,510.10m 0m] [170.50m -282.24m 0m] [5,510.10m -5,642.68m 1,126.70m 0m] [-282.24m 170.50m 0m]	X X	

	(50%,25%,25%)	[418.23m -581.91m 1,160.68m 0m] [85.18m 26.28m 0m] [1,160.68m -581.91m 418.23m 0m] [26.28m 85.18m 0m]	X X	
	(70%,15%,15%) Default	[2,288.45m 8,429.98m 7,134.97m 0m] [565.12m 578.81m 0m] [7,134.97m -8,429.98m 2,288.45m 0m] [578.81m 565.12m 0m]	X X	
	(80%,10%,10%)	[1,469.42m -6,012.17m 5,547.10m 0m] [138.33m 269.54m 0m] [5,547.10m -6,012.17m 1,469.42m 0m] [269.54m 138.33m 0m]	X X	
	(90%,5%,5%)	[99.39m 1,255.15m -354.41m 0m] [240.46m -91.46m 0m] [-354.41m 1,255.15m 99.39m 0m] [-91.46m 240.46m 0m]	X X	
	(98%,1%,1%)	[-560.38m 2,964.91m -1,265.14m 0m] [134.73m 358.45m 0m] [-1,265.14m 2,964.91m -560.38m 0m] [358.45m 134.73m 0m]	X X	

Table 10
Distribution and Branch Line Length Approximations of NNIM-LLA for the Rural Case, Default Operation Settings B and Different Participation Percentage Values and Hidden Layers (the symmetrical approximations are reported in blue font color)

Indicative OV LV BPL Topologies of Table 1	**Participation Percentages for Training, Validation and Testing (%,%,%)**	**Rural case**	**RMSD**	**Notes**
Distribution Line Length L =[L_1 L_2 0 0] **Branch Line Length** $\mathbf{L}_\mathrm{b}$ =[L_{b1} 0 0]		[600m 400m 0m 0m] [300m 0m 0m]	-	-
NNIM-LLA **Approximated Distribution Line Length** $\mathbf{L}_{\mathrm{NNIM-LLA}}$ = [$L_{1,\mathrm{NNIM-LLA}}$ $L_{2,\mathrm{NNIM-LLA}}$ 0 0] **Approximated Branch Line Length** $\mathbf{L}_{\mathrm{b,NNIM-LLA}}$ = [$L_{\mathrm{b1,NNIM-LLA}}$ 0 0]	(10%,45%,45%)	[311.08m 696.43m 0m 0m] [175.45m 0m 0m] [696.43m 311.08m 0m 0m] [175.45m 0m 0m]	163.38m 68.37m	Default Operation Settings B + 1 hidden layer
	(30%,35%,35%)	[119.77m 904.53m 0m 0m] [44.00m 0m 0m] [904.53m 119.77m 0m 0m] [44.00m 0m 0m]	280.48m 183.92m	
	(50%,25%,25%)	[194.44m 806.07m 0m 0m] [93.66m 0m 0m] [806.07m 194.44m 0m 0m] [93.66m 0m 0m]	230.51m 134.85m	
	(70%,15%,15%) Default	[265.66m 866.04m 0m 0m] [156.07m 0m 0m] [866.04m 265.66m 0m 0m]	223.51m 125.09m	

		[156.07m 0m 0m]		
	(80%,10%,10%)	[257.40m 742.60m 0m 0m] [200.81m 0m 0m] [742.60m 257.40m 0m 0m] [200.81m 0m 0m]	186.92m 84.94m	
	(90%,5%,5%)	[220.80m 824.57m 0m 0m] [170.62m 0m 0m] [824.57m 220.80m 0m 0m] [170.62m 0m 0m]	220.65m 119.09m	
	(98%,1%,1%)	[187.47m 812.53m 0m 0m] [171.92m 0m 0m] [812.53m 187.47m 0m 0m] [171.92m 0m 0m]	225.76m 123.48m	
	(10%,45%,45%)	[248.28m 748.62m 0m 0m] [183.84m 0m 0m] [748.62m 248.28m 0m 0m] [183.84m 0m 0m]	192.26m 91.50m	Default Operation Settings B + 2 hidden layers
	(30%,35%,35%)	[297.78m 899.66m 0m 0m] [81.95m 0m 0m] [899.66m 297.78m 0m 0m] [81.95m 0m 0m]	235.60m 145.30m	
	(50%,25%,25%)	[252.84m 665.95m 0m 0m] [180.89m 0m 0m] [665.95m 252.84m 0m 0m] [180.89m 0m 0m]	171.31m 75.77m	
	(70%,15%,15%) Default	[247.53m 772.84m 0m 0m] [215.07m 0m 0m] [772.84m 247.53m 0m 0m] [215.07m 0m 0m]	196.56m 92.84m	
	(80%,10%,10%)	[255.63m 742.63m 0m 0m] [302.62m 0m 0m] [742.63m 255.63m 0m 0m] [302.62m 0m 0m]	183.61m 76.71m	
	(90%,5%,5%)	[215.75m 795.23m 0m 0m] [266.35m 0m 0m] [795.23m 215.75m 0m 0m] [266.35m 0m 0m]	208.73m 102.26m	
	(98%,1%,1%)	[208.65m 791.35m 0m 0m] [279.41m 0m 0m] [791.35m 208.65m 0m 0m] [279.41m 0m 0m]	209.33m 102.58m	
	(10%,45%,45%)	[250.39m 799.33m 0m 0m] [172.89m 0m 0m] [799.33m 250.39m 0m 0m] [172.89m 0m 0m]	206.28m 105.74m	Default Operation Settings B +

	(30%,35%,35%)	[242.37m 714.46m 0m 0m] [183.29m 0m 0m] [714.46m 242.37m 0m 0m] [183.29m 0m 0m]	185.32m 85.83m	3 hidden layers
	(50%,25%,25%)	[99.70m 900.25m 0m 0m] [299.56m 0m 0m] [900.25m 99.70m 0m 0m] [299.56m 0m 0m]	267.41m 160.50m	
	(70%,15%,15%) Default	[216.21m 784.78m 0m 0m] [160.92m 0m 0m] [784.78m 216.21m 0m 0m] [160.92m 0m 0m]	212.03m 111.65m	
	(80%,10%,10%)	[220m 780m 0m 0m] [300m 0m 0m] [780m 220m 0m 0m] [300m 0m 0m]	203.12m 96.21m	
	(90%,5%,5%)	[218.74m 767.11m 0m 0m] [251.74m 0m 0m] [767.11m 218.74m 0m 0m] [251.74m 0m 0m]	200.88m 94.95m	
	(98%,1%,1%)	[220m 780m 0m 0m] [300m 0m 0m] [780m 220m 0m om] [300m 0m 0m]	203.12m 96.21m	
	(10%,45%,45%)	[81.83m 869.35m 0m 0m] [294.75m 0m 0m] [869.35m 81.83m 0m 0m] [294.75m 0m 0m]	264.26m 157.58m	Default Operation Settings B + 4 hidden layers
	(30%,35%,35%)	[336.45m 745.92m 0m 0m] [214.26m 0m 0m] [745.92m 336.45m 0m 0m] [214.26m 0m 0m]	167.53m 68.33m	
	(50%,25%,25%)	[148.85m 912.52m 0m 0m] [36.01m 0m 0m] [912.52m 148.85m 0m 0m] [36.01m 0m 0m]	276.69m 181.44m	
	(70%,15%,15%) Default	[233.58m 728.75m 0m 0m] [274.36m 0m 0m] [728.75m 233.58m 0m 0m] [274.36m 0m 0m]	186.32m 80.11m	
	(80%,10%,10%)	[186.30m 827.32m 0m 0m] [279.94m 0m 0m] [827.32m 186.30m 0m 0m] [279.94m 0m 0m]	224.93m 118.17m	
	(90%,5%,5%)	[220m 780m 0m 0m] [300m 0m 0m]	203.12m	

		[780m 220m 0m 0m] [300m 0m 0m]	96.21m	
	(98%,1%,1%)	[220m 780m 0m 0m] [300m 0m 0m] [780m 220m 0m om] [300m 0m 0m]	203.12m 96.21m	
	(10%,45%,45%)	[180.87m 632.44m 0m 0m] [88.01m 0m 0m] [632.44m 180.87m 0m 0m] [88.01m 0m 0m]	198.08m 115.89m	Default Operation Settings B + 5 hidden layers
	(30%,35%,35%)	[424.35m 860.32m 0m 0m] [268.28m 0m 0m] [860.32m 424.35m 0m 0m] [268.28m 0m 0m]	186.61m 99.55m	
	(50%,25%,25%)	[199.88m 800.01m 0m 0m] [300.00m 0m 0m] [800.01m 199.89m 0m 0m] [300.00m 0m 0m]	213.84m 106.94m	
	(70%,15%,15%) Default	[50m 950m 0m 0m] [300m 0m 0m] [950m 50m 0m 0m] [300m 0m 0m]	293.99m 187.08m	
	(80%,10%,10%)	[259.42m 753.73m 0m 0m] [285.93m 0m 0m] [753.73 259.42m 0m 0m] [285.93m 0m 0m]	185.67m 78.92m	
	(90%,5%,5%)	[229.20m 935.03m 0m 0m] [260.65m 0m 0m] [935.03m 229.20m 0m 0m] [260.65m 0m 0m]	246.49m 142.91m	
	(98%,1%,1%)	[220m 780m 0m 0m] [300m 0m 0m] [780m 220m 0m om] [300m 0m 0m]	203.12m 96.21m	

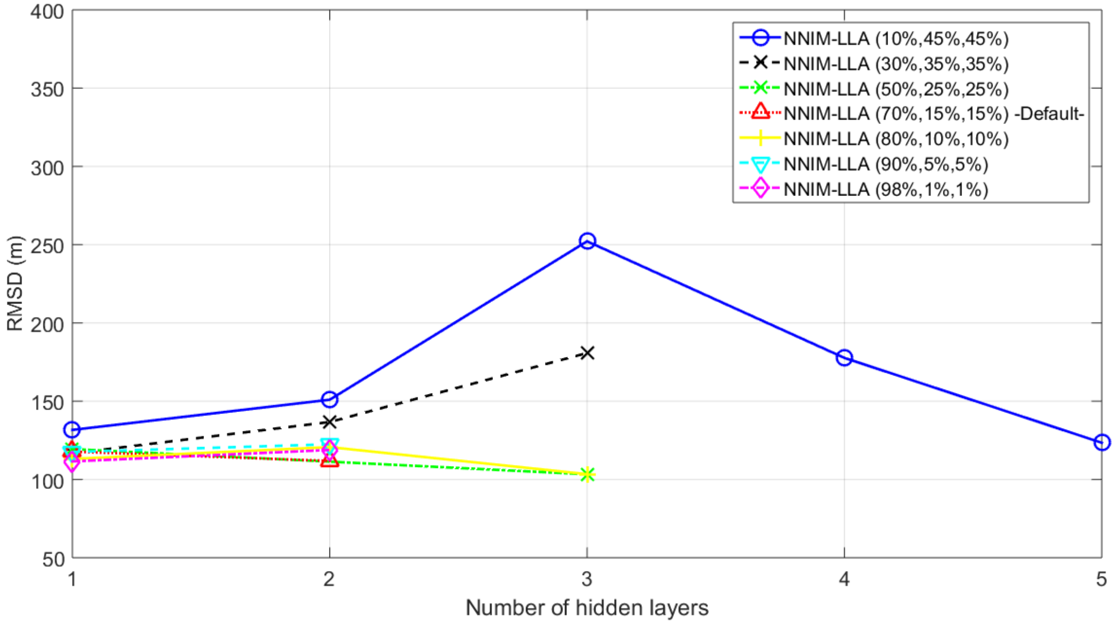

Figure 5. The best approximation RMSDs of NNIM-LLA for the urban case A for different participation percentages of training, validation and testing when the remaining default operation settings B are assumed.

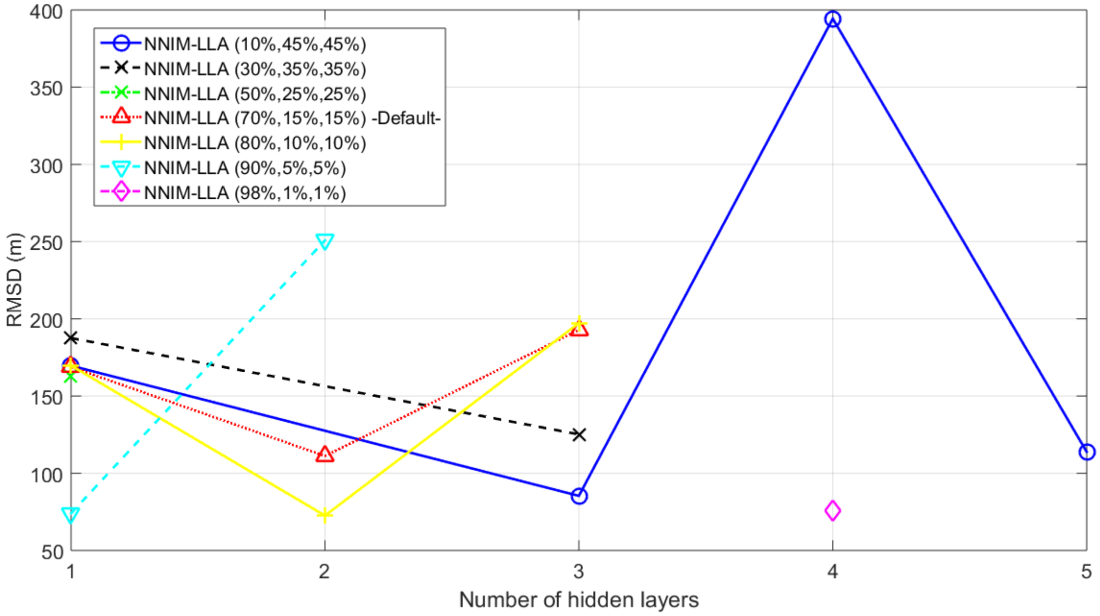

Figure 6. The best approximation RMSDs of NNIM-LLA for the suburban case for different participation percentages for training, validation and testing when the remaining default operation settings B are assumed.

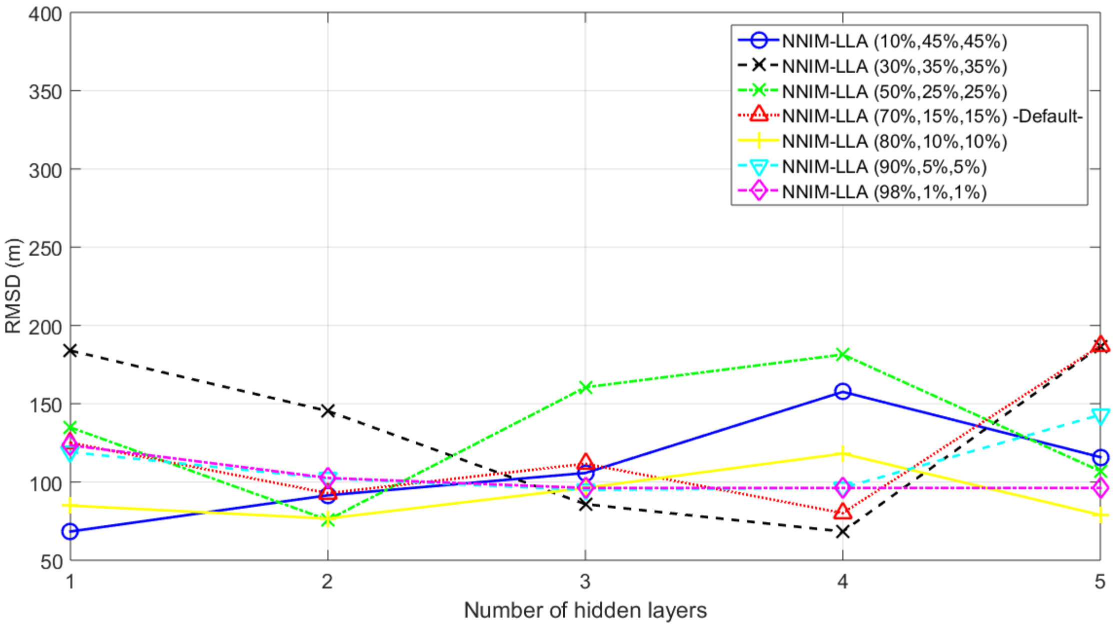

Figure 7. The best approximation RMSDs of NNIM-LLA for the rural case for different participation percentages for training, validation and testing when the remaining default operation settings B are assumed.

For the analysis of the NNIM-LLA approximations when different participation percentages of the three phases are applied, a balanced ratio among the participation percentages is here promoted for achieving lower RMSDs with an emphasis on the training participation percentage. In total, the default set (70%, 15%, 15%) of participation percentages in the operation settings B allows NNIM-LLA to satisfactorily approximate the distribution and branch line lengths of all the indicative OV LV BPL topologies of Table 1. Note that the RMSD of the default set of participation percentages is almost equal to the minimum RMSD in urban case A and rural case whilst the RMSD of the default set of participation percentages remains close to the minimum RMSD in suburban case.

4.4 TIM-LLA and NNIM-LLA Performance during the Default Operation Settings B and Possible Improvements

In this subsection, a briefing of the previous TIM-LLA and NNIM-LLA performance results is attempted so that the overall numerical performance comparison between these two proposed methods may become easy when the default operation settings B are assumed (see Sec. 4.1). In addition, the possible performance improvements, which may occur for the various *R* values of TIM-LLA presented in Sec. 4.2 and the different participation percentages of the three phases of NNIM-LLA presented in Sec. 4.3, are also presented.

In Table 11, the minimum RMSDs and the corresponding distribution and branch line length approximations of TIM-LLA and NNIM-LLA are reported with reference to Table 2 and Figure 1 for the urban case A when the default operation settings B are assumed. To examine the possible TIM-LLA performance improvement, the minimum RMSD, the difference between the minimum RMSDs of the default operation settings B and of the improvement action, the corresponding distribution and branch line length approximation and the corresponding *R* value of TIM-LLA are also presented in Table 11 with reference to Table 5 and Figure 4 for the various *R* values of TIM-LLA of Sec. 4.2. To examine the possible NNIM-LLA performance improvement, the minimum RMSD, the difference between the minimum RMSDs of the default operation settings B and of the improvement action, the corresponding distribution and branch line length approximation, the corresponding set of participation percentages of the three phases of NNIM-LLA and the corresponding number of hidden layers are also reported in Table 11 with reference to Table 8 and Figure 5 for the various sets of participation percentages and number of hidden layers of NNIM-LLA of Sec. 4.3. Of course, the real distribution and branch line lengths of the urban case A of Table 1 are also provided for comparison reasons. In Tables 12 and 13, same Tables with Table 11 are demonstrated but for the suburban and rural case, respectively.

Some final thoughts and observations can be outlined for the performance of TIM-LLA and NNIM-LLA by observing Tables 11-13:

- The difference values between the minimum RMSDs of the default operation settings B and of the previous improvement actions reveal the nature of TIM-LLA and NNIM-LLA; say:
    - TIM-LLA is a deterministic methodology and for that reason the RMSD differences remain marginal ranging from 0 to -13.12m (or -7.77%). Note that only negative RMSD differences are expected since the TIM OV LV BPL topology database is the operation basis of the deterministic concept of TIM-LLA and only improvement may occur.
    - NNIM-LLA is a stochastic methodology where AI, machine learning and neural networks coexist and for that reason the RMSD differences remain mixed and significant ranging from +15.63m (+17.83%) to -38.56m (-34.69%). Due to the simulation process of NNIM-LLA, positive RMSD differences can be observed and the values of the minimum RMSD depend on the simulation process.

  In general, TIM-LLA is a deterministic methodology with a steady and rather predictable performance behavior whereas NNIM-LLA is a stochastic methodology that may achieve better performances in comparison with the TIM-LLA one but a lot of settings are required to be further investigated prior to the NNIM-LLA operation in each BPL topology (*e.g.*, number of hidden layers, number of executions, participation percentages of its three phases). Similarly to [1], TIM-LLA and NNIM-LLA present advantages and disadvantages concerning their application towards the tomography of the OV LV BPL topologies while their performances can be considered to be comparable.

Table 11
Best Distribution and Branch Line Length Approximations of TIM-LLA and NNIM-LLA for the Urban Case A (Default Operation Settings B and Possible Improvements)

Indicative OV LV BPL Topologies of Table 1	**Urban case A** **(Typical urban case)**		**RMSD** **(m)** **RMSD Difference** **(m, %)**	**Notes**
Distribution Line Length L =$[L_1 \quad L_2 \quad L_3 \quad L_4]$ **Branch Line Length** $\mathbf{L_b}$ =$[L_{b1} \quad L_{b2} \quad L_{b3}]$	[500m 200m 100m 200m] [8m 13m 10m]		-	-
TIM-LLA (Default) **Approximated Distribution Line Length** $\mathbf{L}_{\mathrm{TIM-LLA}} =$ $[L_{1,\mathrm{TIM-LLA}} \quad L_{2,\mathrm{TIM-LLA}} \quad L_{3,\mathrm{TIM-LLA}} \quad L_{4,\mathrm{TIM-LLA}}]$ **(Approximated Branch Line Length)** $\mathbf{L}_{\mathrm{b,TIM-LLA}} =$ $[L_{\mathrm{b1,TIM-LLA}} \quad L_{\mathrm{b2,TIM-LLA}} \quad L_{\mathrm{b3,TIM-LLA}}]$	[640m 80m 80m 200m] [160m 0m 80m]		94.55m	Default Operation Settings B
NNIM-LLA (Default) **Approximated Distribution Line Length** $\mathbf{L}_{\mathrm{NNIM-LLA}} =$ $[L_{1,\mathrm{NNIM-LLA}} \quad L_{2,\mathrm{NNIM-LLA}} \quad L_{3,\mathrm{NNIM-LLA}} \quad L_{4,\mathrm{NNIM-LLA}}]$ **Approximated Branch Line Length** $\mathbf{L}_{\mathrm{b,NNIM-LLA}} =$ $[L_{\mathrm{b1,NNIM-LLA}} \quad L_{\mathrm{b2,NNIM-LLA}} \quad L_{\mathrm{b3,NNIM-LLA}}]$	3 hidden layers	[559.97m 184.02m 29.39m 226.51m] [126.66m 137.30m 131.44m]	87.68m	Default Operation Settings B
TIM-LLA (Improvement Action) **Approximated Distribution Line Length** $\mathbf{L}_{\mathrm{TIM-LLA}} =$ $[L_{1,\mathrm{TIM-LLA}} \quad L_{2,\mathrm{TIM-LLA}} \quad L_{3,\mathrm{TIM-LLA}} \quad L_{4,\mathrm{TIM-LLA}}]$ **(Approximated Branch Line Length)** $\mathbf{L}_{\mathrm{b,TIM-LLA}} =$ $[L_{\mathrm{b1,TIM-LLA}} \quad L_{\mathrm{b2,TIM-LLA}} \quad L_{\mathrm{b3,TIM-LLA}}]$	[633.33m 66.67m 66.67m 233.33m] [133.33m 0m 66.67m]		90.13m -4.42m (-4.67%)	R=3 + Default Operation Settings B
NNIM-LLA (Improvement Action) **Approximated Distribution Line Length** $\mathbf{L}_{\mathrm{NNIM-LLA}} =$ $[L_{1,\mathrm{NNIM-LLA}} \quad L_{2,\mathrm{NNIM-LLA}} \quad L_{3,\mathrm{NNIM-LLA}} \quad L_{4,\mathrm{NNIM-LLA}}]$ **Approximated Branch Line Length** $\mathbf{L}_{\mathrm{b,NNIM-LLA}} =$ $[L_{\mathrm{b1,NNIM-LLA}} \quad L_{\mathrm{b2,NNIM-LLA}} \quad L_{\mathrm{b3,NNIM-LLA}}]$	3 hidden layers	[668.38m 85.22m 51.72m 194.67m] [102.01m 121.44m 111.15m]	103.31m +15.63m (+17.83%)	(50%,25%,25%) + Default Operation Settings B

Table 12
Best Distribution and Branch Line Length Approximations of TIM-LLA and NNIM-LLA for the Suburban Case (Default Operation Settings B and Possible Improvements)

Indicative OV LV BPL Topologies of Table 1	**Suburban case**		**RMSD** **(m)** **RMSD Difference** **(m, %)**	**Notes**
Distribution Line Length L =$[L_1 \quad L_2 \quad L_3 \quad 0]$ **Branch Line Length** $\mathbf{L_b}$ =$[L_{b1} \quad L_{b2} \quad 0]$	[500m 400m 100m 0m] [50m 10m 0m]		-	-
TIM-LLA (Default) **Approximated Distribution Line Length** $\mathbf{L}_{\mathrm{TIM-LLA}} =$ $[L_{1,\mathrm{TIM-LLA}} \quad L_{2,\mathrm{TIM-LLA}} \quad L_{3,\mathrm{TIM-LLA}} \quad 0]$ **(Approximated Branch Line Length)** $\mathbf{L}_{\mathrm{b,TIM-LLA}} =$ $[L_{\mathrm{b1,TIM-LLA}} \quad L_{\mathrm{b2,TIM-LLA}} \quad 0]$	[780m 100m 120m 0m] [140m 160m 0m]		168.78m	Default Operation Settings B
NNIM-LLA (Default) **Approximated Distribution Line Length** $\mathbf{L}_{\mathrm{NNIM-LLA}} =$ $[L_{1,\mathrm{NNIM-LLA}} \quad L_{2,\mathrm{NNIM-LLA}} \quad L_{3,\mathrm{NNIM-LLA}} \quad 0]$ **Approximated Branch Line Length** $\mathbf{L}_{\mathrm{b,NNIM-LLA}} =$	2 hidden layers	[632.36m 164.18m 203.43m 0m] [68.58m 57.94m 0m]	111.14m	Default Operation Settings B

$[L_{\mathrm{b1,NNIM-LLA}}\quad L_{\mathrm{b2,NNIM-LLA}}\quad 0]$				
TIM-LLA (Improvement Action) **Approximated Distribution Line Length** $\mathbf{L}_{\mathrm{TIM-LLA}} = [L_{1,\mathrm{TIM-LLA}}\quad L_{2,\mathrm{TIM-LLA}}\quad L_{3,\mathrm{TIM-LLA}}\quad L_{4,\mathrm{TIM-LLA}}]$ **(Approximated Branch Line Length)** $\mathbf{L}_{\mathrm{b,TIM-LLA}} = [L_{\mathrm{b1,TIM-LLA}}\quad L_{\mathrm{b2,TIM-LLA}}\quad L_{\mathrm{b3,TIM-LLA}}]$	[700m 100m 200m 0m] [150m 150m 0m]		155.66m -13.12m (-7.77%)	*R*=10 + Default Operation Settings B
NNIM-LLA (Improvement Action) **Approximated Distribution Line Length** $\mathbf{L}_{\mathrm{NNIM-LLA}} = [L_{1,\mathrm{NNIM-LLA}}\quad L_{2,\mathrm{NNIM-LLA}}\quad L_{3,\mathrm{NNIM-LLA}}\quad L_{4,\mathrm{NNIM-LLA}}]$ **Approximated Branch Line Length** $\mathbf{L}_{\mathrm{b,NNIM-LLA}} = [L_{\mathrm{b1,NNIM-LLA}}\quad L_{\mathrm{b2,NNIM-LLA}}\quad L_{\mathrm{b3,NNIM-LLA}}]$	2 hidden layers	[516.86m 341.28m 141.86m 0m] [158.49m 150.07m 0m]	72.58m -38.56m (-34.69%)	(80%,10%,10%) + Default Operation Settings B

Table 13
Best Distribution and Branch Line Length Approximations of TIM-LLA and NNIM-LLA for the Rural Case (Default Operation Settings B and Possible Improvements)

Indicative OV LV BPL Topologies of Table 1	**Rural case**		**RMSD (m)** **RMSD Difference (m, %)**	**Notes**
Distribution Line Length L $=[L_1\quad L_2\quad 0\quad 0]$ **Branch Line Length** $\mathbf{L}_{\mathrm{b}} = [L_{\mathrm{b1}}\quad 0\quad 0]$	[600m 400m 0m 0m] [300m 0m 0m]		-	-
TIM-LLA (Default) **Approximated Distribution Line Length** $\mathbf{L}_{\mathrm{TIM-LLA}} = [L_{1,\mathrm{TIM-LLA}}\quad L_{2,\mathrm{TIM-LLA}}\quad 0\quad 0]$ **(Approximated Branch Line Length)** $\mathbf{L}_{\mathrm{b,TIM-LLA}} = [L_{\mathrm{b1,TIM-LLA}}\quad 0\quad 0]$	[780m 220m 0m 0m] [300m 0m 0m]		96.21m	Default Operation Settings B
NNIM-LLA (Default) **Approximated Distribution Line Length** $\mathbf{L}_{\mathrm{NNIM-LLA}} = [L_{1,\mathrm{NNIM-LLA}}\quad L_{2,\mathrm{NNIM-LLA}}\quad 0\quad 0]$ **Approximated Branch Line Length** $\mathbf{L}_{\mathrm{b,NNIM-LLA}} = [L_{\mathrm{b1,NNIM-LLA}}\quad 0\quad 0]$	1 hidden layer	[733.33m 266.67m 0m 0m] [233.33m 0m 0m]	75.59m	Default Operation Settings B
TIM-LLA (Improvement Action) **Approximated Distribution Line Length** $\mathbf{L}_{\mathrm{TIM-LLA}} = [L_{1,\mathrm{TIM-LLA}}\quad L_{2,\mathrm{TIM-LLA}}\quad L_{3,\mathrm{TIM-LLA}}\quad L_{4,\mathrm{TIM-LLA}}]$ **(Approximated Branch Line Length)** $\mathbf{L}_{\mathrm{b,TIM-LLA}} = [L_{\mathrm{b1,TIM-LLA}}\quad L_{\mathrm{b2,TIM-LLA}}\quad L_{\mathrm{b3,TIM-LLA}}]$	[780m 220m 0m 0m] [300m 0m 0m]		96.21m 0m (0%)	*R*=5 + Default Operation Settings B
NNIM-LLA (Improvement Action) **Approximated Distribution Line Length** $\mathbf{L}_{\mathrm{NNIM-LLA}} = [L_{1,\mathrm{NNIM-LLA}}\quad L_{2,\mathrm{NNIM-LLA}}\quad L_{3,\mathrm{NNIM-LLA}}\quad L_{4,\mathrm{NNIM-LLA}}]$ **Approximated Branch Line Length** $\mathbf{L}_{\mathrm{b,NNIM-LLA}} = [L_{\mathrm{b1,NNIM-LLA}}\quad L_{\mathrm{b2,NNIM-LLA}}\quad L_{\mathrm{b3,NNIM-LLA}}]$	4 hidden layers	[745.92m 336.45m 0m 0m] [214.26m 0m 0m]	68.33m -7.26m (-9.60%)	(30%,35%,35%) + Default Operation Settings B

- The approximated OV LV BPL topologies by TIM-LLA and NNIM-LLA that have been reported in Tables 11-13 are those between the corresponding original and symmetrical approximated ones that have the best RMSD in each case. In real life, the selection between the original and the symmetrical approximated OV LV BPL topologies by TIM-LLA and NNIM-LLA requires any additional topological pieces of information or empirical observations so that the distinction between these approximated OV LV BPL topologies can be feasible in each case (*e.g.,* any distribution or branch line length information can be useful).
- With reference to [1], the representativeness attribute and the accuracy degree of the TIM OV LV BPL topology database had a significant impact on the performance of TIM-BNI and NNIM-BNI. In this paper, the representative sets of the TIM OV LV BPL topology database have been adopted by default during the preparation of the default operation settings B; say, only the OV LV BPL topologies with the same number of branches with the examined one are considered from the TIM OV LV BPL topology database in each approximation of the TIM-LLA and NNIM-LLA. As the accuracy degree of the TIM OV LV BPL topology database is concerned, the following modifications have been made in default operation settings B in comparison with the default operation settings A, namely:
    - The length spacing for branch distance is equal to 100m and remains the same between the default operation settings A and B. Also, the length between the transmitting and receiving ends of all the OV LV BPL topologies remains the same for the default operation settings A and B and is assumed to be equal to 1000m;
    - To better approximate OV LV BPL topologies of larger branches (*e.g.,* rural case of Table 1), the length spacing for branch length is assumed to be equal to 100m while the branch line length may range from 0m to 300m in default operation settings B. The respective values are equal to 25m and 0m-100m in default operation settings A and B. However, the higher length spacing for branch length has a negative impact on the approximation of the short branches thus creating higher RMSDs.
    - In default operation settings B, the frequency range and the flat-fading subchannel frequency spacing are assumed to be equal to 3-88MHz and 1MHz, respectively. During the preparation of the default operation settings B, more frequencies are used per coupling scheme channel transfer function for the examined OV LV BPL topologies so as to facilitate the operation of TIM-LLA and NNIM-LLA. In fact, the frequency range had been assumed equal to 3-30MHz while the flat-fading subchannel frequency spacing had been equal to 1MHz in operation settings A of [1].

  Here, it should be reminded that there is a trade-off relationship between the accuracy degree of the TIM OV LV BPL topology database and the execution time of TIM-LLA and NNIM-LLA. For the previous reason, a compromise between the accuracy and the execution time is made either in this extension paper or in [1] during the preparation of the corresponding default operation settings. In fact, the aforementioned trade-off relationship is stronger in this extension paper since the tomography requirements have been proved to be higher in comparison with the ones during the branch number identification of [1].

Already been mentioned in [1], on the basis of the factors that affect the accuracy degree of the TIM OV LV BPL topology database, the impact of lower values of the length spacing L_s for both branch distance and branch length and of higher values of the maximum branch length $L_{b,max}$ during the preparation of the TIM OV LV BPL topology database on the approximation performance of TIM-LLA and NNIM-LLA is a subject of future research.

5. Conclusions

In this extension paper, the distribution and branch line length approximation methods of TIM-LLA and NNIM-LLA have been proposed as extensions of the respective TIM-BNI and NNIM-BNI of [1] while the factors that affect their approximation performance have been recognized and benchmarked. Learning from the good practices of [1] concerning the factors that affect the preparation of the TIM OV LV BPL topology database, the accuracy degree and the representativeness of the TIM OV LV BPL topology database have been taken into account during the preparation of the default operation settings B of this paper thus having improved RMSD values of the distribution and branch line length approximations of both TIM-LLA and NNIM-LLA by default. As the operation of TIM-LLA is concerned, it has been revealed that TIM-LLA is a deterministic methodology with a steady and rather predictable performance behavior in terms of the appeared RMSD differences. TIM-LLA better approximates the distribution and branch line lengths when the number of branches of the examined OV LV BPL topology remains high (i.e., urban case A). Also, satisfactory TIM-LLA approximations may occur when OV LV BPL topologies of 1 branch are examined (i.e., rural case). Learning from the good practice of [1] concerning the R value factor that affects the operation of the TIM OV LV BPL topology database, the assumption of the R value that was equal to 5 in the operation settings B has allowed TIM-LLA to decently approximate the distribution and branch line lengths of all the indicative OV LV BPL topologies. As the operation of NNIM-LLA is concerned, it has been revealed that NNIM-LLA is a stochastic methodology that may achieve better performances in comparison with the TIM-LLA one but a lot of settings are required to be investigated prior to the NNIM-LLA operation (i.e., number of hidden layers, number of executions, participation percentages of its three phases). Conversely to [1], a balanced ratio among the NNIM-LLA participation percentages has been highlighted in this extension paper for achieving lower RMSDs with a more emphasis on the training participation percentage. Anyway, mixed RMSD differences of significant range may occur since NNIM-LLA is based on simulations where AI, machine learning and neural networks coexist. Similarly to [1], the accuracy degree of the TIM OV LV BPL topology database again remains critical for the performance of TIM-LLA and NNIM-LLA thus promising significantly lower RMSDs for both approximation methods when higher accuracy degree is going to be adopted in exchange with higher execution times due to the preparation of the TIM OV LV BPL topology database. Especially, the approximation of the branch line length remains a more difficult task and demands significantly higher accuracy degrees in comparison with the approximation of the distribution line lengths and branch number identification. In the future research steps, TIM-LLA and NNIM-LLA are going to be further elaborated, expanded and cooperate in order to cope with the fervent tomography issues of the operation of the smart grid (e.g. fault identification, measurement noise mitigation).

CONFLICTS OF INTEREST

The authors declare that there is no conflict of interests regarding the publication of this paper.

References

[1] A. G. Lazaropoulos, "Information Technology, Artificial Intelligence and Machine Learning in Smart Grid – Performance Comparison between Topology Identification Methodology and Neural Network Identification Methodology for the Branch Number Approximation of Overhead Low-Voltage Broadband over Power Lines Network Topologies," *Trends in Renewable Energy*, *Trends in Renewable Energy*, vol. 7, no. 1, pp. 87-113, Oct. 2021. [Online]. Available: http://futureenergysp.com/index.php/tre/article/view/133

[2] G. Hallak, M. Berners, and A. Mengi, "Planning Tool for Fast Roll-Out of G. hn Broadband PLC in Smart Grid Networks: Evaluation and Field Results," *In 2021 IEEE International Symposium on Power Line Communications and its Applications (ISPLC)*, pp. 108-113, 2021.

[3] F. Aalamifar and L. Lampe, "Optimized WiMAX profile configuration for smart grid communications," *IEEE Transactions on Smart Grid*, vol. 8, no. 6, pp. 2723-2732, 2017.

[4] A. G. Lazaropoulos, "Wireless Sensor Network Design for Transmission Line Monitoring, Metering and Controlling Introducing Broadband over PowerLines-enhanced Network Model (BPLeNM)," *ISRN Power Engineering*, vol. 2014, Article ID 894628, 22 pages, 2014. doi:10.1155/2014/894628. [Online]. Available: http://www.hindawi.com/journals/isrn.power.engineering/2014/894628/

[5] M. H. Rehmani, M. Reisslein, A. Rachedi, M. Erol-Kantarci, and M. Radenkovic, "Integrating renewable energy resources into the smart grid: recent developments in information and communication technologies," *IEEE Transactions on Industrial Informatics*, vol. 14, no. 7, pp. 2814-2825, 2018.

[6] A. G. Lazaropoulos and H. C. Leligou, "Fiber Optics and Broadband Over Power Lines in Smart Grid: a Communications System Architecture for Overhead High-Voltage, Medium-Voltage and Low-Voltage Power Grids," *Progress in Electromagnetics Research B*, vol. 95, pp. 185-205, 2022. [Online]. Available: https://www.jpier.org/PIERB/pier.php?paper=22062502

[7] F. R. Yu, P. Zhang, W. Xiao, and P. Choudhury, "Communication systems for grid integration of renewable energy resources," *IEEE Network*, vol. 25, no. 5, pp. 22–29, Sep. 2011.

[8] B. Heile, "Smart grids for green communications [industry perspectives]," *IEEE Wireless Commun.*, vol. 17, no. 3, pp. 4–6, Jun. 2010.

[9] A. G. Lazaropoulos and P. G. Cottis, "Transmission characteristics of overhead medium voltage power line communication channels," *IEEE Trans. Power Del.*, vol. 24, no. 3, pp. 1164-1173, Jul. 2009.

[10] A. G. Lazaropoulos and P. G. Cottis, "Capacity of overhead medium voltage power line communication channels," *IEEE Trans. Power Del.*, vol. 25, no. 2, pp. 723-733, Apr. 2010.

[11] A. G. Lazaropoulos and P. G. Cottis, "Broadband transmission via underground medium-voltage power lines-Part I: transmission characteristics," *IEEE Trans. Power Del.*, vol. 25, no. 4, pp. 2414-2424, Oct. 2010.

[12] A. G. Lazaropoulos and P. G. Cottis, "Broadband transmission via underground medium-voltage power lines-Part II: capacity," *IEEE Trans. Power Del.*, vol. 25, no. 4, pp. 2425-2434, Oct. 2010.

[13] E. Biglieri, "Coding and modulation for a horrible channel," *IEEE Commun. Mag.*, vol. 41, no. 5, pp. 92–98, May 2003.

[14] M. Gebhardt, F. Weinmann, and K. Dostert, "Physical and regulatory constraints for communication over the power supply grid," *IEEE Commun. Mag.*, vol. 41, no. 5, pp. 84-90, May 2003.

[15] M. Götz, M. Rapp, and K. Dostert, "Power line channel characteristics and their effect on communication system design," *IEEE Commun. Mag.*, vol. 42, no. 4, pp. 78-86, Apr. 2004.

[16] A. G. Lazaropoulos, "Towards Modal Integration of Overhead and Underground Low-Voltage and Medium-Voltage Power Line Communication Channels in the Smart Grid Landscape: Model Expansion, Broadband Signal Transmission Characteristics, and Statistical Performance Metrics (Invited Paper)," *ISRN Signal Processing*, vol. 2012, Article ID 121628, pp. 1-17, 2012. [Online]. Available: http://www.hindawi.com/isrn/sp/2012/121628/

[17] F. Versolatto and A. M. Tonello, "An MTL theory approach for the simulation of MIMO power-line communication channels," *IEEE Trans. Power Del.*, vol. 26, no. 3, pp. 1710-1717, Jul. 2011.

[18] P. Amirshahi and M. Kavehrad, "High-frequency characteristics of overhead multiconductor power lines for broadband communications," *IEEE J. Sel. Areas Commun.*, vol. 24, no. 7, pp. 1292-1303, Jul. 2006.

[19] L. Stadelmeier, D. Schneider, D. Schill, A. Schwager, and J. Speidel, "MIMO for inhome power line communications," presented at the *Int. Conf. on Source and Channel Coding*, Ulm, Germany, Jan. 2008.

[20] T. Sartenaer, "Multiuser communications over frequency selective wired channels and applications to the powerline access network" *Ph.D. dissertation*, Univ. Catholique Louvain, Louvain-la-Neuve, Belgium, Sep. 2004.

[21] S. Galli and T. Banwell, "A deterministic frequency-domain model for the indoor power line transfer function," *IEEE J. Sel. Areas Commun.*, vol. 24, no. 7, pp. 1304-1316, Jul. 2006.

[22] S. Galli and T. Banwell, "A novel approach to accurate modeling of the indoor power line channel-Part II: Transfer function and channel properties," *IEEE Trans. Power Del.*, vol. 20, no. 3, pp. 1869-1878, Jul. 2005.

[23] A. Pérez, A. M. Sánchez, J. R. Regué, M. Ribó, R. Aquilué, P. Rodréguez-Cepeda, and F. J. Pajares, "Circuital and modal characterization of the power-line network in the PLC band," *IEEE Trans. Power Del.*, vol. 24, no. 3, pp. 1182-1189, Jul. 2009.

[24] T. Sartenaer and P. Delogne, "Deterministic modelling of the (Shielded) outdoor powerline channel based on the multiconductor transmission line equations," *IEEE J. Sel. Areas Commun.*, vol. 24, no. 7, pp. 1277-1291, Jul. 2006.

[25] T. Sartenaer and P. Delogne, "Powerline cables modelling for broadband communications," in Proc. *IEEE Int. Conf. Power Line Communications and Its Applications*, Malmö, Sweden, Apr. 2001, pp. 331-337.

[26] C. R. Paul, *Analysis of Multiconductor Transmission Lines*. New York: Wiley, 1994.

[27] H. Meng, S. Chen, Y. L. Guan, C. L. Law, P. L. So, E. Gunawan, and T. T. Lie, "Modeling of transfer characteristics for the broadband power line communication channel," *IEEE Trans. Power Del.*, vol. 19, no. 3, pp. 1057-1064, Jul. 2004.

[28] A. G. Lazaropoulos, "Statistical Broadband over Power Lines Channel Modeling – Part 1: The Theory of the Statistical Hybrid Model," *Progress in Electromagnetics Research C*, vol. 92, pp. 1-16, 2019. [Online]. Available: http://www.jpier.org/PIERC/pierc92/01.19012902.pdf

[29] A. G. Lazaropoulos, "Improvement of Power Systems Stability by Applying Topology Identification Methodology (TIM) and Fault and Instability Identification Methodology (FIIM)–Study of the Overhead Medium-Voltage Broadband over Power Lines (OV MV BPL) Networks Case," *Trends in Renewable Energy*, vol. 3, no. 2, pp. 102-128, Apr. 2017. [Online]. Available: http://futureenergysp.com/index.php/tre/article/view/34

[30] A. G. Lazaropoulos, "Measurement Differences, Faults and Instabilities in Intelligent Energy Systems–Part 1: Identification of Overhead High-Voltage Broadband over Power Lines Network Topologies by Applying Topology Identification Methodology (TIM)," *Trends in Renewable Energy*, vol. 2, no. 3, pp. 85-112, Oct. 2016. [Online]. Available: http://futureenergysp.com/index.php/tre/article/view/26/32

[31] A. G. Lazaropoulos, "Review and Progress towards the Capacity Boost of Overhead and Underground Medium-Voltage and Low-Voltage Broadband over Power Lines Networks: Cooperative Communications through Two- and Three-Hop Repeater Systems," *ISRN Electronics*, vol. 2013, Article ID 472190, pp. 1-19, 2013. [Online]. Available: http://www.hindawi.com/isrn/electronics/aip/472190/

[32] A. G. Lazaropoulos, "Statistical Channel Modeling of Overhead Low Voltage Broadband over Power Lines (OV LV BPL) Networks – Part 1: The Theory of Class Map Footprints of Real OV LV BPL Topologies, Branch Line Faults and Hook-Style Energy Thefts," *Trends in Renewable Energy*, vol. 6, no. 1, pp. 61-87, Mar. 2020. [Online]. Available: http://futureenergysp.com/index.php/tre/article/download/112/pdf

[33] A. G. Lazaropoulos, "Broadband Performance Metrics and Regression Approximations of the New Coupling Schemes for Distribution Broadband over Power Lines (BPL) Networks," *Trends in Renewable Energy*, vol. 4, no. 1, pp. 43-73, Jan. 2018. [Online]. Available: http://futureenergysp.com/index.php/tre/article/view/59/pdf

[34] A. G. Lazaropoulos, "New Coupling Schemes for Distribution Broadband over Power Lines (BPL) Networks," *Progress in Electromagnetics Research B*, vol. 71, pp. 39-54, 2016. [Online]. Available: http://www.jpier.org/PIERB/pierb71/02.16081503.pdf

[35] I. C. Demetriou, “An application of best $L1$ piecewise monotonic data approximation to signal restoration,” *IAENG International Journal of Applied Mathematics*, vol. 53, no. 4, pp. 226-232, 2013.

[36] I. C. Demetriou, “L1PMA: A Fortran 77 Package for Best L1 Piecewise Monotonic Data Smoothing,” *Computer Physics Communications*, vol. 151, no. 1, pp. 315-338, 2003.

[37] M. Ibnkahla, “Applications of neural networks to digital communications–a survey. Signal processing,” vol. 80, no. 7, pp. 1185-1215, 2020.

[38] D. Okoh, *Computer Neural Networks on MATLAB*. CreateSpace Independent Publishing Platform, 2016.

[39] Y. T. Ma, K. H. Liu, and Y. N. Guo, “Artificial neural network modeling approach to power-line communication multi-path channel," in *Proc. Int. Conf. Neural Netw. Signal Process*, Jun. 2008, pp. 229-232.

[40] R. Hecht-Nielsen, “Theory of the backpropagation neural network,” *Neural networks for perception. Academic Press*, pp. 65-93, 1992.

[41] D. Okoh, Neural Network Training Code (https://www.mathworks.com/matlabcentral/fileexchange/59362-neural-network-training-code), MATLAB Central File Exchange. Retrieved April 22, 2020.

[42] A. G. Lazaropoulos, “Special Cases during the Detection of the Hook Style Energy Theft in Overhead Low-Voltage Power Grids through HS-DET Method – Part 2: Different Measurement Differences, Feint “Smart” Hooks and Hook Interconnection Issues,” *Trends in Renewable Energy*, vol. 5, no. 1, pp. 90-116, Jan. 2019. [Online]. Available: http://futureenergysp.com/index.php/tre/article/view/83/pdf

[43] A. G. Lazaropoulos, “Deployment Concepts for Overhead High Voltage Broadband over Power Lines Connections with Two-Hop Repeater System: Capacity Countermeasures against Aggravated Topologies and High Noise Environments,” *Progress in Electromagnetics Research B*, vol. 44, pp. 283-307, 2012. [Online]. Available: http://www.jpier.org/PIERB/pierb44/13.12081104.pdf

Trends in Renewable Energy
OPEN ACCESS ISSN: 2376-2144
Peer-Reviewed Article futureenergysp.com/index.php/tre

Effects of Angstrom-Prescott and Hargreaves-Samani Coefficients on Climate Forcing and Solar PV Technology Selection in West Africa

Mfongang Erim Agbor[1], Sunday O. Udo[1], Igwe O. Ewona[1,2], Samuel Chukwujindu Nwokolo*[1], Julie C. Ogbulezie[1], Solomon Okechukwu Amadi[3], Utibe Akpan Billy[1]

1: Department of Physics, Faculty of Physical Sciences, University of Calabar, Nigeria
2: Department of Physics, Faculty of Physical Sciences, Cross River University of Science and technology, Nigeria
3: Department of Physics, Faculty of Physical Sciences, Alex Ekwueme Federal University, Ndufu-Alike, Nigeria

Received December 10, 2022; Accepted January 13, 2023; Published January 15, 2023

We evaluated and compared the performance of simulated Angström-Prescott (AP) and Hargreaves-Samani (HS) models on monthly and annual timescales using generalized datasets covering the entire West African region. The fitted AP model yielded more efficient parameters of a = 0.366 and b = 0.459, whereas the HS model produced a 0.216 coefficient based on an annual timescale, which is more suitable in the region compared to coefficients recommended by the Food and Agriculture Organization (FAO) (a = 0.25 and b = 0.5) and HS (0.17), respectively. Employing the FAO and HS recommended coefficients will introduce a relative percentage error (RPE) of 18.388% and 27.19% compared to the RPEs of 0.0014% and 0.1036% obtained in this study, respectively. When considering time and resource availability in the absence of ground-measured datasets, the coefficients obtained in this study can be used for predicting global solar radiation within the region. According to the AP and HS coefficients, the polycrystalline module (p-Si) is more reliable than the monocrystalline module (m-Si) because the p-Si module has a higher tendency to withstand the high temperatures projected to affect the region due to its higher intrinsic properties based on the AP and HS coefficients assessment in the region.

Keywords: Ångström-Prescott coefficient; Hargreaves-Samani coefficient; Global solar radiation; Solar PV technologies; Climate forcing

Introduction

It is undeniable that the growth of solar PV installed capacity in the past years has outpaced the most optimistic projections, as indicated by global cumulative installed capacity at the end of 2013 being only 9.2 MW and worldwide cumulative capacity at year-end 2014 being 15.6 GW [1]. The exponential trend of PV installation growth started in 2008, and the total capacity has doubled every year, with the longest period of increase (since 2009) in 2014, when global installed capacity reached 15.6 GW and year-end solar power share was estimated at 5% of global electricity generation in just 6 years

---

*Corresponding authors: henrilynnmfongang@gmail.com (Agbor M.E.); sam31628@gmail.com (Nwokolo S.C.)

Tr Ren Energy, 2023, Vol.9, No.1, 78-106. doi: 10.17737/tre.2023.9.1.00150

(period of 2000-2014), which indicates the steep growth rate in global cumulative installed capacity [1].

The reason for this rapid growth is that in just 6 years, the cost of PV electricity has gone down significantly, which is phenomenal as it was in the years 2007 to 2009 and 2012 to 2014, when global cumulative installed capacity grew by 71% (from 2.1 GW to 3.4 GW) and 47% (from 586 MW to 1.12 GW), respectively [1]. The global cumulative installed capacity of solar power was only 15.6 GW at year-end 2014, and the share of solar power in electricity generation was estimated at 5%. Solar power penetration grew from 20.9 GW in 2010 to 29.3 GW in 2014, with a CAGR (compound annual growth rate) of 60% for the six-year period of 2000-2014. Installed solar capacity in France and Germany amounted to 79 GW and 30 GW [1], respectively, due to a high construction cost and German government subsidies for PV power plants that are only given for the first 15 years of the plants, whereas PV power is available on the commercial grid in countries such as Italy, China, and India for a number of years.

The cost of solar energy is affected by a number of factors. The most important factor is the installation costs of PV cells, particularly photovoltaic modules. The issue of determining the optimal location for a PV power plant has seen a steady decline as the cost of solar cells, per watt, has dropped from $2.96/W in 1979 to $1.61/W in 2013 and is expected to drop to about $1/W by 2016. More than 30 countries in the world are adopting solar power as a part of their national energy mix. After years of investment and research, solar energy has become a reliable source of electricity worldwide, and PV modules are becoming more efficient, using less energy and costing less to produce.

Both of these conditions result in relatively low densities of data regarding incoming solar radiation at the ground level for global climatic information activities, especially at the local level in countries with a few stations in those countries that have started to monitor solar radiation. Satellite observations of solar radiation are more accurate and less expensive than terrestrial observations because they can make use of remote sensing instruments that determine the spectral composition and geographical distribution of incoming solar radiation. Consequently, the density of meteorological stations equipped for measuring solar radiation is too low for global coverage. For instance, there are over 3,000 stations worldwide measuring solar radiation, and in the rest of the world there is a density of about 10 stations per million people [2]. Additionally, a number of statistical problems have been identified, mainly in the field of quantifying solar radiation; for example, the variability of the measurement technique makes it difficult to use solar radiation data for selecting stations to form climatic networks. Finally, spectral solar radiation data on the horizontal and vertical distribution of solar radiation in space can be obtained with high precision, taking advantage of satellite measurements.

Michael FitzGerald has found an equation from the period between 1781 and 1860 that plots monthly mean global solar radiation (H) in all sky conditions on the horizontal axis versus H in clear skies (Hclear), which is S/So cited in Kimball [3]. Throughout the year, some astronomers believe that global solar radiation is closely related to or directly proportional to the duration of sunshine. However, others suggest that it is not directly related but that it changes in proportion to the strength of atmospheric transparency, according to the Global Precipitation Climatology Project (GPCP), an assessment of climate change conducted by NASA and other international organizations on the time of the Earth’s orbit about the sun.

FitzGerald's equation demonstrated that the relationship between monthly mean global solar radiation (H) and the duration of sunshine (S) varies from year to year and decade to decade between 1781 and 1860. FitzGerald found that there was a stable relationship between solar radiation and cloud cover. However, this was not the case in other periods during the nineteenth century. During the decade before 1840, there was an unstable relationship between solar radiation and cloud cover. The main results for this period show an increase in solar radiation because of an increase in global cloud cover and a decrease in solar radiation by changing the duration of sunshine from one decade to another. Therefore, we can say that FitzGerald's equation is only accurate for the last part of the nineteenth century.

Kimball [3] was the first to discover that FitzGerald's equation view of solar radiation in relation to sunlight is highly correlated with or directly proportional to the length of daylight. Angstrom [4] was the first to mathematically represent Kimball's idea. This was accomplished by relating the monthly mean global solar radiation (H) in all clear sky conditions (H_{clear}) to the fraction of sunlight duration (S/So). As a result, Angstrom [4] claims that the relation can be used to estimate H:

$$\frac{H}{Hclear} = 0.25 + 0.75\left(\frac{S}{So}\right) \quad (1)$$

The most recent version of the Angstrom-Prescott model (AP) replaces H with daily average extraterrestrial solar radiation parameters (Ho) which Prescott modified [5] and is expressed as:

$$\frac{H}{Ho} = 0.25 + 0.54\left(\frac{S}{So}\right) \quad (2)$$

Environmental variables such as cloud cover, relative humidity, wind, temperature, and precipitation regime can help modify the physical AP model. However, these factors vary between physical and environmental parameters, and their effect is difficult to quantify numerically.

The AP model was developed not only to expand energy applications in response to the need for adequate knowledge of available solar resources, but also to study numerous atmospheric physical parameters in which sunlight scattering, reflections, and diffractions influence the variation of AP coefficients in different parts of the world [6]. Paulescu *et al.* [7] identified two categories of algorithms for predicting solar energy using AP coefficients: (1) prediction of global solar irradiance under a clear sky; and (2) physical fit of clear sky estimates to the current sky state based on sunshine duration measurements.

The authors of this study identified additional aspects that the AP model coefficient could help us evaluate. The coefficient can be quantified for various solar PV technologies suitable for solar energy harvesting by analyzing the atmospheric dynamics of the sum of the AP coefficients (a+b) and taking into account that different solar PV modules have different degrees of ability to withstand extreme temperatures due to the inherent characteristics of the module's solar cell. Polycrystalline silicon (p-Si), for example, is more resistant to high temperatures than monocrystalline silicon (m-Si), activating the production of electricity in places with low temperatures induced by a higher percentage of diffuse components of solar radiation worldwide.

Thus, the amplitude of the AP coefficients (a + b) tells us about the transparency of the sky. Since different solar PV technologies have different intrinsic module characteristics, the conditions of the sky allow us to dictate the type of solar module technology suitable for a specific climatic and geographic environment. The p-Si technology is expected to be used in desert, arid, or semi-arid regions, where the sum of

AP coefficients (a + b) exceeds 0.65, because it has higher intrinsic modulus properties to withstand extreme temperatures in such climatic conditions with respect to m-Si. Despite the higher energy production, cost-effectiveness, and wider commercialization of m-Si technology compared to p-Si technology, p-Si is highly recommended when considering the effects of climate change on it.

Extreme temperatures, inherently, cause high wind speeds due to low vapour pressure, resulting in low relative humidity and cloud cover, as well as relatively high sunshine duration and fraction in an open savanna [8], suggesting that as the impact of climate change intensifies, extreme temperatures combined with high wind speeds in such open savanna regions may likely result in damaging the solar cell designed to generate voltage for electrification purposes [9]. Extreme wind speed events, on the other hand, have the potential to destroy or damage the module due to the lack of sufficient wind break in open savanna climate regions. These two factors can cause the modules to degrade faster or introduce cracks in the module, potentially reducing the module's energy productivity.

However, m-Si technology is preferred for regions with a low transparency index, which can also be calculated using AP (a + b) coefficients. This will essentially lead to a sharper reduction in global solar radiation and, in some rare cases, in solar PV generation. The longer the PV cells are exposed to low AP (a+b) environments, implying a high humidity environment, the steeper the expected performance degradation. This could be due to the high concentration of water vapor in the atmosphere, which often leads to the disintegration of the cavity [10].

Cell interconnect failures or broken cells are often exacerbated in m-Si technology compared to p-Si modules, according to Obiwulu *et al*. [11]. This suggests that a local climate and geographic environment with hot and humid weather (as determined by AP coefficients) may accelerate these deterioration processes, which are common in regions with high relative humidity or a low clarity index (implying a low sum of AP coefficients).

AP coefficients (a+b) can also be used to estimate the length of sunlight and clarity index, as well as their implications for climate pressure dynamics and air quality [12]. The Earth's atmosphere is made up of gases, particles, and clouds that form a thin column around the planet. This thin column contains billions of tons of pollutants that change the atmosphere unintentionally. These pollutants are produced by the burning of fossil fuels for energy needs and domestic and industrial transport, as well as forest fires, volcanoes, soil dust, and sea salts. Carbon dioxide, a greenhouse gas, is the final by-product of all forms of combustion [13]. According to Ramanathan and Feng [14], the cumulative effects of these reactions produce ozone, another greenhouse gas that is a major contributor to global warming and climate change.

As a result of the renewable energy and atmospheric benefits of the AP model, countless empirical models based on the AP model and other modified models such as exponential, logarithmic, quadratic, polynomial, and power law models have been introduced worldwide, among others, for the estimation of global solar radiation. This pattern is well documented for Nigeria [15], West Africa [16], Africa [17], India [18], China [19], and the globe [20].

The availability and demand for air temperature input data, which can be easily measured globally, are of particular interest in temperature prediction models. Hargreaves and Samani [21] developed the first temperature-based model for predicting global solar radiation, using maximum and minimum temperatures and extraterrestrial solar radiation as input parameters, and obtained an empirical coefficient of 0.17, as shown in Equation 3. It has since been recognized as one of the most popular, simple, and accurate temperature models for predicting global solar radiation and can be used for short- and long-term predictions of global solar radiation expressed as:

$$\frac{H}{Ho} = 0.17(\Delta T)^{0.5} \qquad (3)$$

where H is the extraterrestrial solar radiation on a horizontal surface, is the temperature gradient depicting the difference between the maximum and minimum temperature?

This model has been used by numerous researchers to predict global solar radiation in various parts of the world. However, because of differences in climatic and geographical conditions unique to different locations around the world, the obtained coefficients of 0.17 seem to vary considerably.

When the hours of sunshine datasets needed to evaluate the AP model were not available due to cost, the instrumentation network, or the expertise required for ground-based observations, researchers have often used this approach to primarily generate solar energy data. On the other hand, this study suggests that climate and geographic location-specific Hargreave-Samani adjustment coefficients (AHC) can be used to estimate climate pressure dynamics and air quality in inland and coastal regions. Some investigators reported that the AHS coefficient ranged from 0.19 to 0.21 in coastal regions [22, 23] and fell below this range in inland regions to around 0.17 depending on the local climate and geographical conditions of the sites.

When evaluating their impacts on climate forcing dynamics and air quality in a given location, what does a higher AHC value inland or a lower value in the coastal region imply? The higher AHC value obtained for coastal regions often indicates high cloud cover and relative humidity, which can return additional longwave radiation to the ground, reducing the influence of the air temperature gradient on global solar radiation. This means that the smaller the air temperature gradient, mainly caused by the influence of open water bodies on the atmosphere, the longer the AHC, which can lead to large errors in estimating global solar radiation using the Hargreaves-Samani (HS), and vice versa.

According to atmospheric research, increased or greater values of cloud cover and relative humidity increase diffuse solar radiation and decrease the normal direct radiation available through scattering; at the same time, global solar radiation remains undisturbed. This reduces the amount of conventional direct radiation available that is needed to generate more solar energy for concentrated solar power (CSP). Normal direct solar radiation must be equal to or slightly higher than global solar radiation for concentrated solar power to work effectively [24]. Solar PV technologies, on the other hand, can still be used in this climate. Basically, m-Si technology is recommended for the maximum use of solar energy because its inherent properties favour scattered light over p-Si in places with higher levels of global solar radiation than with normal direct irradiation.

Therefore, the first objective of this paper was to provide AP and HS coefficients in West Africa using generalized datasets that have not been used in the literature since the beginning of solar radiation prediction. In addition, the study proposes a qualitative approach to the analysis of the implications of the AP and HS coefficients for predicting global solar radiation and potential evapotranspiration on climate pressure dynamics, as well as suitable solar PV technology and solar energy concentration in West Africa, which have not been previously implemented in the literature using generalized data sets for the region. Third, the authors proposed an analytical approach based on a rigorous error metric analysis to determine the predictability of the APC (a = 0.25 and b = 0.5) recommended by the Food and Agriculture Organization (FAO) to estimate potential evapotranspiration when no ground observations are available, as well as validation of the AHC's performance for the prediction of global solar radiation in West Africa in this era of climate change and global sustainability, which has been studied in the literature using generalized regression.

Materials and Methods

Data Description, Quality and Modeling

Surface downwelling shortwave radiation (hereafter, global solar radiation, W/m^2), incident shortwave radiation in the upper atmosphere (hereafter, extraterrestrial, W/m^2), total fraction of clouds (%), relative humidity (%), minimum surface air temperature (T_{min}) at 2 m height (^{o}C), maximum cloud air temperature surface (T_{max}) at 2 m height (^{o}C), with monthly spatial resolution were used in this study. These datasets were generated from two different Global Climate Model (GCM) outputs participating in Coupled Model Intercomparison Project Phase 6 (CMIP6). The datasets were downloaded using the latitudes cutting across North (28^o) and South (30^o), as well as the longitudes cutting across the west (-28^o) and east (15^o) of West Africa as a sub-region on the Africa continent under monthly time resolution as shown in Fig. 1. Using a conversion factor of 11.6, the obtained datasets for global solar radiation and extraterrestrial solar radiation in W/m^2 were converted to MJ/m^2/d. Meteo-solar parameters were used to fit the Anstrom-Prescott [5] and Hargreaves-Samani [21] coefficients to global solar radiation prediction models, as well as to assess the implications of the coefficients on climate forcing dynamics and technology selection for solar photovoltaic in the West African Region.

The two GCMs (National Oceanic and Atmospheric Administration, Geophysical Fluid Dynamics Laboratory, USA (GFDL-ESM4), and National Centre for Meteorological Research, France (HadGEM3-GC31) are chosen based on the availability of relevant energy variables for all selected SSPs developed by the European Centre for Medium Weather Forecasts (ECMWF) (https://www.ecmwf.int/en/forecasts/datasets/reanalysis-datasets/era5). Table 1 presents a summary of the GCMs along with their spatiotemporal resolution.

Table 1. Summary of two Global Climate Models (GCMs) from Coupled Model Intercomparison Project Phase 6 (CMIP6)

Model	Centre	Grid size (long × lat) /Spatial resolution		Temporal resolution
		Historical	Future	
GFDL-ESM4	National Oceanic and Atmospheric Administration, Geophysical Fluid Dynamics Laboratory	288 × 180 (1.25° × 1.00°)	288 × 180 (1.25° × 1.00°)	Monthly
HadGEM3-GC31	National Centre for Meteorological Research, France	1024 × 768 (0.35° × 0.23°)	432 × 324 (0.83° × 0.55°)	Monthly

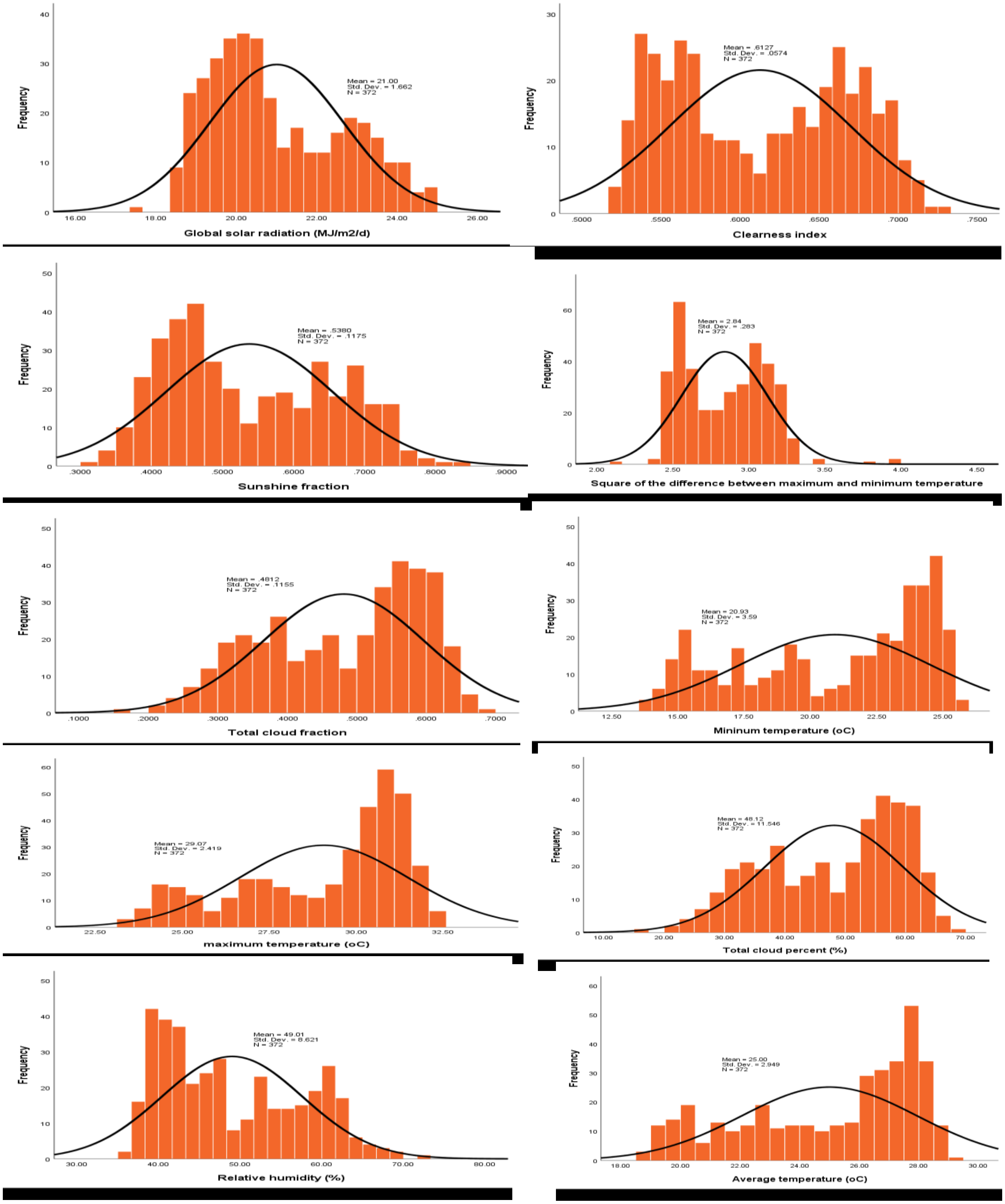

Fig. 1. Descriptive statistics of input and output parameters

Since these two GCM model outputs have different spatial resolutions, they were averaged to reduce the margin of error. The total cloud fraction parameter was used to evaluate the fraction of sunlight in addition to the above parameters, which are used directly to predict global solar radiation. Equation (4) describes the fit of the conventional numerical model using the high-resolution sunshine fraction (S/So) and total cloud fraction (clt) parameters obtained from Zhu *et al*. [25]:

$$S/S_o = 0.946 - 0.6355(clt/100) - 0.4173(clt/100)^2 \qquad (4)$$

Khorasanizadeh *et al*. [26] developed a scattering technique to independently confirm the quality of the clearness index and sunshine fraction datasets, respectively, as they were important components of the input settings. The Khorasanizadeh *et al*. [26] method was also used to ensure that the quality of the sunshine fraction was checked. The HadGEM3-GC31 datasets were used to test the developed models using historical data from 1984 to 2014. The GFDL-ESM4 climate datasets were used to simulate global solar radiation models for West Africa. Table 2 displays the descriptive statistics for the input and output parameters.

Table 2. Descriptive statistics of the input and output parameters

Parameter	N	Range	Minimum	Maximum	Mean	Std. Deviation
H	372	7.520	17.470	24.980	20.996	1.662
Ho	372	9.690	28.320	38.010	34.497	3.477
kt	372	0.211	0.518	0.730	0.613	0.057
S/So	372	0.507	0.322	0.829	0.538	0.117
ΔT	372	11.200	4.500	15.700	8.139	1.643
ΔT0.5	372	1.840	2.120	3.960	2.839	0.283
Tave	372	10.400	18.600	29.000	24.997	2.949
clt	372	51.300	16.600	67.900	48.122	11.546
RHave	372	36.600	35.400	72.000	49.008	8.621
Tmin	372	12.100	13.750	25.850	20.927	3.590
Tmax	372	9.100	23.350	32.450	29.067	2.419

Where H is the global solar radiation (MJ/m^2/d), Ho stands for extraterrestrial solar radiation (MJ/m^2/d), kt represents clearness index, S/So represents sunshine fraction, ΔT stands for temperature gradient (°C), Tave represents average ambient temperature (°C), clt represents total cloud percent (%), RHave represents average relative humidity (%), Tmin and Tmax represent minimum and maximum temperature respectively in degrees Celsius

On both the monthly and annual timescales for West Africa, the statistically validated clearness index and sunshine fraction were used to fit the Angstrom-Prescott [5] adjusted model (AP). The temperature gradient and the clearness index parameter were used in West Africa to fit the Hargreaves-Samani [21] adjusted model (AHS) on monthly and annual timescales. Table 3 shows the coefficients of the Angstrom-Prescott [5] adjusted model (AP) and the Hargreaves-Samani [21] adjusted model (AHS).

Table 3. The coefficients of the Angstrom-Prescott (AP) and Hargreaves-Samani (HS) and their respective adjusted coefficients in West Africa

Resolution	Angstrom-Prescott (AP) type model		Hargreaves-Samani type model	
	Original AP model	Present study	Original HS model	Present study
January	$\frac{H}{Ho} = 0.25 + 0.50\left(\frac{S}{So}\right)$	$\frac{H}{Ho} = 0.496 + 0.273\left(\frac{S}{So}\right)$	$\frac{H}{Ho} = 0.17(\Delta T)^{0.5}$	$\frac{H}{Ho} = 0.218(\Delta T)^{0.5}$
February	$\frac{H}{Ho} = 0.25 + 0.50\left(\frac{S}{So}\right)$	$\frac{H}{Ho} = 0.475 + 0.304\left(\frac{S}{So}\right)$	$\frac{H}{Ho} = 0.17(\Delta T)^{0.5}$	$\frac{H}{Ho} = 0.214(\Delta T)^{0.5}$
March	$\frac{H}{Ho} = 0.25 + 0.50\left(\frac{S}{So}\right)$	$\frac{H}{Ho} = 0.506 + 0.249\left(\frac{S}{So}\right)$	$\frac{H}{Ho} = 0.17(\Delta T)^{0.5}$	$\frac{H}{Ho} = 0.213(\Delta T)^{0.5}$
April	$\frac{H}{Ho} = 0.25 + 0.50\left(\frac{S}{So}\right)$	$\frac{H}{Ho} = 0.491 + 0.263\left(\frac{S}{So}\right)$	$\frac{H}{Ho} = 0.17(\Delta T)^{0.5}$	$\frac{H}{Ho} = 0.215(\Delta T)^{0.5}$
May	$\frac{H}{Ho} = 0.25 + 0.50\left(\frac{S}{So}\right)$	$\frac{H}{Ho} = 0.436 + 0.343\left(\frac{S}{So}\right)$	$\frac{H}{Ho} = 0.17(\Delta T)^{0.5}$	$\frac{H}{Ho} = 0.214(\Delta T)^{0.5}$
June	$\frac{H}{Ho} = 0.25 + 0.50\left(\frac{S}{So}\right)$	$\frac{H}{Ho} = 0.411 + 0.367\left(\frac{S}{So}\right)$	$\frac{H}{Ho} = 0.17(\Delta T)^{0.5}$	$\frac{H}{Ho} = 0.215(\Delta T)^{0.5}$
July	$\frac{H}{Ho} = 0.25 + 0.50\left(\frac{S}{So}\right)$	$\frac{H}{Ho} = 0.358 + 0.422\left(\frac{S}{So}\right)$	$\frac{H}{Ho} = 0.17(\Delta T)^{0.5}$	$\frac{H}{Ho} = 0.212(\Delta T)^{0.5}$
August	$\frac{H}{Ho} = 0.25 + 0.50\left(\frac{S}{So}\right)$	$\frac{H}{Ho} = 0.346 + 0.437\left(\frac{S}{So}\right)$	$\frac{H}{Ho} = 0.17(\Delta T)^{0.5}$	$\frac{H}{Ho} = 0.215(\Delta T)^{0.5}$
September	$\frac{H}{Ho} = 0.25 + 0.50\left(\frac{S}{So}\right)$	$\frac{H}{Ho} = 0.403 + 0.351\left(\frac{S}{So}\right)$	$\frac{H}{Ho} = 0.17(\Delta T)^{0.5}$	$\frac{H}{Ho} = 0.215(\Delta T)^{0.5}$
October	$\frac{H}{Ho} = 0.25 + 0.50\left(\frac{S}{So}\right)$	$\frac{H}{Ho} = 0.426 + 0.340\left(\frac{S}{So}\right)$	$\frac{H}{Ho} = 0.17(\Delta T)^{0.5}$	$\frac{H}{Ho} = 0.217(\Delta T)^{0.5}$
November	$\frac{H}{Ho} = 0.25 + 0.50\left(\frac{S}{So}\right)$	$\frac{H}{Ho} = 0.437 + 0.342\left(\frac{S}{So}\right)$	$\frac{H}{Ho} = 0.17(\Delta T)^{0.5}$	$\frac{H}{Ho} = 0.223(\Delta T)^{0.5}$
December	$\frac{H}{Ho} = 0.25 + 0.50\left(\frac{S}{So}\right)$	$\frac{H}{Ho} = 0.527 + 0.221\left(\frac{S}{So}\right)$	$\frac{H}{Ho} = 0.17(\Delta T)^{0.5}$	$\frac{H}{Ho} = 0.225(\Delta T)^{0.5}$
Annual	$\frac{H}{Ho} = 0.25 + 0.50\left(\frac{S}{So}\right)$	$\frac{H}{Ho} = 0.366 + 0.459\left(\frac{S}{So}\right)$	$\frac{H}{Ho} = 0.17(\Delta T)^{0.5}$	$\frac{H}{Ho} = 0.216(\Delta T)^{0.5}$

Analytical Tools and Performance Evaluation

The coefficient of determination (R2), root mean square error (RMSE), normalized root mean square error (nRMSE), relative percentage error (RPE), skill score (SS), and mean absolute percentage error (MAPE) were the evaluation metrics used in this study, as shown in Table 4.

Table 4. Details of the statistical indicators

S/N	Abbreviation	Statistical test	Expression	Idea value
1.	R^2	Coefficient of determination	$R^2 = 1 - \left[\frac{\sum_{i=1}^{n}(O_i - P_i)^2}{\sum_{i=1}^{n}(O_i - O_{ave})^2}\right]$	One
2.	RMSE	Root mean square error	$RMSE = \sqrt{\frac{1}{n}\sum_{i=1}^{n}(O_i - P_i)^2}$	Zero
3.	nRMSE	Normalized root mean square error	$nRMSE = \frac{RMSE}{\sum_{i=1}^{n}(H)}$	Zero
4.	RPE	Relative percentage error	$RPE = \sum_{i=1}^{n}\left(\frac{O_i - P_i}{P_i}\right) \times 100$	Zero
5.	SS	Skill score	$SS = 1 - \frac{nRMSE_{present\ study}}{nRMSE_{literature}}$	One
6.	MAPE	Mean absolute percentage error	$MAPE = \frac{1}{n}\sum_{i=1}^{n}\lvert O_i - P_i\rvert \times 100$	Zero

Results and Discussion

Performance of AP Parameters in West Africa

According to the statistics of the AP parameter in the different months and according to the annual time scale (Table 3), the parameter a had a higher value in West Africa. The parameter reported a monthly value of 0.346 in August and a monthly value of 0.527 in December, with a corresponding annual value of 0.366. The monthly variability of parameter b was the inverse of that of parameter a, with a maximum value of 0.437 in August and a minimum value of 0.221 in December, and a corresponding annual value of 0.459, which is the maximum value for parameter b. Figure 2 shows that the trend between the AP parameters (a and b) is inverse for daily, monthly, and annual time scale fluctuations. For example, in August, both parameters a and b produced maximum and minimum values. Consequently, the two parameters converge between June and July, August and September, and December and the annual value. Figure 2 shows that the AP parameter gradually increases from January to August and then begins to decrease from September to December, with an accelerated value of 0.459 representing the maximum during the entire monthly period. In contrast, the AP metric decreased gradually from January to August before starting to accelerate from September to December, with a corresponding decrease in value on the annual time scale. Figure 3 shows that the AP a+b parameter produced somewhat uniform values from May to August, with a minimum value in January and a maximum value of 0.783 in August, while the annual time scale value accelerated over the range 0.733–0.779 between January and December to 0.825.

Table 5. Variation of AP parameters in West Africa

Month	Present study AP parameters			FAO recommended AP parameters		
	a	b	a+b	a	b	a+b
JAN	0.496	0.237	0.733	0.25	0.5	0.75
FEB	0.475	0.304	0.779	0.25	0.5	0.75
MAR	0.506	0.249	0.755	0.25	0.5	0.75
APR	0.491	0.263	0.754	0.25	0.5	0.75
MAY	0.436	0.343	0.779	0.25	0.5	0.75
JUN	0.411	0.367	0.778	0.25	0.5	0.75
JUL	0.358	0.422	0.78	0.25	0.5	0.75
AUG	0.346	0.437	0.783	0.25	0.5	0.75
SEP	0.403	0.351	0.754	0.25	0.5	0.75
OCT	0.426	0.34	0.766	0.25	0.5	0.75
NOV	0.437	0.342	0.779	0.25	0.5	0.75
DEC	0.527	0.221	0.748	0.25	0.5	0.75
ANN	0.366	0.459	0.825	0.25	0.5	0.75

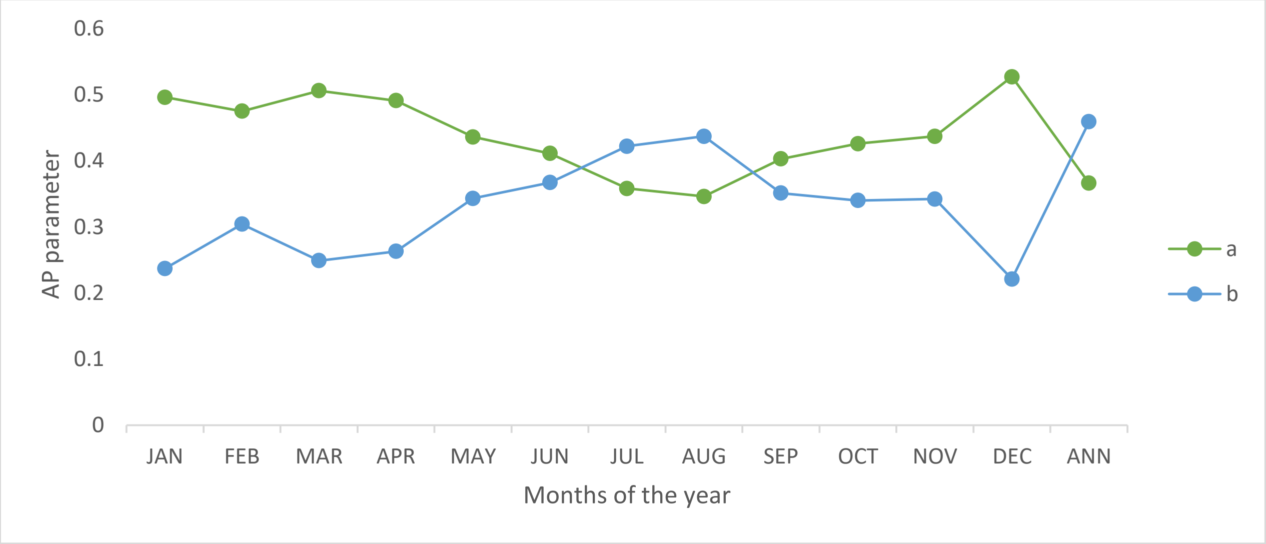

Fig. 2. Variation of AP parameters in West Africa

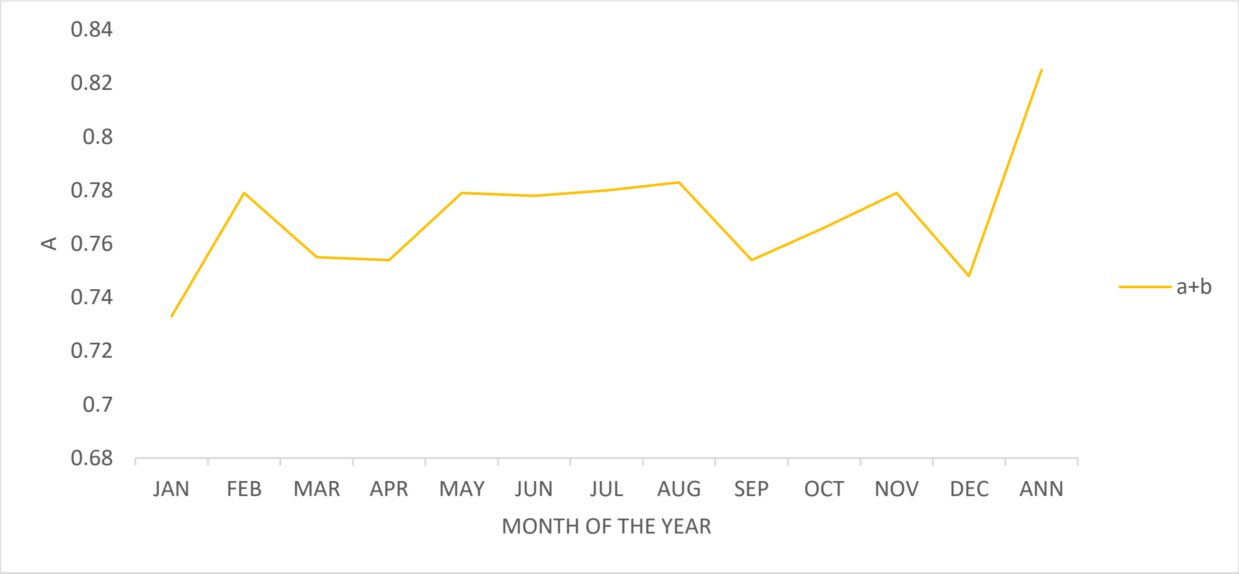

Fig. 3. Variation of a+b AP parameter in West Africa

Compared to the FAO parameter values (a = 0.25 and b = 0.50), the average parameter "a" in each month as well as the annual value were higher, and the monthly value and the annual value of the "b" parameter were lower. If the recommended FAO values of a = 0.25 and b = 0.50 are used to estimate global solar radiation or potential evaporation, the system will have an additional margin of error of 46.4% and a relative percentage error of -8.2%, according to Table 6. Since the annual value is the lowest, a higher margin of error is introduced on a monthly basis, as shown in Table 6. However, in this era of climate change and global warming, it is clear that the AP parameters proposed by the FAO are not suitable for West Africa, as it will be necessary to estimate the impacts of climate change on solar PV generation, net radiation, net primary productivity, and potential evaporation. these solar flux parameters, introducing an additional margin of error due to the sensitivity of climate change to input and output.

Table 6. Error metrics between observed and FAO AP parameters in West Africa

Month/Annual	**a**				**b**			
	RMSE	**MAPE**	**nRMSE**	**RPE**	**RMSE**	**MAPE**	**nRMSE**	**RPE**
JAN	0.0071	0.0413	0.0143	98.4	0.0076	0.0925	0.0320	-52.6
FEB	0.0065	0.0395	0.0137	90.0	0.0057	0.0537	0.0186	-39.2
MAR	0.0074	0.0422	0.0146	102.4	0.0072	0.0840	0.0291	-50.2
APR	0.0070	0.0409	0.0142	96.4	0.0068	0.0751	0.0260	-47.4
MAY	0.0054	0.0356	0.0123	74.4	0.0045	0.0381	0.0132	-31.4
JUN	0.0046	0.0326	0.0113	64.4	0.0038	0.0302	0.0105	-26.6
JUL	0.0031	0.0251	0.0087	43.2	0.0023	0.0154	0.0053	-15.6
AUG	0.0028	0.0231	0.0080	38.4	0.0018	0.0120	0.0042	-12.6
SEP	0.0044	0.0316	0.0110	61.2	0.0043	0.0354	0.0123	-29.8
OCT	0.0051	0.0344	0.0119	70.4	0.0046	0.0392	0.0136	-32.0
NOV	0.0054	0.0357	0.0124	74.8	0.0046	0.0385	0.0133	-31.6
DEC	0.0080	0.0438	0.0152	110.8	0.0081	0.1052	0.0364	-55.8
ANN	0.0033	0.0264	0.0091	46.4	0.0012	0.0074	0.0026	-8.2

Compared to the parameter values (a + b = 0.75) provided by FAO, the average parameter a + b in all months as well as the annual value was higher than expected, with the exception of January and December, which recorded lower values. as shown in Table 5. Using the recommended FAO value of a+b = 0.75 to estimate global solar radiation or potential evaporation will introduce an additional 10.0% margin of error on the annual mean values of the relative percentage error in the system, according to Table 5. The recommended FAO value is overestimated by -2.3% in January and -0.3% in December, according to Table 7, while other parameters introduce marginal errors between 0.5 and 4.5% for the months that are left. Since this annual value is the lowest, a larger margin of error is introduced on a monthly basis, as shown in Table 7. However, in this era of climate change and global warming, it is clear that the AP parameters recommended by FAO56 (the Food and Agriculture Organization (FAO) Irrigation and Drainage Paper No. 56) are inadequate. suitable for West Africa, as these solar flux parameters will be needed to account for the impact of climate change on solar PV generation, net radiation, net primary production, and potential evaporation, which will introduce an additional margin of error due to input and output sensitivity to changing climate.

Multiple results were obtained from adjusting the AP equation coefficient between the adjusted and recommended values. Most of these studies are based on single or multiple stations [27, 28], and provincial or global study regions, as well as uniform coefficient values, are commonly used in regional studies [29, 30, 31]. Although some regional coefficients were interpolated, they were not optimized. Liu *et al*. [32] show that the coefficient "a" ranges from 0.139 to 0.270, with an average of 0.205 in China.

Table 7. Error metrics between observed and FAO AP a+b parameter in West Africa

Month/Annual	**a+b**			
	RMSE	MAPE	nRMSE	RPE
JAN	0.0005	0.0019	0.0007	-2.3
FEB	0.0008	0.0031	0.0011	3.9
MAR	0.0001	0.0006	0.0002	0.7
APR	0.0001	0.0004	0.0002	0.5
MAY	0.0008	0.0031	0.0011	3.9
JUN	0.0008	0.0030	0.0010	3.7
JUL	0.0009	0.0032	0.0011	4.0
AUG	0.0010	0.0035	0.0012	4.4
SEP	0.0001	0.0004	0.0002	0.5
OCT	0.0005	0.0017	0.0006	2.1
NOV	0.0008	0.0031	0.0011	3.9
DEC	0.0001	0.0002	0.0001	-0.3
ANN	0.0022	0.0076	0.0026	10.0

Performance of A-P Model for Predicting Global Solar Radiation in West Africa

Table 8 summarizes the performance of global solar radiation prediction on monthly and yearly timescales, as well as training and testing timelines, using FAO-recommended AP parameters and those obtained in this study. The statistical error metric obtained using both approaches revealed that the FAO-recommended AP parameters are ineffective for predicting global solar radiation, whereas those fitted using the parameters in this manner performed significantly better for both the training and training categories. For example, for all 13 models developed between January and December on an annual time scale, the AP parameters developed in this study yielded upper R2 error metrics ranging from 0.451 to 0.929 and lower R2 error metrics ranging from 0.0011 to 0.0022 for MAPE, between 0.0003 and 0.0008 for nRMSE, 0.0095 and 0.4501 for RPE, and 0.8182 and 0.9167 for skill score values. The skill score error metric is used because the higher the R2 values, the closer they are to one, and the lower the nRMSE values, and the RPE may not fully reveal how accurately predictive performance differs between the FAO-recommended approach and the models adapted in this study.

A skill score error metric indicator was used to compare the performance of the approach used in this study with the one recommended by the FAO. A skill score closes to one (between 0.5 and 1) indicates better performance accuracy, while skill scores close to zero and negative values indicate moderate and poor benchmarking results, respectively. Table 8 shows that on an annual time scale, the ability score for all 13 models developed between January and December was between 0.8182 and 0.9167, indicating a lack of predictive ability for the parameters recommended by FAO to assess the potential global solar radiation in West Africa using the AP parameters obtained using the datasets of this study. This may be because the models were built using historical datasets from when global warming had not exceeded 1.0 degree Celsius, compared to the 1.4 degree Celsius reported by the European Center for Medium-Term Weather Forecasts database. beam (ECMWF) in April 2022.

Paulescu *et al*. [33] recently compared the performance of developed AP parameters derived from ground-based data from WRDC and BSRN with four online platforms. The authors found that the performance of platforms using the AP equation is broadly comparable, with ability scores ranging from 6.1% to 40%. They also stated that both platforms and AP parameters are climate-sensitive; however, AP parameters outperformed platforms in tropical and continental climates. The authors also found that no AP equations outperformed the platforms in all seasons and that no platforms outperformed the AP equations in all seasons. According to Paulescu *et al*. [33], there is no recommendation for using a platform or empirical equation. The models developed by the online platform exceeded FAO parameters in this study. Thorough testing of radiometric sources (satellites, reanalyses, empirical equations) against reliable data measured from the ground, as well as dissemination of results, are general requirements for scientific progress in solar radiation modeling and selection of the appropriate model in solar engineering. This would make it easier to compare the results of different scientific studies.

Table 8. Performance of Angstrom-Prescott model for estimating global solar radiation in West Africa

Model #		**Training Model Fit statistics**					**Testing Model Fit statistics**				
		R2	MAPE	nRMSE	RPE	Skill Score	R2	MAPE	nRMSE	RPE	Skill Score
JAN	Present study	0.729	0.0010	0.0003	0.0095	0.9167	0.663	0.0009	0.0003	0.0086	0.8334
	FAO	0.699	0.0104	0.0036	14.3714	0.0000	0.635	0.0095	0.0033	13.0649	0.0000
FEB	Present study	0.710	0.0013	0.0005	0.4501	0.8718	0.645	0.0012	0.0005	0.4092	0.7925
	FAO	0.709	0.0113	0.0039	15.7238	0.0000	0.645	0.0103	0.0035	14.2944	0.0000
MAR	Present study	0.451	0.0017	0.0006	0.4182	0.8667	0.410	0.0015	0.0005	0.3802	0.7879
	FAO	0.391	0.0131	0.0045	18.7053	0.0000	0.355	0.0119	0.0041	17.0048	0.0000
APR	Present study	0.714	0.0014	0.0005	0.4023	0.9020	0.649	0.0013	0.0005	0.3657	0.8200

	FAO	0.700	0.0147	0.0051	21.5031	0.0000	0.636	0.0134	0.0046	19.5483	0.0000
MAY	Present study	0.851	0.0014	0.0005	0.4015	0.9074	0.774	0.0013	0.0005	0.3650	0.8249
	FAO	0.829	0.0156	0.0054	23.1318	0.0000	0.754	0.0142	0.0049	21.0289	0.0000
JUN	Present study	0.851	0.0015	0.0005	0.3421	0.9074	0.774	0.0014	0.0005	0.3110	0.8249
	FAO	0.562	0.0156	0.0054	23.1274	0.0000	0.511	0.0142	0.0049	21.0249	0.0000
JUL	Present study	0.800	0.0018	0.0006	0.3187	0.8462	0.727	0.0016	0.0005	0.2897	0.7693
	FAO	0.478	0.0112	0.0039	15.6581	0.0000	0.435	0.0102	0.0035	14.2346	0.0000
AUG	Present study	0.792	0.0017	0.0006	0.2955	0.8333	0.720	0.0015	0.0005	0.2686	0.7575
	FAO	0.614	0.0104	0.0036	14.2686	0.0000	0.558	0.0095	0.0033	12.9715	0.0000
SEP	Present study	0.817	0.0017	0.0006	0.2701	0.8696	0.743	0.0015	0.0005	0.2455	0.7905
	FAO	0.726	0.0133	0.0046	19.2397	0.0000	0.660	0.0121	0.0042	17.4906	0.0000
OCT	Present study	0.861	0.0014	0.0005	0.3313	0.9038	0.783	0.0013	0.0005	0.3012	0.8216
	FAO	0.815	0.0149	0.0052	21.9478	0.0000	0.741	0.0135	0.0047	19.9525	0.0000
NOV	Present study	0.929	0.0013	0.0005	0.3886	0.8750	0.845	0.0012	0.0005	0.3533	0.7955
	FAO	0.781	0.0117	0.0040	16.3367	0.0000	0.710	0.0106	0.0036	14.8515	0.0000
DEC	Present study	0.537	0.0013	0.0004	0.4348	0.8919	0.488	0.0012	0.0004	0.3953	0.8108
	FAO	0.509	0.0108	0.0037	15.0118	0.0000	0.463	0.0098	0.0034	13.6471	0.0000
ANN	Present study	0.882	0.0022	0.0008	0.0014	0.8182	0.802	0.0020	0.0007	0.0013	0.7438
	FAO	0.674	0.0128	0.0044	18.3808	0.0000	0.000	0.0000	0.0000	0.0000	0.0000

Performance of Hargreaves-Samani Model for Predicting Global Solar Radiation

Table 9 summarizes the performance of global solar radiation prediction on monthly and yearly timescales, as well as training and testing timelines, using Hargreaves-Samani (HS) parameter and those obtained in this study. The statistical error metric obtained using both approaches revealed that the HS coefficient is ineffective for predicting global solar radiation, whereas those fitted using the coefficient in this study performed significantly better for both the training and training categories.

A skill score error metric indicator was used to compare the performance of the approach used in this study with the HS. A skill score close to one (between 0.5 and 1) indicates better performance accuracy, while skill scores close to zero and negative values indicate moderate and poor benchmarking results, respectively. Table 9 shows that on an annual time scale, the ability score for all 13 models developed between January and December was between 0.800 to 0.937, indicating a lack of predictive ability for the parameters HS model to assess the potential global solar radiation in West Africa using the datasets of this study. This may be because the models were built using historical datasets from when global warming had not exceeded 1.0 degree Celsius, compared to the 1.4 degree Celsius reported by the European Center for Medium-Term Weather Forecasts database. beam (ECMWF) in April 2022.

Table 9. Performance of Hargreaves-Samani model for estimating global solar radiation in West Africa

Model #		Training Model Fit statistics					Testing Model Fit statistics				
		R2	MAPE	nRMSE	RPE	Skill Score	R2	MAPE	nRMSE	RPE	Skill Score
JAN	Present study	0.598	0.0012	0.0004	0.0064	0.937	0.556	0.0011	0.0004	0.0060	0.872
	HS	0.598	0.0183	0.0063	28.2435	0.000	0.556	0.0170	0.0059	26.2730	0.000
FEB	Present study	0.790	0.0016	0.0006	0.8938	0.898	0.735	0.0015	0.0006	0.8314	0.835
	HS	0.800	0.0172	0.0059	25.9703	0.000	0.744	0.0160	0.0055	24.1584	0.000
MAR	Present study	0.917	0.0013	0.0005	0.7001	0.914	0.853	0.0012	0.0005	0.6513	0.850
	HS	0.911	0.0167	0.0058	25.1577	0.000	0.847	0.0155	0.0054	23.4025	0.000
APR	Present study	0.873	0.0018	0.0006	0.7123	0.900	0.812	0.0017	0.0006	0.6626	0.837
	HS	0.877	0.0173	0.0060	26.3106	0.000	0.816	0.0161	0.0056	24.4750	0.000
MAY	Present study	0.799	0.0017	0.0006	0.7975	0.898	0.743	0.0016	0.0006	0.7419	0.835
	HS	0.815	0.0171	0.0059	25.8491	0.000	0.758	0.0159	0.0055	24.0457	0.000
JUN	Present study	0.014	0.0032	0.0011	0.8735	0.825	0.013	0.0030	0.0010	0.8126	0.767
	HS	0.012	0.0182	0.0063	26.5145	0.000	0.011	0.0169	0.0059	24.6647	0.000
JUL	Present study	0.031	0.0034	0.0012	0.7851	0.800	0.029	0.0032	0.0011	0.7303	0.744
	HS	0.030	0.0173	0.0060	24.6948	0.000	0.028	0.0161	0.0056	22.9719	0.000
AUG	Present study	0.203	0.0017	0.0006	0.6952	0.900	0.189	0.0016	0.0006	0.6467	0.837
	HS	0.207	0.0173	0.0060	26.2890	0.000	0.193	0.0161	0.0056	24.4549	0.000
SEP	Present study	0.242	0.0025	0.0009	0.8635	0.852	0.225	0.0023	0.0008	0.8033	0.793
	HS	0.246	0.0175	0.0061	26.5019	0.000	0.229	0.0163	0.0057	24.6529	0.000
OCT	Present study	0.105	0.0032	0.0011	1.0038	0.828	0.098	0.0030	0.0010	0.9338	0.770
	HS	0.108	0.0184	0.0064	27.8204	0.000	0.100	0.0171	0.0060	25.8794	0.000
NOV	Present study	0.358	0.0033	0.0011	0.7425	0.836	0.333	0.0031	0.0010	0.6907	0.778
	HS	0.354	0.0194	0.0067	30.9011	0.000	0.329	0.0180	0.0062	28.7452	0.000
DEC	Present study	0.007	0.0030	0.0010	1.0837	0.857	0.007	0.0028	0.0009	1.0081	0.797
	HS	0.001	0.0202	0.0070	32.4908	0.000	0.001	0.0188	0.0065	30.2240	0.000
ANN	Present study	0.959	0.0020	0.0007	0.1036	0.887	0.892	0.0019	0.0007	0.0964	0.825
	HS	0.959	0.0179	0.0062	27.1905	0.000	0.892	0.0167	0.0058	25.2935	0.000

Atmospheric Factors Militating the A-P Parameters

The values of parameters a and b, however, can vary from one station to another due to differences in geographical conditions. Therefore, a comprehensive understanding of these parameters is important for accurate estimates of global solar radiation. Therefore, it is crucial to accurately measure parameters a and b in order to properly estimate global solar radiation and further our understanding of regional climatic variations. In particular, the parameter a measures the fraction of radiation reflected by clouds, while the parameter b measures the fraction of radiation transmitted through clouds. This is an important factor because it allows us to determine how much radiation reaches the surface of the Earth and thus affects its climate. By accurately measuring parameters a and b, scientists can better understand how clouds affect the Earth's radiation budget and how this in turn impacts regional climates. Furthermore, it is also important to understand the effect of aerosols on global solar radiation, as these particles can both absorb and reflect incoming radiation. This can have a significant influence on the Earth's energy balance, and therefore it is essential to take aerosols into account when measuring parameters of a and b.

These longwave emissions can interact with other atmospheric gases, such as water vapor and carbon dioxide, creating a complex web of interactions that must be considered when measuring parameters, a and b. Thus, a thorough understanding of the interaction between aerosols and radiation is necessary to accurately measure parameters a and b. Furthermore, aerosols also influence the albedo of the Earth's surface by increasing its reflectivity. This increased reflectivity reduces the amount of incoming solar radiation, thus affecting the overall climate of a region. Additionally, aerosols can also affect the Earth's radiative budget by absorbing and scattering incoming longwave radiation. This absorption and scattering of longwave radiation can increase or decrease the amount of radiation emitted into space, further contributing to regional climate change.

This leads to a decrease in the amount of solar radiation that is received by the Earth's surface, further altering regional climate. Additionally, the presence of aerosols can also affect precipitation patterns due to their effects on cloud formation and dynamics. By acting as a cloud condensation nucleus, aerosols can result in larger droplets in clouds and increased rain or snowfall. In extreme cases, aerosols can also lead to decreased visibility in the atmosphere, causing reduced levels of photosynthesis and reducing the health of terrestrial ecosystems.

From the experimental results, geographic location, meteorological systems, and atmospheric conditions influenced the parameter values [6, 34, 35]. The astronomical radiant fraction that reaches the Earth's surface on a cloudy day is, according to the literature, influenced by atmospheric conditions such as humidity, dust content, cloud type and thickness, and pollutant concentration [36]. It varies with station altitude [37] and is determined primarily by cloud type and thickness, increasing as cloudiness increases [38]. When the sky is clear, the sum (a + b) equals the clarity index, which rises slightly with altitude [39]. The parameter b represents the transport properties (aerosol density) of a cloudless atmosphere under the influence of altitude and is primarily determined by the atmosphere's total water content and turbidity [40].

Liu *et al*. [31] calibrated AP parameters in China using six classification zones. A partial correlation analysis of the calibration parameters and variables showed that the main influences on the calibration parameters were sunlight duration, temperature, altitude, and precipitation. The authors also found that prediction models accounting for changes in altitude performed better in most regions, suggesting that altitude is the main determinant of AP parameters in most regions of China. The results of Liu *et al*. [31] agree with those of Paulescu *et al*. [33], who showed that height is a necessary input variable for the AP model. According to Liu *et al*. [31], only models of the altitude and precipitation parameters could reliably predict the parameters.

Paulescu *et al*. [7] found that altitude influences a, and both latitude and altitude influence b. They demonstrated that the dependence of parameters a and b on latitude and longitude was critical to their fit; however, Liu *et al*. [31] unearthed that predictive model 6 did not outperform Chinese predictive models based on altitude. Furthermore, the researchers found no significant correlations between the parameters and latitude or longitude in different parts of China.

Effects of Angstrom-Prescott Coefficients on Climate Forcing and Solar PV Technology Selection

Solar energy estimators have used the A-P model coefficient "a" to empirically determine the proportion of extraterrestrial solar radiation (Ho) in all sky conditions. Under clear sky conditions, the AP model coefficients (a + b) were used to calculate the proportion of Ho. The AP model based on an annual timescale was applied as an example using generalized datasets, that is,

$$\frac{H}{Ho} = 0.366 + 0.459\left(\frac{S}{So}\right) \quad (5)$$

where a=0.366 and b=0.459

On sunny or clear days, solve equation (5) using the methodology of theoretical physics, where S = So, *i.e.*, S/So = 1. The model parameters are changed to a+b=0.825. This means that under clear sky conditions, approximately 82.5% of extraterrestrial solar radiation (Ho) reaches the horizontal surface, while the remaining percentage is absorbed by clouds. On non-sunny days, however, S = 0, *i.e.*, S/So = 0, and model (5) reduces to a coefficient of 0.366. This means that the clouds absorbed 36.6% of the total available sunlight.

Despite the fact that global solar radiation has three components (namely direct solar radiation, diffuse solar radiation, and reflected solar radiation), the reflected component is often ignored because of its small proportion to the total radiation and the diffuse component. Therefore, most solar meteorological studies consider global solar radiation as a mixture of direct and diffuse components. This means that a greater percentage of the global solar radiation available on the horizontal surface can be attributed to normal direct irradiation on sunny days in West Africa.

According to atmospheric studies, diffuse or diffuse radiation components dominate the available percentage of global solar radiation on non-sunny days (approximately 36.6% according to equation 5). Diffuse light accounts for about 36.6% of global solar radiation on non-sunny days. This means that, compared to a conventional solar module, the use of a monocrystalline (m-Si) solar module with the module's inherent characteristics of trapping and using a higher percentage of available stray light in temperate and humid climates can ensure significantly efficient performance during non-sunny days in the region.

During sunny days, however, a larger percentage of the available global solar radiation (about 82.5% of the total) may be stimulated or produced in a tropical region by normal direct irradiation. This means that the region can experience extreme temperatures due to excess heat being trapped on the horizontal surface for months and days of the year. This could be attributed to clear skies, which allow direct radiation to penetrate easily due to low cloud cover and particulate matter in open savannah, enabling crosswind assessment and purifying air quality. As a result, the weather pressure parameters of clouds and aerosols that attenuate direct solar radiation through scattering and conversion of beam radiation are reduced. As a result, the region is likely to receive high solar fluxes throughout the year except for June-July-August, when the region suffers from a high precipitation regime in most of its southern parts due to open water bodies where increased pressure encourages steam, resulting in high rainfall in those regions. On the other hand, locations in north western Africa will have fewer rainy days and months, as well as longer dry seasons, than locations in the south of the region.

Extreme temperature events, according to the explanation, may be caused by higher tendencies to receive more direct radiation due to the atmosphere opening up as an open savanna region. As a result, the region may require solar PV modules resistant to extreme temperatures to harness the region's abundance of solar radiation, especially in this era of rising global temperatures that are causing climate change and devastating the global environment and economy. This suggests that polycrystalline (p-Si) solar photovoltaic modules suitable for harnessing solar radiation with high-performance capabilities and module resistance to extreme temperatures could be found in the region. According to several literary works, arid, semi-arid and desert locations should use p-Si to harness solar energy fluxes, while humid regions should use m-Si [37, 41, 42]. However, in this era of climate change, the opening up of the atmosphere caused by high clarity index, direct normal irradiance, and low diffuse light, as well as shared socioeconomic pathways caused by low anthropological activity, may not result in increased solar radiation global and ambient temperature. Climate change is caused by a variety of atmospheric forcing factors. Consequently, it is recommended to establish a global climate model in the region accessible through several databases to determine the impacts of climate change on global solar radiation and ambient temperature.

Effects of Hargreaves-Samani (HS) Coefficient on Climate Forcing and Solar PV Technology Selection

In West Africa, the values of the adjusted coefficient of the Hargreaves-Samani model (HS) are generated using the retrieved datasets described in Section 2.

$$H/Ho = 0.216(\Delta T)^{0.5} \qquad (1)$$

$$H/Ho = 0.17(\Delta T)^{0.5} \qquad (2)$$

where equation (1) represents adjusted coefficient of Hargreaves-Samani coefficient obtained for West Africa, whereas, equation (2) stands for original coefficient of Hargreaves-Samani model simulated in North America.

This shows that the adjusted Hargreaves-Samani coefficients (AHC) for West Africa is given as 0.216. The value generated in this study is greater than the results reported by other researchers around the world. Allen *et al.* [22] used the ratio of site atmospheric pressure to sea level to estimate the empirical coefficient of the Hargreaves-Samani (HS) model. Allen reported values of 0.17 for inland regions and 0.20 for coastal regions. Hargreaves *et al.* [23] calibrated the HS model and obtained an AHC of 0.16 for inland regions and 0.19 for coastal regions. Adaramola [43] estimated AHC at 0.1945 for the inland region of Akure, Nigeria. For Osogbo, Nigeria, Ohunakin *et al*. [40] found 0.1141. Nwokolo and Ogbulezie [15] found the following values for different parts of Nigeria: Calabar reported an AHC of 0.27, Port Harcourt 0.25, Uyo 0.25, Yenagoa 0.25, Warri 0.25, Asaba 0.23, and Benin City was 0.20, Ikeja was 0.20, and Enugu, Akure, Ilorin, Ibadan, Lokoja, Jos, Bauchi, Gusau, Yola, Kaduna, Maiduguri, and Sokoto were all 0.20. The authors also performed simulations for Kano and Nigeria as a whole. Overall, the authors obtained values of 0.22 and 0.20 for the coastal and interior regions of Nigeria, respectively.

The AHC coefficient obtained in this study is consistent with those reported globally. However, the differences in values from one site to another could be attributed to the fact that global solar radiation is entirely dependent on the local climate and regional geography of the site. However, this high value of 0.216 corresponds to the high values found mainly in coastal regions around the world. Nwokolo and Ogbulezie [15] reported 0.22 for the coastal region of Nigeria; Allen [22] reported 0.20; and Hargreaves *et al.* [23] reported 0.19 for the coastal region. AHC values should be higher in coastal regions than inland regions, according to numerous experimental results from different parts of the world. This also implies that the smaller the air temperature gradient (difference between maximum and minimum temperature), mainly due to the influence of open bodies of water on the atmosphere, the greater the AHC, which may result in a larger error in estimating global solar radiation (H) from the HS model found in West Africa.

In contrast, the lower AHC obtained in the literature for the interior region is due to a decrease in humidity and cloud cover, which reduces long-wave radiation to the ground, thereby enhancing the effect of air temperature range on global solar radiation, which may cause a lower AHC in the region. This means that the higher the air temperature range, which is primarily caused by decreased humidity, cloud cover, diffuse solar radiation, and so on in the atmosphere, the smaller the AHC, which could improve the HS model's estimation of global solar radiation. For annual values, the AHC value reported in this study is higher than that of the original HS model (0.17).

According to the results, using the original HS model value of 0.17 is grossly inadequate for estimating global solar radiation in West Africa. Rather, a value of 0.216 can improve model performance. However, since the obtained value corresponds to the values of the coastal region as indicated by numerous literature sources [22, 15, 21, 43], an increase in cloudiness, diffuse solar radiation, and humidity, which mainly return additional long-wave radiation to the ground, thus reducing the influence of the air temperature gradient on global solar radiation, is thus expected in the region. This is obvious because the increase in cloud cover, humidity, and diffuse solar radiation, according to various atmospheric researchers, results in a decrease in the direct solar radiation available through the diffusion component of the solar radiation beam, while the solar radiation overall remains constant. However, as global temperatures rise and anthropological activities increase, which is inevitable in a developing region, and more and more additional longwave radiation is added to the ground, global solar radiation is expected to begin to decline rapidly in the near future. while the ambient temperature in the region will rise rapidly. This could lead to a warmer environment, a decrease in global solar radiation potential and normal direct radiation, and an increase in diffuse light. This means that as the global effects of climate change increase, West Africa will become warmer, with a corresponding decrease in global solar and normal direct radiation and an increase in diffuse solar radiation.

In this case, p-Si technology will be the best choice to take advantage of the region's abundant solar energy. This is because, compared to other solar PV modules, the solar technology has higher module intrinsic characteristics to withstand the extreme temperatures of the region. According to Dutta *et al.* [41], solar PV generation will decline in Africa, including North Africa, West Africa, Cameroon, the Republic of the Congo, and the Democratic Republic of the Congo. Photovoltaic and concentrated solar power generation in Africa, North Africa, and West Africa is likely to decline, according to Crook *et al.* [42]. Gaetani *et al.* [44] reduced near-future PV energy availability in Europe and Africa in aerosol-climate modeling experiments. Huber *et al.* [45] investigated the impact of long-term changes in solar radiation projections based on CMIP5 climate models on PV energy yields in Africa and parts of West Africa. According to Zou *et al.* [46], Phase 5 models of a combined intercomparison project in Africa and West Africa showed a reduction in global surface solar radiation and photovoltaic power. Bazyomo *et al*. [47] showed a decline in PV generation in West Africa, with the exception of Sierra Leone. Fant *et al*. [48] projected small changes in solar PV generation in 2050, with an increase in the winter and a decrease in the summer in most regions of Southern Africa. Patchali *et al*. [49] also reported reductions in global solar radiation at several locations in Togo, West Africa. Ohunakin *et al*. [50] showed a decrease in global solar radiation in Nigeria, with the largest possible decrease in southern Nigeria.

Effects of Aerosol and Cloud on Climate Forcing

In general, atmospheric aerosols enhance the scattering of radiation from the sun to the ground. Variations in atmospheric properties such as humidity and aerosol concentrations can significantly modify the spectrum of radiation passing through the atmosphere, both by scattering radiation and by absorbing radiation at specific frequencies. This can counteract the greenhouse effect by reflecting back incoming solar radiation, thus cooling the planet. These solar-radiation management techniques have been discussed in the recent literature in connection with a limitation of aerosol efficacy on regional climate [51]. Some earth science programs have begun to study the effects of indirect aerosolization. Aerosol particles play a role in snow formation and the Arctic Sea ice melt. Indirect aerosol effects enhance satellite views of Earth. They could also modify cloud lifetime and cover ocean surfaces, but there is not enough evidence to say that they have that much effect. CO_2 emissions in the atmosphere are a major cause of global warming and have been estimated to have increased over 30% per year on average between 1973 and 2000. Indeed, as the figures show there have been large reductions in sunshine duration during the 20th century. In the light of this, Pope *et al.* [51] observes that the solar radiation does not reach all places on Earth at the same time; atmospheric particulate matter is a key culprit. The dimming or brightening of the atmosphere is caused by air pollution and can be mitigated. The transmittivity of the atmosphere plays a key role in explaining some of the observed changes in global dimming and brightening. Here, the change in the transmittivity of the atmosphere must come from some causes other than climate change, so "changes in the concentration and optical properties of aerosols" will not suffice. Moderate increases in surface cooling, slow surface heating, drying of air and soil, damage to regional circulation systems, reduced removal of pollutants from the atmosphere and the hydrological cycle are all consequences of light pollution. At present, Earth climate is generally warmer than it was over the last two millennia. While current climate models include both effects, they do not include the feedbacks caused by changes in cloud cover. Solar dimming is a form of cloud interference. The most dramatic solar dimming effects, such as those on the African continent, result from volcanic eruptions and fireballs. Solar dimming results from surface cooling, an increase in atmospheric solar heating, a disruption of regional circulation systems, changes in atmospheric thermal structure, suppression of evaporation and precipitation, a slowing down of the hydrological cycle. Depending on the extent of the alterations, there may be changes in ocean circulation and weather patterns that could cause major alterations in the hydrological cycle. Another consequence of changing oceanic currents might be the shifting of continental glaciers, thereby increasing the Earth's albedo. The anticipated changes to the hydrological cycle could be disastrous. Yet existing estimates show that these effects, even if substantial, cannot be the sole cause of climate change at present. The practical implication is that global dimming results in significantly reduced plant growth [52]. Slight and apparently easily resolved, global dimming may instead have far-reaching effect. Additionally, they play an important role in socialization processes: For instance, they influence the infant's ability to make direct contact with others and its early attachment to the parent. We anticipate that aerosols will pose more hazards as the planet becomes warmer. Salby [53] observes that atmospheric pressure can decrease over a volcanic plume by several millibars. The author, however, concluded the main threat to the earth's climate is the release of sulfuric acid aerosols by volcanoes. He also argues that when volcanic eruptions release particles into the atmosphere, they cool down the troposphere and thus slow global warming. In the mid-nineteenth century, dust particles originating in Asian deserts accumulated over Europe and Northern America, causing violent storms that produced both summer and winter droughts. Contrary to Salby's assertions, it is well known that volcanic eruptions affect climate change. These aerosols serve as scavengers, with the effect of allowing a residual layer to exist at the interface between air and water. For example, large volcanic eruptions and such fluctuations in the content of atmospheric aerosols affect how aerosols are transported to different regions of the atmosphere [54]. The increasing frequency of ash emissions observed since the start of the twentieth century coincides with a significant cooling of the Earth's climate. Over time, aerosols (large particles and droplets in the atmosphere) play an important role in climate fluctuations. Scientists have studied the albedo effect and aerosols for centuries, but this novel provides a very human look at the result of increased emissions. Earth's climate fluctuates rapidly, because the net radiation to Earth is altered by the sun's light and heat output. One of the most important roles that aerosols play in climate change is to scatter sunlight, which is an essential aspect of the general circulation process. Besides also reflecting the influences of global climate change, volcanic eruptions may lead to an increase in ozone depletion [55] and an overall decrease in cloudiness and dimming of sunshine at earth's surface. Thus, the anthropogenic emissions of aerosols impact climate changes [56]. The variable equilibrium constants (K) of some phase changes tend to decrease with increased concentrations of aerosols [57]. The moisture content, cloud liquid water content, and latent heat storage characteristics of the atmosphere show a consistent response to aerosol increases [58]. When the albedo effect is balanced by aerosol absorption of incoming radiation, this causes the net cooling effect in polar areas.

Effects of Cloud and Aerosols on Air Quality

One interpretation of this plot idea is that the climate forcing effects of aerosols and clouds influence air quality through the following processes and mechanisms: causing small but significant changes in ventilation rates; precipitation scavenging; changes in chemical production and loss rates; and dry deposition. In the earlier studies, the ozone concentration had a low sensitivity to temperature (2 to 3.7 times less) than had been observed for PM10 [non-particulate matter] and black carbon. The researchers found that ozone is strongly associated with temperature, as ozone concentrations in both warm and cold years decrease and increase, respectively. Since the date at which the temperature of the Earth's atmosphere began to rise, it has increased annually by 0.85 K. The warming that results from the burning of fossil fuels has major implications for the chemical composition of ozone, a pollutant of considerable concern for public health. Although it was previously known that ozone was dependent on temperature and altitude, the findings from this study were remarkable. Ozone is a reactive, unstable chemical formed from oxygen molecules when ultraviolet light from the sun hits ground level pollutants. Ozone is a molecule that consists of three oxygen atoms bound together in a molecule that resembles an H. A new study [60] published recently showed that temperature correlated with ozone and water vapor in the atmosphere over land. An increasing number of studies suggest that an increase in temperature is the main cause of this ozone depletion. From 1940 to 1976, the earth was cooler, and during this time there were three times as many days when the minimum overlying ozone concentration fell below 0.12 parts per billion (ppb). The best correlation, from which the present-day figure of 0.84 is derived, occurs between ozone and temperature in the lower atmosphere. Therefore, according to the authors, ozone forms when warmer air near the surface moves upward toward cooler layers of air. Today, this knowledge has helped us make considerable progress in reducing stratospheric ozone depletion, which would eventually lead to a significant reduction of ultraviolet radiation reaching the Earth's surface. Ozone and high temperatures are examples of a positive autocorrelation because ozone is sensitive to changing temperature and higher temperatures lead to more ozone, in spite of the fact that these variables have no direct causal relationship. Ozone is a poisonous gas, found in the atmosphere and emitted by some industrial emissions and forest fires. Large numbers of ozone molecules can be created when sunlight breaks apart ozone molecules with oxygen atoms (ozone is comprised of two oxygen atoms). Ozone affects temperatures through absorption of infrared radiation by liquid water, which returns the energy to space as long as it remains liquid.

Ozone production occurs in the stratosphere as well, where the ionization of water molecules by solar ultraviolet radiation (UV) reduces the reactive hydroxyl radical. Most of these NMVOCs are harmful to the ozone layer and produce secondary organic aerosols (SOAs) [59]. As the concentrations of NMVOCs and NO_x in the atmosphere rise due to anthropogenic climate change, ozone levels are expected to increase [60]. Ozone is produced in the troposphere by the photochemical oxidation of carbon monoxide (CO), methane and non-methane volatile organic compounds (NMVOCs), and the hydroxyl radical in the presence of reactive nitrogen oxides.

CONCLUSIONS

The effects of the Angstrom-Prescott [5] and Hargreaves-Samani [21] coefficients on climate forcing and solar PV technology selection in West Africa were studied using monthly averaging datasets. The main finding was that the Angstrom-Prescott and Hargreaves-Samani coefficients are ineffective for assessing global solar radiation over West Africa. On the other hand, coefficients fitted in this study were more efficient for calculating the Angstrom-Prescott and Hargreaves-Samani coefficients in the region. Consequently, if global solar radiation ground measurement datasets were not available in West Africa, the following models based on sunlight and temperature could be used:

$$\frac{H}{Ho} = 0.366 + 0.459\left(\frac{S}{So}\right) \tag{6}$$

$$\frac{H}{Ho} = 0.216(\Delta T)^{0.5} \tag{7}$$

According to the above equation, AP parameters obtained on an annual basis include a = 0.366 and b = 0.459, whereas the Hargreaves-Samani coefficient of 0.216 can be used as more accurate parameters than the FAO-recommended a = 0.25 and b = 0.5, as well as the 0.17 recommended by Hargreaves and Samani [21]. The effects of the Angstrom-Prescott and Hargreaves-Samani coefficients were also examined to determine the best solar PV model for West Africa. According to the parameters of the Angstrom-Prescott and Hargreaves-Samani coefficients, the p-Si module is more reliable than the m-Si module, because the p-Si module has a higher tendency to withstand the high temperatures projected to affect the region due to its higher module intrinsic properties [61].

ACKNOWLEDGMENTS

The authors would like to acknowledge the European Centre for Medium Weather Forecasts (ECMWF) for providing the data used in this study.

REFERENCES

[1] Beiter, P. C., Vincent, N. M., and Ma, O. (2018). *2016 Renewable Energy Grid Integration Data Book* (No. NREL/BK-6A20-71151). National Renewable Energy Lab.(NREL), Golden, CO (United States).

[2] Benatallah, M., Bailek, N., Bouchouicha, K., Sharifi, A., Abdel-Hadi, Y., Nwokolo, S., S. Band, S., Jamil, B., Mosavi, A., and El-kenawy, E.-S. (2022). Exploring the ability of hybrid extreme machine-based methods to predict solar radiation-a case study of Sahara middle South, Algeria. *NRIAG Journal of Astronomy and Geophysics*.

[3] Kimball, H. H. (1919). Variations in the total and luminous solar radiation with geographical position in the United States. *Monthly Weather Review*, 47(11), 769-793. DOI: https://doi.org/10.1175/1520-0493(1919)47<769:vittal>2.0.co;2

[4] Angstrom, A. (1924). Solar and terrestrial radiation. Report to the international commission for solar research on actinometric investigations of solar and atmospheric radiation. 50(210), 121-126. DOI: https://doi.org/10.1002/qj.49705021008

[5] Prescott, J. (1940). Evaporation from Water Surface in Relation to Solar Radiation. *Trans R Soc South Aust,* 64,114–118.

[6] Nwokolo, S. C., Amadi, S. O., Obiwulu, A. U., Ogbulezie, J. C., and Eyibio, E. E. (2022). Prediction of global solar radiation potential for sustainable and cleaner energy generation using improved Angstrom-Prescott and Gumbel probabilistic models. *Cleaner Engineering and Technology*, 6, 100416. DOI: https://doi.org/10.1016/j.clet.2022.100416

[7] Paulescu, M., Stefu, N., Calinoiu, D., Paulescu, E., Pop, N., Boata, R., and Mares, O. (2016). Ångström–Prescott equation: Physical basis, empirical models and sensitivity analysis. *Renewable and Sustainable Energy Reviews*, 62, 495-506.

[8] Nwokolo, S. C., Obiwulu, A. U., Ogbulezie, J. C., and Amadi, S. O. (2022). Hybridization of statistical machine learning and numerical models for improving beam, diffuse and global solar radiation prediction. *Cleaner Engineering and Technology*, 9, 100529. DOI: https://doi.org/10.1016/j.clet.2022.100529

[9] Obiwulu, A. U., Erusiafe, N., Olopade, M. A., and Nwokolo, S. C. (2022). Modeling and estimation of the optimal tilt angle, maximum incident solar radiation, and global radiation index of the photovoltaic system. *Heliyon*, 8(6). DOI:

10.1016/j.heliyon.2022.e09598
[10] Obiwulu, A. U., Chendo, M. A. C., Erusiafe, N., and Nwokolo, S. C. (2020). Implicit meteorological parameter-based empirical models for estimating back temperature solar modules under varying tilt-angles in Lagos, Nigeria. *Renewable Energy*, 145, 442-457. DOI: https://doi.org/10.1016/j.renene.2019.05.136
[11] Obiwulu, A. U., Erusiafe, N., Olopade, M. A., and Nwokolo, S. C. (2020). Modeling and optimization of back temperature models of mono-crystalline silicon modules with special focus on the effect of meteorological and geographical parameters on PV performance. *Renewable Energy*, 154, 404-431. DOI: https://doi.org/10.1016/j.renene.2020.02.103
[12] Amadi, S. O., Dike, T., and Nwokolo, S. C. (2020). Global Solar Radiation Characteristics at Calabar and Port Harcourt Cities in Nigeria. *Trends in Renewable Energy*, 6(2), 111-130. DOI: https://doi.org/10.17737/tre.2020.6.2.00114
[13] Nwokolo, S. C., Ogbulezie, J. C., and Obiwulu, A. U. (2022). Impacts of climate change and meteo-solar parameters on photosynthetically active radiation prediction using hybrid machine learning with Physics-based models. *Advances in Space Research*, 70(11), 3614-3637. DOI: https://doi.org/10.1016/j.asr.2022.08.010
[14] Ramanathan, V., and Feng, Y. (2009). Air pollution, greenhouse gases and climate change: Global and regional perspectives. *Atmospheric Environment*, 43(1), 37-50. DOI: https://doi.org/10.1016/j.atmosenv.2008.09.063
[15] Nwokolo, S.C., and Ogbulezie, J.C. (2017). A single hybrid parameter-based model for calibrating hargreaves-samani coefficient in Nigeria. Int J Phys Res 5(2), 49. DOI: https://doi.org/10.14419/ijpr.v5i2.8042
[16] Nwokolo, S.C., and Ogbulezie, J.C. (2018). A quantitative review and classification of empirical models for predicting global solar radiation in West Africa. *Beni-Suef Univ J Basic Appl Sci*, 7,367–396. DOI: https://doi.org/10.1016/j.bjbas.2017.05.001
[17] Nwokolo, S.C. (2017). A comprehensive review of empirical models for estimating global solar radiation in Africa. *Renew Sustain Energy Rev*, 78, 955–995. DOI: https://doi.org/10.1016/j.rser.2017.04.101
[18] Makade, R. G., Chakrabarti, S., and Jamil, B. (2021). Development of global solar radiation models: A comprehensive review and statistical analysis for Indian regions. *Journal of Cleaner Production*, 293, 126208. DOI: https://doi.org/10.1016/j.jclepro.2021.126208
[19] Gouda, S. G., Hussein, Z., Luo, S., and Yuan, Q. (2020). Review of empirical solar radiation models for estimating global solar radiation of various climate zones of China. 44(2), 168-188. DOI: https://doi.org/10.1177/0309133319867213
[20] Almorox, J., Voyant, C., Bailek, N., Kuriqi, A., and Arnaldo, J. A. (2021). Total solar irradiance's effect on the performance of empirical models for estimating global solar radiation: An empirical-based review. *Energy*, 236, 121486. DOI: https://doi.org/10.1016/j.energy.2021.121486
[21] Hargreaves, G. H., and Samani, Z. A. (1982). Estimating potential evapotranspiration. *Journal of the irrigation and Drainage Division*, *108*(3), 225-230. DOI: https://doi.org/10.1061/taceat.0008673
[22] Allen, R. G., Pereira, L. S., Raes, D., and Smith, M. (1998). Crop

evapotranspiration-Guidelines for computing crop water requirements-FAO Irrigation and drainage paper 56. *Fao, Rome*, *300*(9), D05109.

[23] Hargreaves, G. L., Hargreaves, G. H., and Riley, J. P. (1985). Irrigation Water Requirements for Senegal River Basin. 111(3), 265-275. DOI: doi:10.1061/(ASCE)0733-9437(1985)111:3(265)

[24] Nwokolo, S.C. and Otse, C.Q. (2019). Impact of Sunshine Duration and Clearness Index on Diffuse Solar Radiation Estimation in Mountainous Climate. *Trends in Renewable Energy*, 5, 307-332. DOI: 10.17737/tre.2019.5.3.00107

[25] Zhu, W., Wu, B., Yan, N., Ma, Z., Wang, L., Liu, W., Xing, Q., and Xu, J. (2019). Estimating sunshine duration using hourly total cloud amount data from a geostationary meteorological satellite. *Atmosphere*, 11(1), 26. DOI: https://doi.org/10.3390/ATMOS11010026

[26] Khorasanizadeh, H., and Mohammadi, K. (2016). Diffuse solar radiation on a horizontal surface: Reviewing and categorizing the empirical models. *Renewable and Sustainable Energy Reviews*, 53, 338-362. DOI: https://doi.org/10.1016/j.rser.2015.08.037

[27] Besharat, F., Dehghan, A. A., and Faghih, A. R. (2013). Empirical models for estimating global solar radiation: A review and case study. *Renewable and Sustainable Energy Reviews*, 21, 798-821. DOI: https://doi.org/10.1016/j.rser.2012.12.043

[28] Liu, Y., Zhou, Y., Chen, Y., Wang, D., Wang, Y., and Zhu, Y. (2020). Comparison of support vector machine and copula-based nonlinear quantile regression for estimating the daily diffuse solar radiation: A case study in China. *Renewable Energy*, 146, 1101-1112. DOI: https://doi.org/10.1016/j.renene.2019.07.053

[29] Govindasamy, T. R., and Chetty, N. (2021). Machine learning models to quantify the influence of PM10 aerosol concentration on global solar radiation prediction in South Africa. *Cleaner Engineering and Technology*, 2, 100042. DOI: https://doi.org/10.1016/j.clet.2021.100042

[30] Li, M.-F., Fan, L., Liu, H.-B., Guo, P.-T., and Wu, W. (2013). A general model for estimation of daily global solar radiation using air temperatures and site geographic parameters in Southwest China. *Journal of Atmospheric and Solar-Terrestrial Physics*, 92, 145-150. DOI: https://doi.org/10.1016/j.jastp.2012.11.001

[31] Liu, Y., Zhou, Y., Wang, D., Wang, Y., Li, Y., and Zhu, Y. (2018). Reply to "Comments on ["Classification of solar radiation zones and general models for estimating the daily global solar radiation on horizontal surfaces in China"[Energy Convers. Manage. 154 (2017) 168–179] by Liu et al.]". *Energy Conversion and Management*, *168*, 653-654.

[32] Liu, Y., Tan, Q., and Pan, T. (2019). Determining the parameters of the Ångström-Prescott model for estimating solar radiation in different regions of China: Calibration and modeling. *Earth and Space Science*, 6(10), 1976-1986. DOI: https://doi.org/10.1029/2019EA000635

[33] Paulescu, M., Badescu, V., Budea, S., and Dumitrescu, A. (2022). Empirical sunshine-based models vs online estimators for solar resources. *Renewable and Sustainable Energy Reviews*, 168, 112868. DOI:

https://doi.org/10.1016/j.rser.2022.112868

[34] Almorox, J., Hontoria, C., and Benito, M. (2011). Models for obtaining daily global solar radiation with measured air temperature data in Madrid (Spain). *Applied Energy*, 88(5), 1703-1709. DOI: https://doi.org/10.1016/j.apenergy.2010.11.003

[35] Chen, R., Ersi, K., Yang, J., Lu, S., and Zhao, W. (2004). Validation of five global radiation models with measured daily data in China. *Energy Conversion and Management*, 45(11), 1759-1769. DOI: https://doi.org/10.1016/j.enconman.2003.09.019

[36] de Barros Silva, A. W., Freitas, B. B., de Alencar Filho, C. L., de Freitas, C. D., de Sousa Junior, E. A., de Castro, E. S., de Araújo, E.M., Correia, F.I.F., da Silva, F.R.P., de Souza, J.J.S., and Martins, L.L.A.P. (2022). Methodology Based on Artificial Neural Networks for Hourly Forecasting of PV Plants Generation. *IEEE Latin America Transactions*, *20*(4), 659-668. DOI: https://doi.org/10.1109/TLA.2022.9675472

[37] Nwokolo, S.C., Obiwulu, A.U., and Ogbulezie, J.C. (2023). Machine learning and analytical model hybridization to assess the impact of climate. *Phys Chem Earth*, (In press)

[38] Hassan, M. A., Bailek, N., Bouchouicha, K., and Nwokolo, S. C. (2021). Ultra-short-term exogenous forecasting of photovoltaic power production using genetically optimized non-linear auto-regressive recurrent neural networks. *Renewable Energy*, 171, 191-209. DOI: https://doi.org/10.1016/j.renene.2021.02.103

[39] Hassan, M. A., Bailek, N., Bouchouicha, K., Ibrahim, A., Jamil, B., Kuriqi, A., Nwokolo, S. C., and El-kenawy, E.-S. M. (2022). Evaluation of energy extraction of PV systems affected by environmental factors under real outdoor conditions. *Theoretical and Applied Climatology*, 150(1), 715-729. DOI: 10.1007/s00704-022-04166-6

[40] Ohunakin, O. S., Adaramola, M. S., Oyewola, O. M., and Fagbenle, R. O. (2013). Correlations for estimating solar radiation using sunshine hours and temperature measurement in Osogbo, Osun State, Nigeria. *Frontiers in Energy*, 7(2), 214-222. DOI: 10.1007/s11708-013-0241-2

[41] Dutta, R., Chanda, K., and Maity, R. (2022). Future of solar energy potential in a changing climate across the world: A CMIP6 multi-model ensemble analysis. *Renewable Energy*, 188, 819-829. DOI: https://doi.org/10.1016/j.renene.2022.02.023

[42] Crook, J. A., Jones, L. A., Forster, P. M., and Crook, R. (2011). Climate change impacts on future photovoltaic and concentrated solar power energy output. *Energy & Environmental Science*, 4(9), 3101-3109. DOI: https://doi.org/10.1039/c1ee01495a

[43] Adaramola, M. S. (2012). Estimating global solar radiation using common meteorological data in Akure, Nigeria. *Renewable Energy*, 47, 38-44. DOI: https://doi.org/10.1016/j.renene.2012.04.005

[44] Gaetani, M., Huld, T., Vignati, E., Monforti-Ferrario, F., Dosio, A., and Raes, F. (2014). The near future availability of photovoltaic energy in Europe and Africa in

climate-aerosol modeling experiments. *Renewable and Sustainable Energy Reviews*, 38, 706-716. DOI: https://doi.org/10.1016/j.rser.2014.07.041

[45] Huber, I., Bugliaro, L., Ponater, M., Garny, H., Emde, C., and Mayer, B. (2016). Do climate models project changes in solar resources? *Solar Energy*, 129, 65-84. DOI: https://doi.org/10.1016/j.solener.2015.12.016

[46] Zou, L., Wang, L., Li, J., Lu, Y., Gong, W., and Niu, Y. (2019). Global surface solar radiation and photovoltaic power from Coupled Model Intercomparison Project Phase 5 climate models. *Journal of Cleaner Production*, 224, 304-324. DOI: https://doi.org/10.1016/j.jclepro.2019.03.268

[47] Bazyomo, S. D. Y. B., Lawin, E. A., Coulibaly, O., and Ouedraogo, A. (2016). Forecasted changes in West Africa photovoltaic energy output by 2045. *Climate*, 4(4), 53. DOI: https://doi.org/10.3390/cli4040053

[48] Fant, C., Adam Schlosser, C., and Strzepek, K. (2016). The impact of climate change on wind and solar resources in southern Africa. *Applied Energy*, 161, 556-564. DOI: https://doi.org/10.1016/j.apenergy.2015.03.042

[49] Patchali, T. E., Ajide, O. O., Matthew, O. J., Salau, T. A. O., and Oyewola, O. M. (2020). Examination of potential impacts of future climate change on solar radiation in Togo, West Africa. *SN Applied Sciences*, 2(12), 1941. DOI: https://doi.org/10.1007/s42452-020-03738-3

[50] Ohunakin, O. S., Adaramola, M. S., Oyewola, O. M., Matthew, O. J., and Fagbenle, R. O. (2015). The effect of climate change on solar radiation in Nigeria. *Solar Energy*, 116, 272-286. DOI: https://doi.org/10.1016/j.solener.2015.03.027

[51] Pope, F. D., Braesicke, P., Grainger, R. G., Kalberer, M., Watson, I. M., Davidson, P. J., and Cox, R. A. (2012). Stratospheric aerosol particles and solar-radiation management. *Nature Climate Change*, *2*(10), 713-719.

[52] Amadi, S. O., andUdo, S. O. (2018). A Study of Multi-Annual Variability of Effective Sunshine Duration in Nigeria and Its Implications for Climate Forcing and Air Quality. *Journal of Health and Environmental Studies*, 2(2), 13-30.

[53] Salby, M. L. (2012). *Physics of the Atmosphere and Climate*. Cambridge University Press.

[54] Viana, M., Pey, J., Querol, X., Alastuey, A., de Leeuw, F., and Lükewille, A. (2014). Natural sources of atmospheric aerosols influencing air quality across Europe. *Science of The Total Environment*, 472, 825-833. DOI: https://doi.org/10.1016/j.scitotenv.2013.11.140

[55] Bais, A. F., McKenzie, R. L., Bernhard, G., Aucamp, P. J., Ilyas, M., Madronich, S., & Tourpali, K. (2015). Ozone depletion and climate change: impacts on UV radiation. *Photochemical & Photobiological Sciences*, *14*(1), 19-52.

[56] Levy II, H., Horowitz, L. W., Schwarzkopf, M. D., Ming, Y., Golaz, J.-C., Naik, V., and Ramaswamy, V. (2013). The roles of aerosol direct and indirect effects in past and future climate change. 118(10), 4521-4532. DOI: https://doi.org/10.1002/jgrd.50192

[57] Adams, P. J., Seinfeld, J. H., and Koch, D. M. (1999). Global concentrations of tropospheric sulfate, nitrate, and ammonium aerosol simulated in a general circulation model. 104(D11), 13791-13823. DOI:

https://doi.org/10.1029/1999JD900083

[58] Senf, F., Quaas, J., and Tegen, I. (2021). Absorbing aerosol decreases cloud cover in cloud-resolving simulations over Germany. 147(741), 4083-4100. DOI: https://doi.org/10.1002/qj.4169

[59] Wu, D., Ding, X., Li, Q., Sun, J., Huang, C., Yao, L., Wang, X., Ye, X., Chen, Y., He, H., and Chen, J. (2019). Pollutants emitted from typical Chinese vessels: Potential contributions to ozone and secondary organic aerosols. *Journal of Cleaner Production*, 238, 117862. DOI: https://doi.org/10.1016/j.jclepro.2019.117862

[60] Fu, T. M., & Tian, H. (2019). Climate change penalty to ozone air quality: review of current understandings and knowledge gaps. *Current Pollution Reports*, *5*(3), 159-171.

[61] Nwokolo, S. C., and Ogbulezie, J. C. (2018). A qualitative review of empirical models for estimating diffuse solar radiation from experimental data in Africa. *Renewable and Sustainable Energy Reviews*, 92, 353-393. DOI: https://doi.org/10.1016/j.rser.2018.04.118

CALL FOR PAPERS

Trends in Renewable Energy

ISSN Print: 2376-2136   ISSN online: 2376-2144
http://futureenergysp.com/index.php/tre/

Trends in Renewable Energy (TRE) is an open accessed, peer-reviewed semi-annual journal publishing reviews and research papers in the field of renewable energy technology and science. The aim of this journal is to provide a communication platform that is run exclusively by scientists. This journal publishes original papers including but not limited to the following fields:

- Renewable energy technologies
- Catalysis for energy generation, Green chemistry, Green energy
- Bioenergy: Biofuel, Biomass, Biorefinery, Bioprocessing, Feedstock utilization, Biological waste treatment,
- Energy issues: Energy conservation, Energy delivery, Energy resources, Energy storage, Energy transformation, Smart Grid
- Environmental issues: Environmental impacts, Pollution
- Bioproducts
- Policy, etc.

We publish the following article types: peer-reviewed reviews, mini-reviews, technical notes, short-form research papers, and original research papers.

The article processing charge (APC), also known as a publication fee, is fully waived for the Trends in Renewable Energy.

Call for Editorial Board Members

We are seeking scholars active in a field of renewable energy interested in serving as volunteer Editorial Board Members.

Qualifications

Ph.D. degree in related areas, or Master's degree with a minimum of 5 years of experience. All members must have a strong record of publications or other proofs to show activities in the energy related field.

If you are interested in serving on the editorial board, please email CV to editor@futureenergysp.com.